ON CARBONATE ALTERATION ZONES IN A GREENSTONE KEEL OF THE EAST PILBARA TERRANE (DOOLENA GAP GREENSTONE BELT)

Duncan Caleb Padraig Burke-Shyne

Bachelor of Applied Science (Geology)

Submitted in fulfilment of the requirements for the degree of

Master of Science (Research)

Science and Engineering Faculty

School of Earth, Environmental and Biological Sciences

Queensland University of Technology

2017

Keywords

Alteration, Archaean, carbonate, dome and keel, Doolena Gap, greenstone

Abstract

Archaean dome-and-keel structures are remnants of a unique tectonic mode of crustal reorganisation in the hot early Earth. They are often ascribed to a Rayleigh Taylor (RT) instability. Numerical models suggest that RT instabilities can only progress in dome-and-keel terranes if the effective viscosity of the mafic rock decreases, allowing for protracted periods of deformation accommodating large strain. I hypothesise that pervasive carbonate alteration of a greenstone has contributed to its protracted deformation, thus facilitating the formation of an Archaean dome-and-keel terrane through metasomatic weakening of the keel.

I examine two transects through alteration zones with detailed litho-structural analysis to investigate when the carbonate alteration observed in the keel rock occurred relative to the main deformation of the dome-and-keel formation event in the Archaean Doolena Gap Greenstone Belt (DGGB) in the Pilbara, Western Australia. Geochemical analysis of the transects was conducted to test if the presence of the pervasive carbonate alteration zones within the greenstone belt is controlled by the protolith. An alternative, competing hypothesis is that shear zones control the pervasive carbonate alteration zones.

I demonstrate that most of the carbonate alteration in the examined greenstone belt indeed occurred prior to or early on during the main deformation event accommodating the keel formation. The host rock bracketing the examined alteration zones is dominantly composed of chlorite + quartz + carbonates (calcite ± dolomite ± ankerite) with Fe-Ti oxides. Carbonates make up 30 % on average in the host rock. Within the alteration zones, the composition progressively increases in carbonate abundance hand in hand with a depletion of chlorite and quartz. In the alteration

zones, carbonate content increases up to 60 %. Deformation mechanisms on the micro-scale include a strong shape preferred orientation of chlorite and carbonate minerals and significant grain size reduction in quartz and carbonates by dynamic recystallisation through bulging and subgrain rotation. The trace element analysis shows that the altered carbonate material is derived from the same protolith as the host rock around it. Given the significant volumetric proportion of pre- to syn-deformational carbonates, it can be expected that they exert a significant impact on the bulk rheology of the greenstone keel during its descent into the lower crust.

Table of Contents

List of Figures

List of Abbreviations

Abbreviation	Meaning
CFB	Central Fold Belt
BLG	Bulging dynamic recrystallisation
CAZ	Carbonate alteration zones
DGGB	Doolena Gap Greenstone Belt
D_x	Deformation event 1-5 from oldest to youngest
GBM	Grain boundary migration dynamic recrystallisation
EPT	East Pilbara Terrane
F_x, f_x	Fold, fault associated with tectonic event
LA-ICP-MS	Laser Ablation Inductively Coupled Plasma Mass Spectroscopy
REE	Rare Earth Elements
SGR	Sub-Grain Rotation
SPO	Shape Preferred Orientation
XRD	X-Ray Diffraction
WDS-XRF	Wavelength Dispersive X-ray spectroscopy

Statement of Original Authorship

The work contained in this thesis has not been previously submitted to meet requirements for an award at this or any other higher education institution. To the best of my knowledge and belief, the thesis contains no material previously published or written by another person except where due reference is made.

QUT Verified Signature

Signature:

Date: __23/05/2017_____

Acknowledgements

I wish to acknowledge first and foremost my supervisors, Christoph Schrank and David Murphy for the countless hours they have put in and patience they've shown to help me get this far. Dan Wiemer for his assistance from field work through to data processing and interpretation. Of course my family, friends and partner for support outside of study and help keeping my focus on study when it has drifted.

I wish to acknowledge QUT staff from CARF and EEBS for their time and expertise in helping turn some old rocks into meaningful data. The Geological Survey of Western Australia for the use of their field equipment and vehicles without which field work wouldn't have been possible. Finally the rest of the field team for a great month in trying physical conditions; Tom Spring, Ali Sternes and Shoshannah O'Connor.

Computational (and/or data visualisation) resources and services used in this work were provided by the HPC and Research Support Group, Queensland University of Technology, Brisbane, Australia.

Chapter 1: Introduction

1.1 Background

Archaean greenstone belts are highly deformed synclines of dominantly meta-volcanic rock with minor clastic metasediments, which envelope tonalite-trondhjemite-granitoid (TTG) domes. The so-called dome-and-keel terranes form the cores of cratons and contain the oldest continental material on Earth (Boulter et al., 1987; Collins, 1989; Hickman, 2012; Hippertt and Davis, 2000; Marshak, 1999; Marshak et al., 1997; O'Neill and Debaille, 2014). Greenstone belts are frequently associated with pervasive carbonate alteration zones (Arndt et al., 1989; Collins, 1989; Polat and Hofmann, 2003; Van Kranendonk et al., 2003; Zegers et al., 2002). Carbonate alteration zones (CAZ in the following) are observed as veins or as pervasive alteration of the host rock, and their emplacement is typically interpreted to originate from sea floor alteration of the volcanics (Arndt et al., 1989), or to be associated with fluid flow in shear zones (Collins, 1989; Polat and Hofmann, 2003). In addition to its association with zones of high strain (Collins, 1989; Polat and Hofmann, 2003), carbonate alteration also occurs in proximity to the ultramafic domains in greenstone belts (Polat and Hofmann, 2003) suggesting an association with lithology. Additionally, it has been shown that intense carbonate alteration can result in mobilisation of typically immobile species such as the REE (Rare Earth Elemenets) and HFSE (High Field Strength Elements, e.g., Zr, Y, Hf) changing the observed geochemical trends used to characterise petrogenesis (Lahaye et al., 1995; Murphy and Hynes, 1986). Finally, the source of the carbonate alteration may also play a role in the degree of mobilisation of species. Polat and Hofmann (2003) have shown that the the source of carbonate alteration may play a role in the degree of REE mobility.

Metasomatism, and thus carbonate alteration, of mafic-ultramafic rocks can involve the addition or removal of various chemical species, depending on the fluid source composition

(Harlov and Austrheim, 2013). The alteration is controlled by temperature, pressure and geochemical gradients due to lithological differences (Andreani et al., 2009; Klein and Garrido, 2011). Multiple generations of alteration are common with late, episodic, lower grade events overprinting earlier events, preserving only the youngest alteration (Alt et al., 1989). The main processes during the alteration of mafic-ultramafic rocks are serpentinisation (Blatt et al., 2006) (hydration reactions) and talc-carbonation (Bjerga et al., 2015) (CO_2 reactions). Metasomatic carbonate alteration of greenstones involves the addition of Ca, Mg and CO_2 and subsequent removal of Si, Na and K (Harlov and Austrheim, 2013). The carbonate involved in the metasomatic alteration requires a source, which typically includes mantle degassing, sea floor water circulation, or primary precipitation of carbonate minerals, which later react due to the large geochemical potential gradients between carbonates and greenstones (Harlov and Austrheim, 2013; Van Kranendonk, 2006; Yardley, 2013).

In summary, CAZ in greenstone belts constitute zones of major mass transfer and possibly give insight into protolith distribution, shear-zone formation, and the source of the carbonate. From this, the general questions arise: how are CAZ related to the formation of the greenstones and what is their role in facilitating the protracted deformation of the greenstone keels.

1.2 Research Questions and Significance

1.2.1 Research questions

The purpose of this thesis is to investigate the origin and relative timing of carbonate alteration zones (CAZ) in the polydeformed Doolena Gap Greenstone Belt (DGGB), which is in the East Pilbara Terrane, a type locality of dome-and-keel-terranes. This leads to the research questions:

1. When did the carbonate alteration occur? Was it pervasive, late-stage, retrograde alteration? Or were there multiple distinct alteration events throughout the deformation history of the DGGB?

Particular attention is paid to localised CAZ associated with the deformation event accommodating dome-and-keel formation in the research area (D_2 sensu Wiemer et al. (2016). The question arises:

2. Did the D_2 CAZ form in shear zones or did they form due to a local difference in the protolith of the mafic schists?

To answer these questions, I present a detailed examination of two transects through CAZ from the Central Fold Belt (CFB) (Figure 7) of the DGGB. The CFB is of interest to the examined dome-and-keel terrane in particular because it preserves clear CAZ separating fairly undeformed mafic lozenges of the keel host rock. This observation inspired research question 2, namely if the CAZ were shear-zone related. Moreover, using the classical notion that space may serve as substitute for time in outcrop (Fusseis et al., 2006), one can examine the evolution of alteration along a transect from a greenstone host into a CAZ. In addition, within the CFB, CAZ are observed throughout the keel rock associated with multiple deformation events, as evidenced by overprinting relationships. In fact, the CFB features the clearest rock record of the protracted deformation history exhibited by this greenstone belt. Therefore, it is the best place to study the research questions in the DGGB.

1.2.2 Research significance

The extensive presence of CAZ in the CFB suggests that carbonate alteration played a significant role in the mass fluxes within the keel rock as it sagducted during TTG dome emplacement. Given the ubiquity of D_2 CAZ, two competing hypotheses regarding the deformation and formation of CAZ in the dome-and-keel terrane arise:

1. Deformation localisation and associated CAZ are host-rock controlled. In this case, CAZ form where host rocks are present which are most conducive to carbonate

alteration. The formation of fairly weak carbonate minerals may then lead to a locally weaker package of rock, which may localise ongoing deformation.

2. The formation of CAZ is controlled by ductile shear instabilities. Ductile shear zones are known to focus not only deformation but also temperature due to shear heating and/or advection, (Regenauer-Lieb et al., 1999; Regenauer-Lieb and Yuen, 2003) and fluid flow (Connolly and Podladchikov, 2004; Fusseis et al., 2009). Hence, it is conceivable that carbonate alteration occurs as a consequence of shear localisation, either through feedback processes such as thermally induced chemical pressurisation (Poulet et al., 2014; Sulem and Famin, 2009)) or advection of reactive fluids (Ferry and Gerdes, 1998; Putnis and Austrheim, 2010).

Answering the research questions will contribute to this debate. Moreover, they will help to better constraining mass fluxes within greenstone keels and thus a fundamental mode of crustal reorganisation in the Archean. In addition to the academic interest in the tectonic processes associated with the formation of Archaean crust, there are economic applications to understanding dome-and-keel terranes. Many of the world's gold deposits are hosted within Archaean granitoid-greenstone terranes (Goldfarb et al., 2001; Zegers et al., 2002).

Chapter 2: Literature Review

2.1 Archaean Granitoid-Greenstone Terrane

In map view, Archaean granitoid-greenstone terranes typically present ovoid-shaped domes surrounded by narrow synclinal keels of mafic to ultramafic greenstone successions (Figure 1) (Lin, 2005; Marshak et al., 1992; Marshak et al., 1997; Zibra et al., 2014). The contacts between the TTG and greenstone keel are highly sheared. Most of the deformation is concentrated in the keel rock, which usually exhibits steep to vertical secondary foliations wrapping around the dome contact, however the marginal gneisses can also be heavily deformed. Not all Archaean greenstone terranes present a with a keel structure, however this is the case within the study area of this thesis and as such the focus of the literature review will be on greenstones that present with a keel.

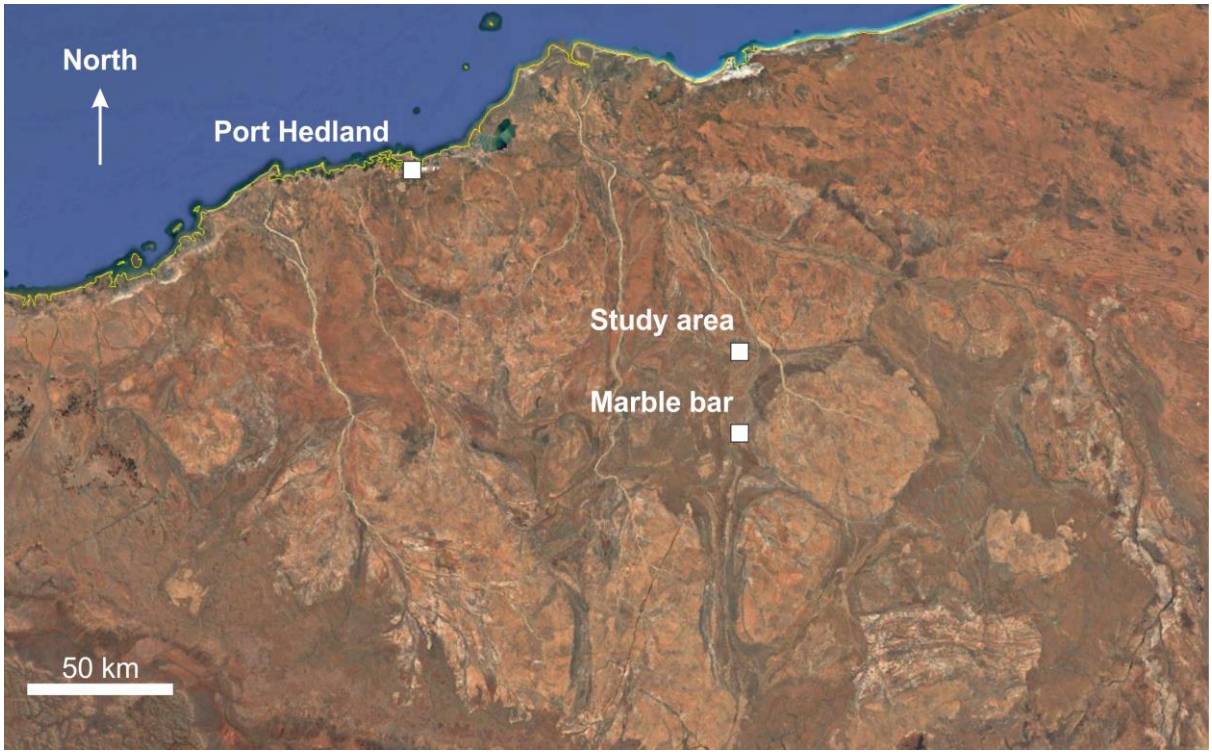

Figure 1: Google Earth satellite image of the Pilbara in northern Western Australia, a type locality for Archaean TTG-greenstone terranes. Ovoid TTG domes appear in light colours – the town Marble Bar, for example, sits on the western edge of a dome – bounded by dark greenstone keel rock.

This unique radial symmetry reflects the formation process of dome-and-keel terranes (Lin, 2005; Marshak et al., 1992; Marshak et al., 1997; Zibra et al., 2014). They are thought to form as Rayleigh-Taylor (RT) instabilities, which usually exhibit some form of radial symmetry because they are a fluid-dynamic instability (Gogus and Pysklywec, 2008). RT instabilities form when a dense viscous fluid overlies a less dense one: the former eventually drips downwards while the latter ascends (Drazin and Reid, 1981; Kull, 1991). In contrast, modern plate tectonics most commonly creates 1000's of kilometres long linear or gently curved features (with exceptions) because of the elasto-plastic rheology of the upper lithosphere (Burov, 2011) and the dominantly horizontal movement. The partial convective overturn in Archaean vertical tectonics is driven primarily by the density contrast between the ascending TTG and sagduction of the greenstone (de Bremond d'Ars et al., 1999). Numerical models suggest that this occurs fast geologically, of the order of 10 Ma (Conrad and Molnar, 1997; Robin and Bailey, 2009). Examples of Archaean dome-and-keel terranes thought to be formed by vertical tectonics are the Dhawar Craton in India (Chardon et al., 1998), parts of the Superior Craton in Canada (Lin, 2005) and the East Pilbara Terrane (EPT) (Van Kranendonk, 2004) in Australia.

In contrast to the vertical tectonics model, a dominantly horizontal kinematic model has been proposed (Kloppenburg et al., 2001; Marshak et al., 1992; Marshak et al., 1997). This model is similar to a steepened metamorphic core complex formed during active crustal extension and like the vertical tectonics model predicts a shear zone at the boundary between the dome and the greenstone belt (Figure 2). However, a notable difference is that the horizontal model predicts unidirectional stretching lineations in the shear zone. In contrast, the vertical RT model implies radially plunging stretching lineations with regards to the dome centre (Kloppenburg et al., 2001; Zegers, et al., 2002).

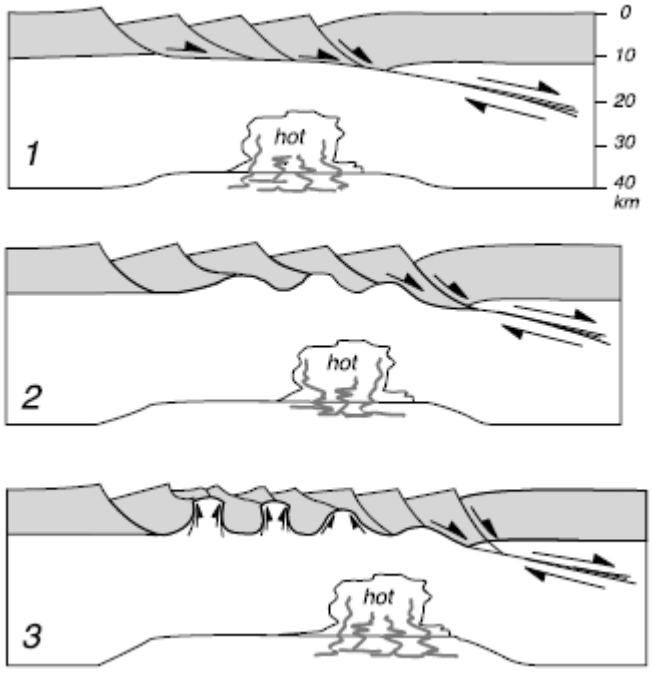

Figure 2: Cross section schematic of the metamorphic core complex model for horizontal tectonic formation of Archaean greenstones. Basement rock is white, supracrustals are shaded. (1) Initial extension (2) Early dome formation as horizontal extension continues (3) Late stage of dome formation. Note that the domes are not solid state diapirs as in vertical tectonics but MCC's with steepened sides (Marshak et al., 1997).

The vertical and horizontal models are not necessarily mutually exclusive. Some authors have described features within Archaean granitoid-greenstone terranes that indicate both horizontal and vertical movement occurring synchronously (Lin, 2005). For example, the Carrot River greenstone belt in the Superior province has complex overprinting features that suggest both vertical, solid state diapiric movement and horizontal active extension (Lin, 2005). Moreover, 3D analogue models of RT instabilities demonstrate that even circular drips can cause cylindrical horizontal deformation in the crust (Pysklywec & Cruden, 2004).

Nevertheless, the seminal work of Van Kranendonk and others (Collins et al., 1998; Hickman 2004; Hippertt and Davies 2000; Lin, 2005; Marshak 1997) strongly supports that the Archean Pilbara craton formed due to RT instability. This region is the focus of the work at hand. The Archaean granitoid-greenstone terrane comprising the lithosphere exhibits fluid-like behaviour during RT instabilities due to the unique temperature budget of the early

Earth: the Archaean Earth was hotter than modern day Earth due to a higher concentration of radiogenic elements and hotter mantle conduction from residual accretionary heat (O'Neill and Debaille, 2014). This increased temperature led to a weak viscous lower and midcrust (Brace and Kohlstedt, 1980; Burgmann and Dresen, 2008; Dimanov et al., 2011) and also promoted intracrustal melting, which in turn decreased viscosity further and induced TTGs to form from mafic-ultramafic proto-crust (Rushmer and Jackson, 2006). Recent numerical models developed explain the high degrees of Archaean volcanism due to increased temperature and resultant sagduction of the density inverted lithosphere stack (O'Neill and Debaille, 2014; Thébaud and Rey, 2013).

Based on the RT instability, the most common genetic model for dome-and-keel terranes is summarised in the following (after (Lee, 2006; Lin, 2005; Rey et al., 2003; Smithies et al., 2005; Van Kranendonk, 2004; Van Kranendonk, 2010; Van Kranendonk et al., 2004)):

[1] The greenstone keels are composed of mafic-ultramafic volcano-sedimentary successions deposited in roughly horizontal layers.

[2] After reaching a critical thickness, the hot volcanic upper crust becomes gravitationally unstable and sinks into the lower crust or mantle in the form of a radially symmetric drip.

[3] At the same time, large intrusive TTG bodies ascend due to their low density relative to the mafic-ultramafic volcano-sedimentary stack. They form domes (i.e., “bubbles”) around which the greenstones sink forming sheared synclines near the dome interface.

The contact is a zone of concentrated shearing that can be observed as near vertically oriented penetrative foliation (Hippertt and Davis, 2000; Marshak et al., 1992; Marshak et al.,

1997). A simplified cross-section schematic of this process with relative movement is shown in Figure 3.

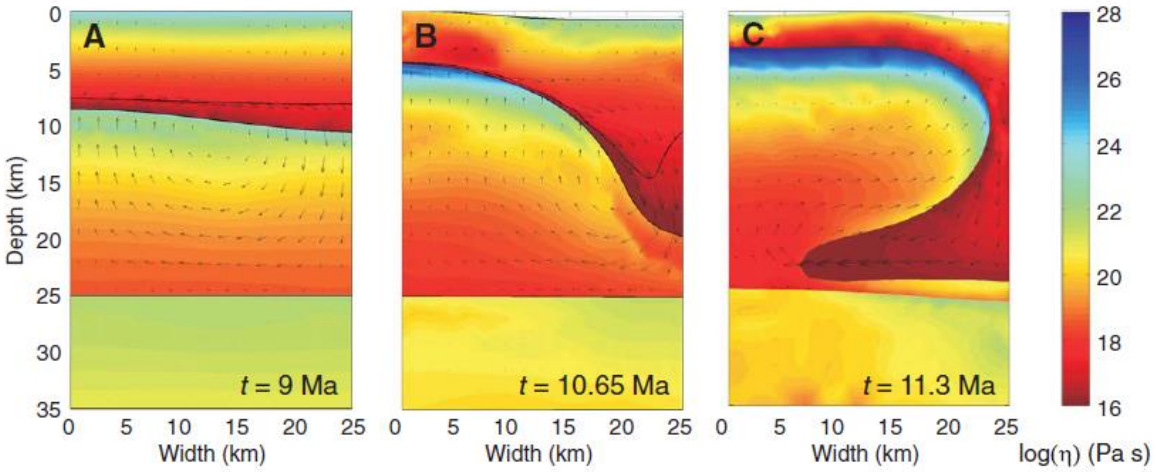

Figure 3: 2D Numerical model of typical Archaean crust arrangement through a RT instability with dense, weak greenstone overlying buoyant felsic sub-cratonic lithospheric mantle from (Robin and Bailey, 2009). The typical dome-and-keel geometry that forms as a result of the overturn is observed, and the time scale shows the rapid progression resolving the density contrast.

2.2 East Pilbara Terrane

The Pilbara is an ovoid Archaean (3650 – 2830 Ma) craton containing metasedimentary, metavolcanic and mafic-ultramafic intrusive rock (Bagas, 2001-2002; Van Kranendonk, 2010). The East Pilbara Terrane (EPT, Figure 4), 3525 – 3235 Ma, is composed of dominantly granitoid domes and greenstone keels. The EPT greenstone belts are composed of three groups separated temporally by two unconformities. The basal 3.53 – 3.43 Ga Warrawoona Group is unconformably overlain by the 3.35 – 3.31 Ga Kelly Group, which is in turn unconformably covered by the 3.27 – 3.24 Ga Sulphur Springs Group (Figure 5). The groups follow a general trend with basal mafic volcanics overlain by an upper felsic volcanic unit. The volcanic cycles are part of a succession of eight magmatic cycles in the EPT that are interpreted as mantle plumes (Hickman, 2012; Smithies et al., 2007; Van Kranendonk, 2010).

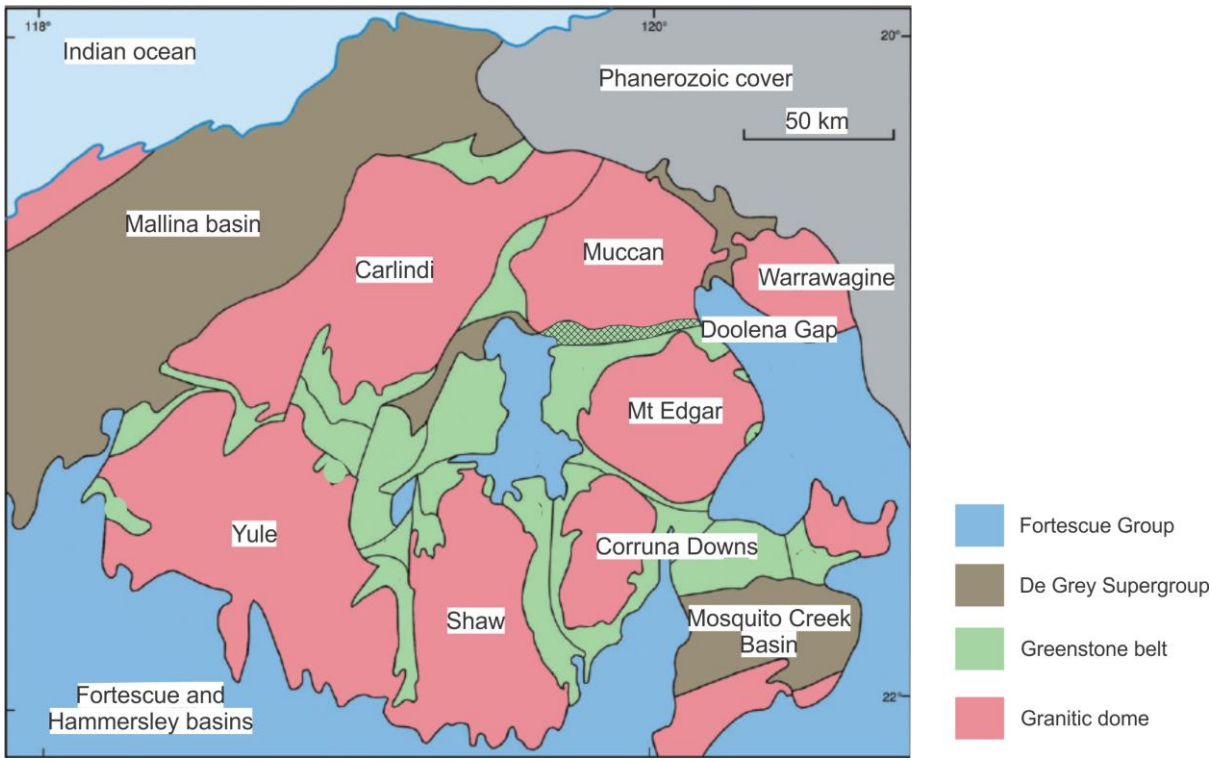

Figure 4 Doolena Gap Greenstone Belt location showed with hatching within the EPT. Simplified regional geology of the EPT shown, for detail on DGGB see Figure 5 (modified from (Hickman, 2012)

The Pilbara Supergroup is overlain by a number of supergroups, supersuites and suites that extend across the whole Pilbara (Figure 5). Immediately above the Pilbara Supergroup is the Soanesville Group (3.18 – 3.10 Ga) composed of mafic volcanics that are sandwiched between shallow-water sedimentary rocks. An angular unconformity separates the Soanesville Group from the overlying De Grey Supergroup (3.10-2.90 Ga), a succession of mafic-felsic volcanics sandwiched by sedimentary rocks. Two supersuite granitoids, Cutinduna and Split Rock (2.89 – 2.83 Ga), are emplaced into the De Grey Supergroup (Hickman, 2012; Smithies et al., 2007). A series of large mafic dikes, The Black Hill dolorites are dated at 2.77 Ga and trend roughly north-south and cuts the supergroups (Wingate, 1999).

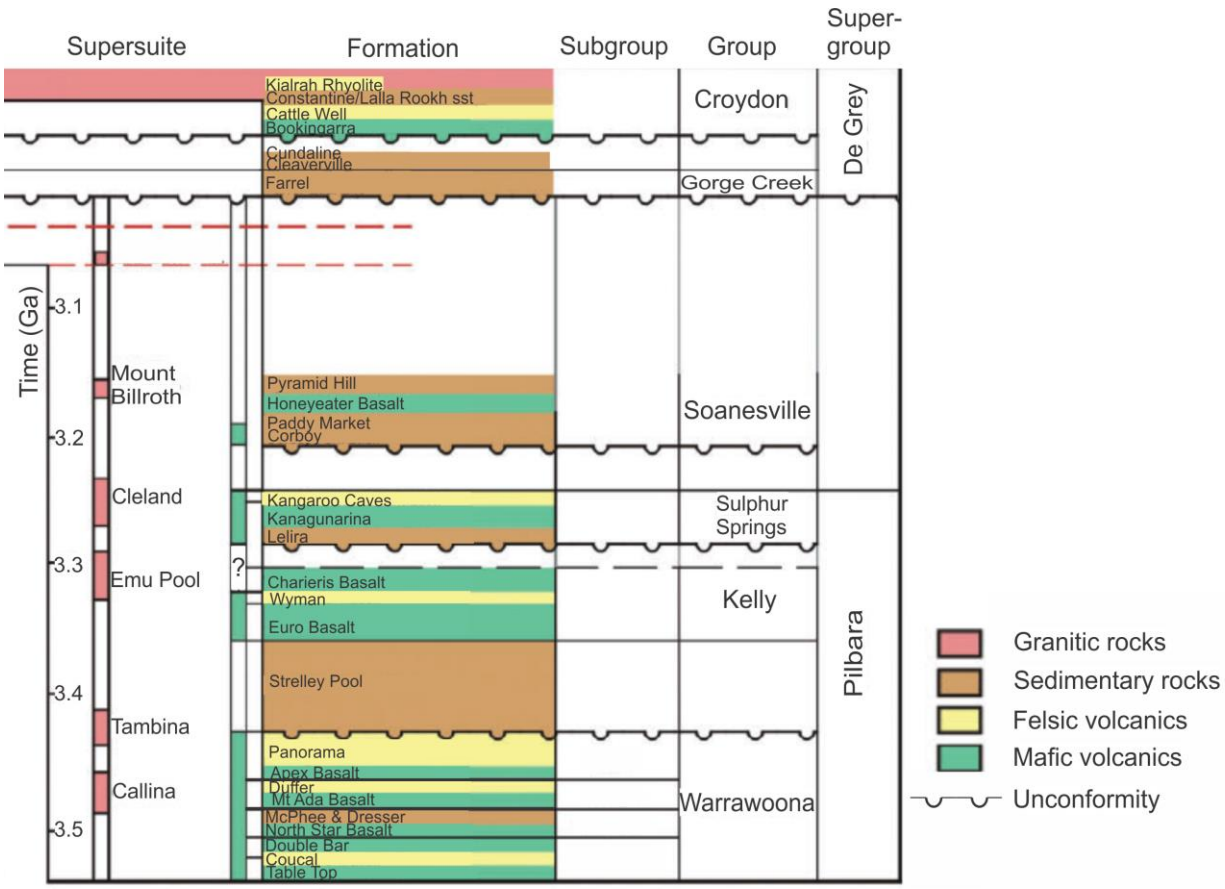

Figure 5 Space-time plot of the East Pilbara Terrane. The focus of this thesis is contained within the basal Warrawoona Group (modified after *(Hickman, 2012)*

The Warrawoona Group covers approximately 35,000 km^2 with a calculated maximum thickness of 12 km (Hickman, 2012). The Warrawoona Group is purported to have been deposited on pre-3.5 Ga supracrustal rock which is rarely observed through xenocrysts and detrital zircons (Green et al., 2000; Hickman, 2012; Kemp et al., 2006; Smithies et al., 2009). The Strelley Pool Formation is dated at 3.43 Ga (Van Kranendonk, 2004, 2006) and provides an age constraint as it unconformably overlies Warrawoona. It is a shallow-water, marine sedimentary deposit as evidenced by stromatolites, quartzose sandstone, evaporites and depositional chert with minor metamorphism (Green et al., 2000; Lowe, 1983). The Warrawoona felsic volcanic units closely coincide with the emplacement of the EPT

granitoid supersuites: 3.47 Ga Callina, 3.43 Ga Tambina, 3.31 Ga Emu Pool, and 3.25 Ga Cleland. These supersuites form the multiphase granitoid complexes surrounding the DGGB from Carlindi to the west, Mount Edgar to the south, and Muccan to the north (Figure 4).

2.3 Doolena Gap

The Doolena Gap Greenstone Belt (DGGB) is situated in Western Australia approximately 200 km southeast from Port Hedland (Figure 4). The DGGB is bound by the associated Muccan dome to the north and has a post-keel-formation fault contact with the Marble Bar greenstone belt to the south (Figure 6). Towards the east, the Fortescue Group covers the DGGB unconformably. In the centre it narrows to a 1-2km wide zone of highly metamorphosed and tectonised schists. To the west it widens out and is overlain unconformably by the De Grey Supergroup. The DGGB is composed of metavolcanic-metasedimentary rocks of the Warrawoona Group (c.3530 – 3426 Ma), metasedimentary Strelley Pool Formation (ca. 3430 Ma) and metavolcanic Kelly group (ca. 3350 – 3310 Ma) (Hickman, 2012; Nijman et al., 1999; Van Kranendonk, 2010). It has experienced extensive volcanism of both mafic and felsic composition, the Mt Ada basalt and Duffer Formation respectively (Smithies et al., 2007; Van Kranendonk, 2010; Wiemer et al., 2016). It constitutes the northern overturned synclinal limb of the greenstone belt wrapping around the southern margin of the Muccan granitoid dome. The DGGB exhibits a decrease in deformation intensity with increasing distance to the dome (Wiemer et al. 2016). Wiemer et al. (2016) identified four structural domains within the DGGB (Figure 7). From north to south they are: the Muccan Granitic Complex (MGC), the South Muccan Shear Zone (SMSZ), the Central Fold Belt (CFB), and the Low-Strain Belt (LSB).

Throughout the greenstone belt there are narrow (metres to tens of metres) zones showing intense pervasive carbonate alteration. These CAZ are most common within the CFB. They disappear to the north with a corresponding increase in metamorphic grade (to

amphibolite facies) in the SMSZ, and they become less frequent with a decrease in metamorphic grade (to lower greenschist facies) within the Low-Strain Belt (Wiemer et al., 2016). However, large faults in the LSB always exhibit complex carbonate-alteration patterns. This study focuses on the CFB because it constitutes the zone of the DGGB that accommodated most of the dome- and keel-forming event and contains the most pervasive CAZ in the area.

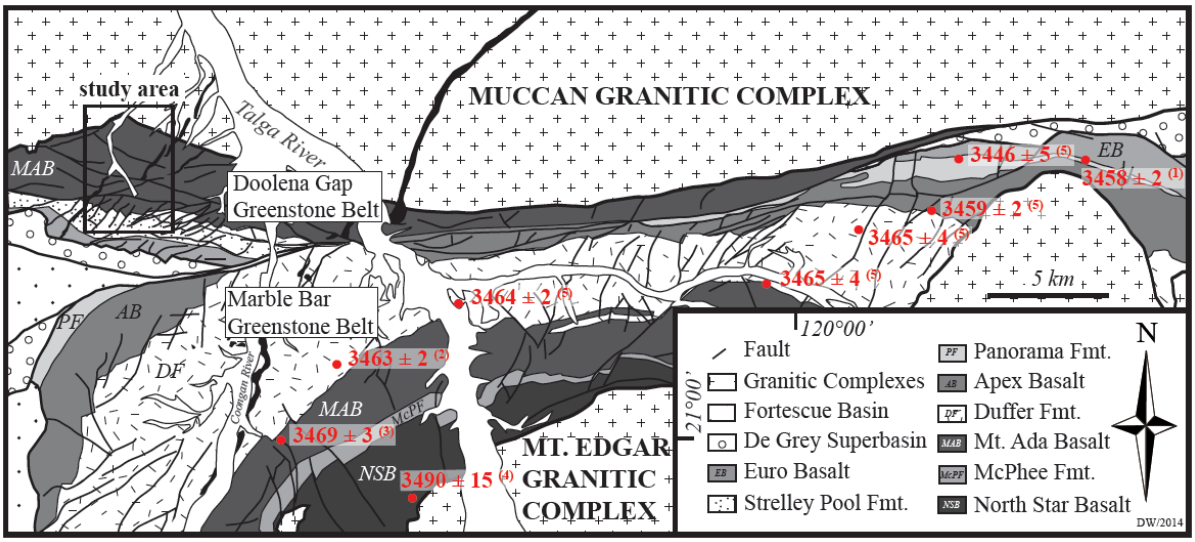

Figure 6 Geological map of the Doolena Gap-Marble Bar greenstone belt with Muccan and Mt Edgar granitic domes (Wiemer et al., 2016)

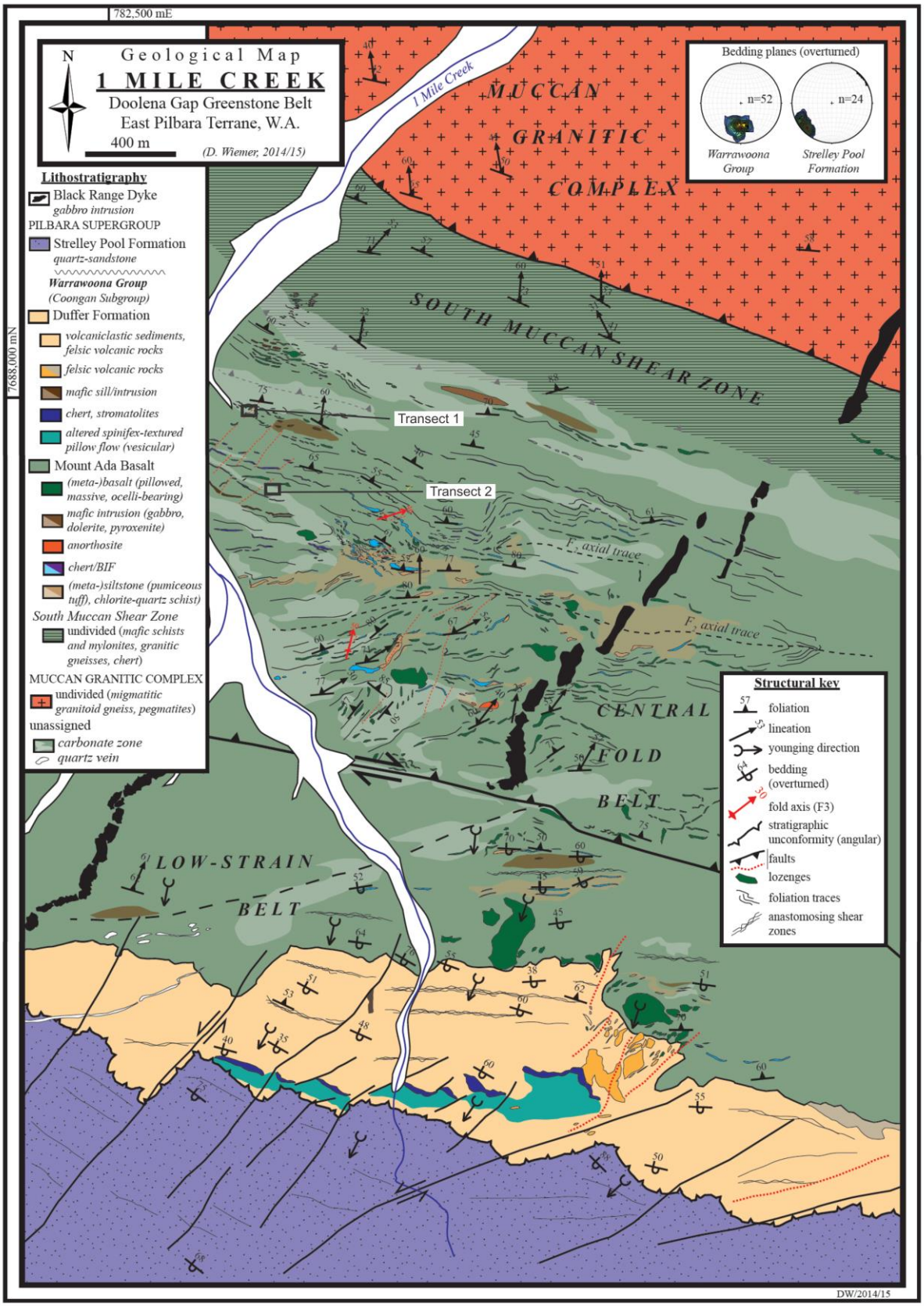

Figure 7: The DGGB geological map showing transect locations of this study (from (Wiemer et al., 2016))

2.3.1 The Central Fold Belt

Wiemer et al. (2016) described the geological and deformation history of DGGB in detail and has established nomenclature that will be used throughout the remainder of this thesis. A brief summary of the deformation history is as follows, with the focus on the Central Fold Belt as the transects of this study are within that structural domain. A cartoon block diagram assists in visualising the description of the events (Figure 8):

2.3.1.1 D_1 event

D_1 structures are poorly preserved and thus difficult to correlate across the structural domains conclusively. A rare S_1 foliation is expressed as early gneissic foliation within the MGC. It presents itself as a composite S_2 foliation within the schists of the CFB. It is suggested that D_1 reflects a sub-horizontal foliation indicating horizontal stretching and vertical contraction of the middle crust during the initial vertical ascension of the Muccan Graditoid Dome. Carbonate veining is also associated with this event.

2.3.1.2 D_2 event

D_2 is the most intense deformation event associated with the dome emplacement and keel sagduction. It is characterised by overturned, tight-isoclinal F_2 folds in the CFB and the regional, approximate east-west trending S_2 foliation. F_2 axial planes dip steeply to NNW with steeply E or W plunging hinges. F_2 folds are frequently rootless and highly transposed parallel to the S_2 foliation, which often forms anastomosing fabrics around mafic lozenges and/or remnant hinges. D_2 reflects a protracted progressive non-coaxial deformation.

2.3.1.3 D_3 event

D_3 is characterised by open, upright, asymmetric, dextral F_3 folds on the 10's of metre to centimetre scale with steeply NE plunging hinges showing dome-up kinematics. They form local S_3-crenulation cleavage. The deformation has associated carbonate veining.

2.3.1.4 D_4 event

D_4 involves NNE-NE trending structures that include ductile f_4 faults and F_4 drag folds. The Strelley Pool Formation (SPF in diagram) displays brittle faulting whereas within the CFB ductile drag folds are observable.

2.3.1.5 D_5 event

D_5 involves late-stage E-W trending faults that displace the late gabbroic Black Range mega-dike. They exhibit dextral offsets in map view, reactivate CAZ in the CFB, and form the boundary between CFB and Low Strain Belt. D_5 postdates the other events by a large time gap because the dike suite is dated at 2.78 Ga (Wingate, 1999).

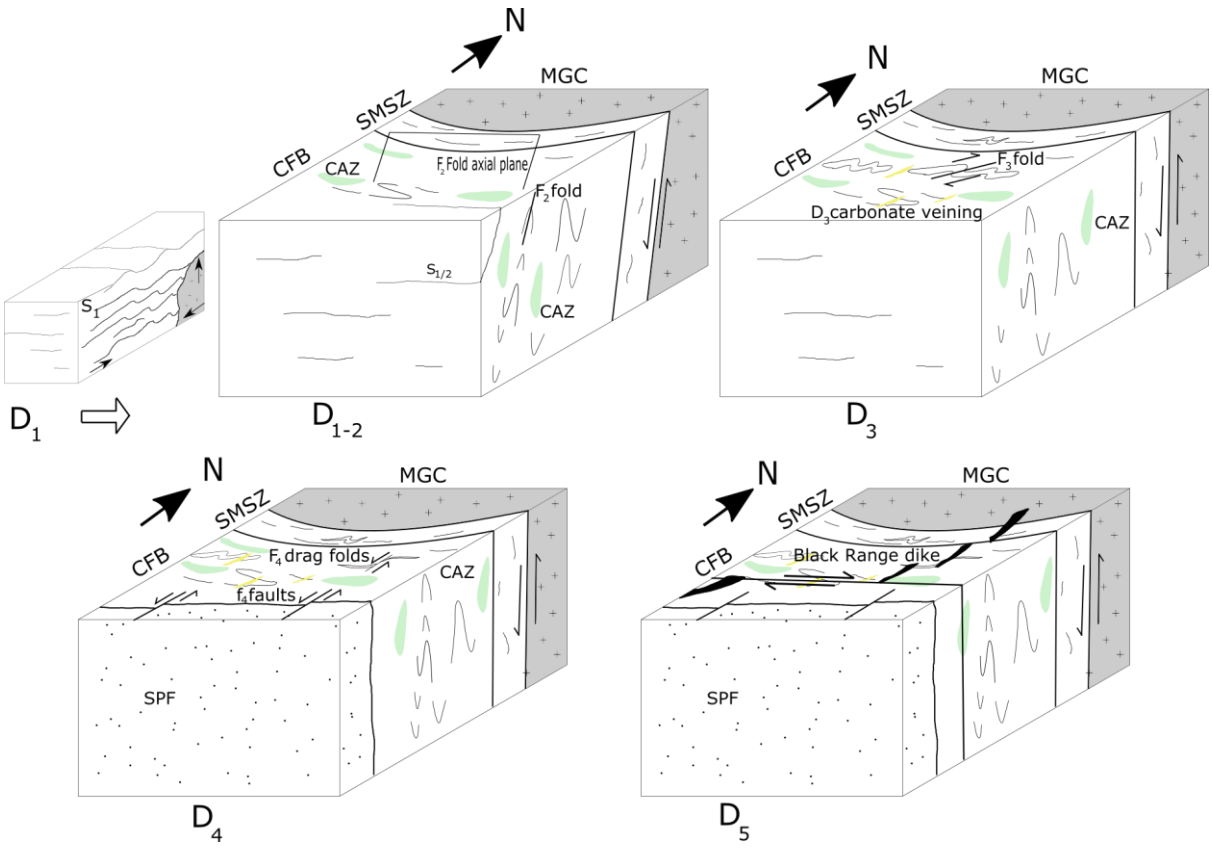

Figure 8: Cartoon block diagram to illustrate the deformation events described in text. D_1 structures are rarely seen and D_2 represents a protracted, progressive deformation under similar kinematics, as such D_{1-2} are shown with a D_1 inset into the major D_2 event. At each new deformation event previous kinematic indicators have been removed to ensure that the diagram remains legible. See text for full description of the deformation events, the focus of this thesis is the CFB.

2.4 Carbonate emplacement mechanisms

The mechanisms of carbonate emplacement most relevant in this study are primary precipitation of carbonate minerals within the interstitial spaces of basaltic pillow lavas (Figure 9), metasomatic alteration producing carbonate minerals, and hydraulic fracturing (Figure 10). A conceptual schematic of these three mechanisms illustrates the relative location of where to expect these processes and the likely reactions that would occur (Figure 11).

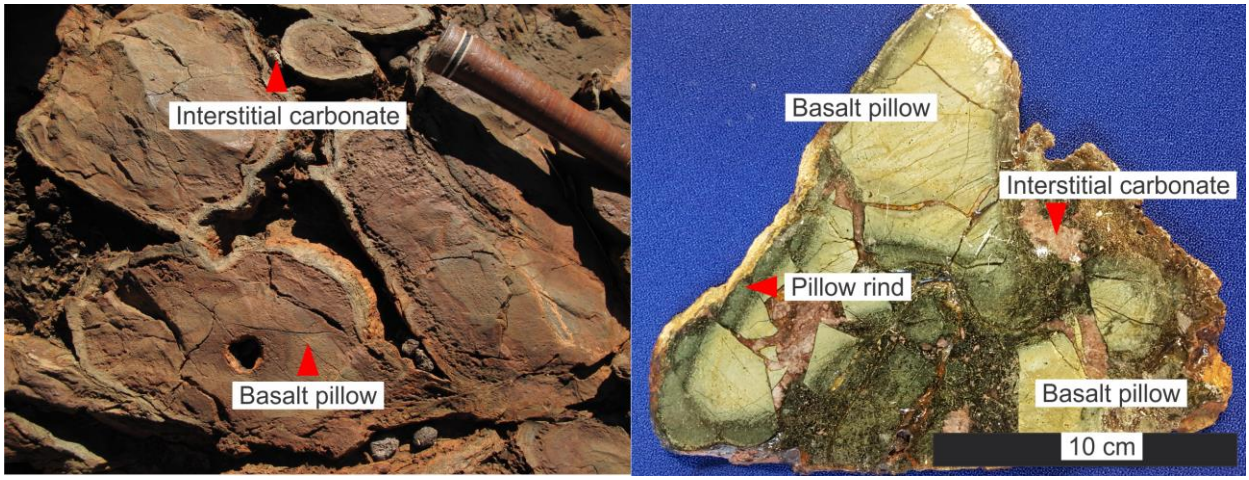

Figure 9 Field photo of pillow basalts with interstitial carbonate material (left) and polished section of pillow basalt showing the interstices filled with carbonate minerals (right). Rock hammer gives scale for field photo.

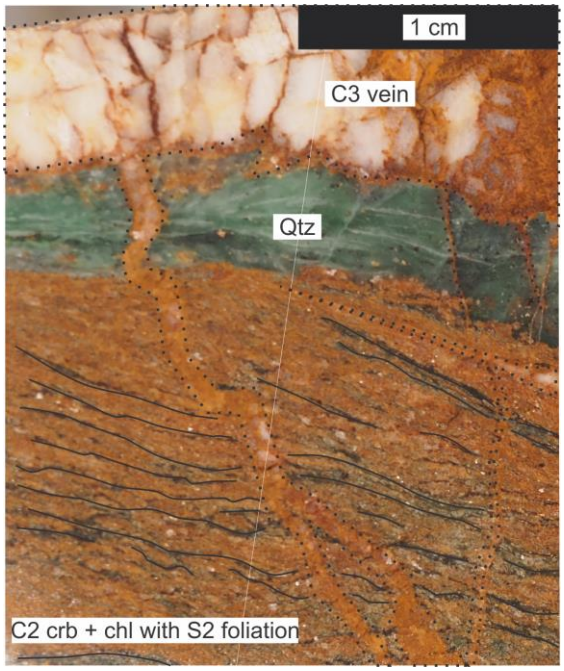

Figure 10 Overprinting relationship between C_2 carbonate + chlorite showing S_2 foliation and C_3 carbonate vein. C3 vein is outlined with dotted line to help visualise the cross cutting relationship. Sample 1-6c, surface shown is perpendicular to the S_2 foliation and parallel to L_2.

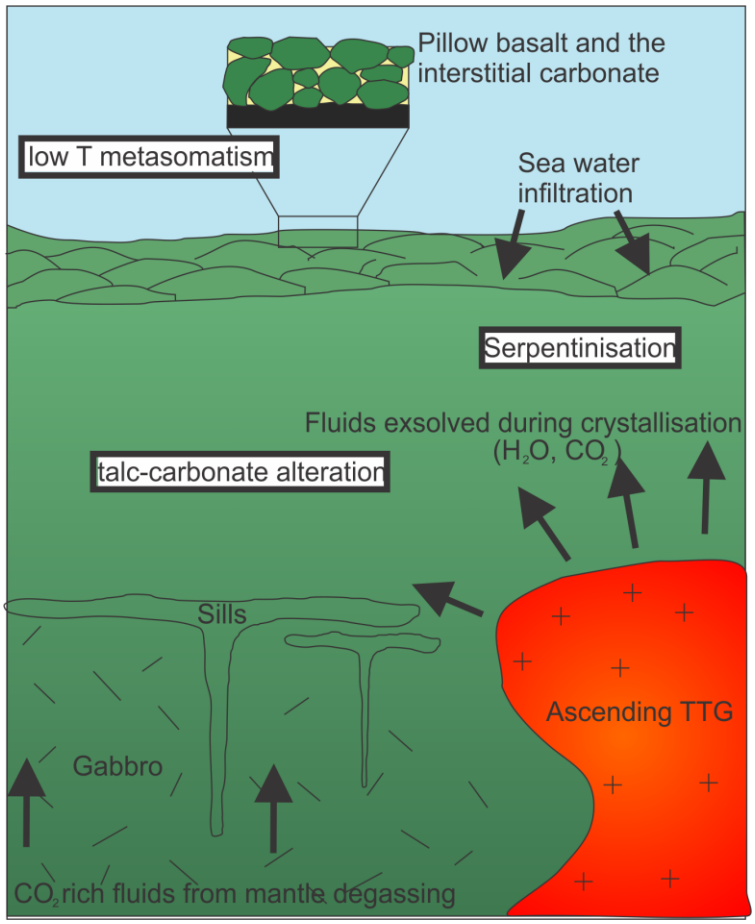

Figure 11: Conceptual schematic cross section of Archaean greenstone with carbonate sources for DGGB, not to scale. The interstitial spaces left by extrusive pillow basalts can be filled by seawater rich in CO_2 and metal ions. Mafic sills create space allowing pathways for fluids and volatiles such as mantle CO_2 degassing. Ascending TTG body releases heat and volatiles such as H_2O and CO_2, which can drive metasomatic alteration.

2.4.1 Primary precipitation

Pillow basalts form where lava extrudes into an aqueous environment (Figure 9) (Rakovan, 2005). The pillows begin to alter almost immediately after their formation because of the steep temperature and chemical potential gradients between anhydrous basaltic minerals and cold seawater (Ordóñez-Calderón et al. 2008; Polat et al. 2012). The latter is rich sodium, chloride, sulphate and carbonate ions. Primary carbonate precipitation occurs in the interstices between pillows along with metasomatic alteration of the basalt itself (Rakovan, 2005; Tucker and Wright, 1990). The large temperature gradient causes rapid cooling resulting in fractures and enhanced permeability, which facilities low-temperature alteration of the basalt. Plagioclase reacts to calcic zeolites, prehnite, carbonates, epidote and chlorite and olivine alters to serpentine (Blatt et al., 2006). Since seawater is undersatured in basaltic components such as CaO and SiO_2, these are typically removed from the rock and transported as aqueous solutions elsewhere (Blatt et al., 2006). The volume portion of interstices between pillows varies from a possible 10 % (Dimroth et al., 1978) up to as large as 40 % (Wells et al., 1979) when vesicles are considered as potential sites for carbonate precipitation. Because the DGGB is rich in pillow basalts, primary carbonates are expected to contribute significantly to the carbonate budget of this system. During extensive carbonate alteration of pillow basalts, chemical species that are typically immobile in other styles of alteration (eg REE) can become mobilised with mobility of these species being higher at the pillow rims and less altered within the pillow cores (Ordóñez-Calderón et al. 2008; Polat et al. 2012). As such care must be taken when interpreting trace element data and the selection of chemical species that are immobile should be justified through further analysis to confirm the lack of mobility.

2.4.2 Hydraulic fracturing

Hydraulic fracturing occurs when the pore-fluid pressure is increased to a point such that the effective pressure becomes small enough to move the deviatoric state of stress into a domain where it touches the brittle-plastic yield envelope. Possible fluid sources can be devolatisation from crystallising bodies or injection from external sources through the pore spaces and/or fractures. Crystallisation of a magma body can result in devolatisation, producing fluids with pressures large enough to overcome the tensile strength of the country rock (Winter, 2010). The fluids produced are buoyant and will migrate due to the density contrast between solid rock and fluid and can be transported at remarkable speeds geologically, reaching up to 1 km/hr (Rumble, 1994). This process is episodic in nature as the fluid pressure will quickly dissipate as the fluids migrate. External fluid sources could originate from sea water infiltration and circulation or mantle degassing.

Hydraulic fracturing is important in the case of DGGB, as evidenced by ubiquitous veining associated with all deformation events. Shallow metasomatic carbonate alteration typically involves reacting infiltrating sea water and fresh mafic lithosphere, whereas deep metasomatic alteration is due to the interaction of fluids advected from deeper degassing mantle sources, which are high in CO_2 (Harlov and Austrheim, 2013). In either case, alteration is typically constrained to zones that enable fluid flow such as shear zones or fracture networks such as those created with sill emplacement or hydraulic fracturing due to devolatisation reactions (Figure 11).

2.4.3 Metasomatism

Metasomatism is the pervasive alteration of rock due to interaction with aqueous fluids that results in a changed chemical composition while remaining in the solid state (Zharikov et al., 2007). Metasomatism is an open-system process requiring fluid fluxes creating a chemical potential gradient between the host and the fluids that is enhanced by large

temperature gradients (Andreani et al., 2009; Klein and Garrido, 2011). Metasomatic fluids are physically sourced in three different ways (after (Harlov and Austrheim, 2013)):

- Pre-existing pore fluid that has escaped or is being released from a host rock. This includes fluid such as circulating seawater as this fluid exists in the pore spaces
- Fluids that are released during metamorphic devolatisation reactions.
- Fluids released during magmatic-body crystallisation. These fluids are expelled in a single direction away from the crystallising body and do not circulate.

Due to the involvement of fluids, metasomatism is either localised in shear zones, faults and fracture systems, or distributed through advective fluid transport in the crust, for example due to large intrusive bodies (Figure 11) (Harlov and Austrheim, 2013). The microphysical mechanisms for distributed fluid flow in mid to deep crustal ductile rocks are still debated. The high confining pressures do not permit a static, interconnected, open pore network. Likely candidates for fluid pathways in this domain are grain boundaries (Bailey, 1990) and creep cavities (Fusseis et al., 2009). The DGGB shows pervasive metasomatism within the regional foliation formed during the overturn event, as shown below. Brines sourced from exsolution of a crystallising TTG body that interact with the mafic crust are an excellent driver of metasomatic alteration (Harlov and Austrheim, 2013). The granitic Muccan dome to the north of Doolena Gap could therefore be a source for a metasomatic fluid. However, CO_2-rich fluids are more typically associated with basic magmas (Kamenetsky and Kamenetsky, 2010). Thus, the Muccan granitoid is a potential source for fluids to drive serpentinisation but an unlikely source for carbonate alteration. On the right of Figure 11 the ascending TTG dome creates a temperature gradient and exsolves volatiles that can be rich in H_2O and/or CO_2. The temperature and chemical gradients drive metasomatic alteration, especially when

the lithologies are significantly different due to advection of a TTG adjacent to the existing mafic crust (Andreani et al., 2009; Klein and Garrido, 2011).

2.5 Alteration reactions in mafic rocks

The main processes for the alteration of mafic-ultramafic rocks are serpentinisation (Blatt et al., 2006) (hydration reactions) or talc-carbonation (Bjerga et al., 2015) (CO_2 reactions). Though the reaction pathway is not a simple single-step process (Bach et al., 2006), the general reactions during serpentinisation of mafic-ultramafic rocks can be expressed as follows (after (Kelemen and Matter, 2008; Klein and Garrido, 2011):

Fayalite: $2Mg_2SiO_4 + Mg_2Si_2O_6 + 4H_2O \rightarrow 2Mg_3Si_2O_5(OH)_4 + Mg(OH)_2$

Fayalite: $3Mg_2SiO_4 + 4H_2O + SiO_{2,aq} \rightarrow 2Mg_3Si_2O_5(OH)_4$

Forsterite: $3Fe_2SiO_4 + 2H_2O \rightarrow 2Fe_3O_4 + 3SiO_2 + 2H_2$

Pyroxene: $(Ca,Mg,Fe)_2Si_2O_6 + 2CO_2 + H_2O \rightarrow 2SiO_2 + 2(Ca,Mg,Fe)CO_3 + H_2$

This can be summarised as:

Olivine + pyroxene + carbon dioxide + water + $quartz_{(aq)}$ → serpentine + magnetite + quartz (aq) + carbonate (solid solution of Ca,Mg,Fe)

If serpentine reacts with carbon-dioxide fluxes, talc-carbonate alteration can occur as follows:

$2Mg_3Si_2O_5(OH)_4 + 3CO_2 \rightarrow Mg_3Si_4O_{10}(OH)_2 + 3MgCO_3 + 3H_2O$

Thus, the end result of hydration and carbonation of mafic-ultramafic rocks is the production of talc, aqueous silica, magnetite and carbonate (with varying solid solution composition of Ca, Mg, Fe) ± serpentine (depending on if the talc-carbonate alteration can consume all the available serpentine). Chen et al. (2005) describe komatiites pervasively altered to a dominantly chlorite ± talc ± carbonate (calcite ± dolomite ± ankerite) mineralogy

by CO_2-rich fluids. This process of carbonate metasomatic alteration of greenstones involves the addition of Ca, Mg and CO_2 and subsequent removal of Si, Na and K (Harlov and Austrheim, 2013).

In order to address the second research question a method for testing the protolith of the host rock and CAZ is needed. During metasomatic alteration there will be some trace and Rare Earth Elements (REE) that remain immobile and some that are mobile (Grant, 1986, 2005; Mori et al., 2003; Polat and Hofmann, 2003). Generally speaking the REE along with some metals like Zr, Hf, Cr are immobile species. Examining the concentration of these immobile species in the host and CAZ rock can be used to test the hypothesis that the CAZ are protolith controlled. Some authors have shown that on occasion, carbonate alteration can mobilise these typically immobile species (Lahaye et al., 1995; Polat and Hofmann, 2003). Isocon analysis is a method of identifying immobile species for a particular system and is employed in this thesis due to the nature of the extensive carbonate alteration potentially mobilising some REE that would typically be used as indicators of protolith characterisation (Grant, 1986, 2005).

Chapter 3: Methodology

3.1 Transect choice and sampling

Field mapping of two transects, T1 and T2, was completed, recording lithological contacts, structural measurements, and overprinting relationships (Figures 12, 13). Both transects cross a metre-scale zone of intense carbonate alteration bracketed by the host mafic schist. These transects were chosen because T1 exhibits densely spaced S_2 foliation within its CAZ, which, in the absence of obvious displacement markers, was tentatively interpreted as shear zone. T2, in contrast, displays a much less foliated, lithologically more homogeneous D_2 CAZ and was tentatively interpreted as a candidate for a host-rock controlled alteration zone. Both transects were mapped in detail, and oriented hand samples were collected where possible to achieve a uniform spatial sample distribution. Unfortunately, exposure is relatively poor (see Figures 12, 13), and outcrop is often obscured by regolith or vegetation.

3.2 Relative timing of carbonate alteration

To answer the first research question, field mapping involved the careful recording of overprinting relationships of deformation and alteration features to establish their relative timing and reconcile the field data with the regional deformation history established by Wiemer et al. (2016). This mesoscale work is complemented by microstructural analysis of overprinting relationships in critical samples using petrographic analysis of oriented samples. To ascertain if the carbonates were deformed rather than are present due to later replacement of existing minerals, ultra-thin thin sections (thin sections with a sample thickness of <10 µm) were prepared to better examine the textural and deformation features of the carbonate phases.

3.3 Shear- versus host-rock controlled alteration

Shear zones are defined as narrow zones of concentrated inelastic non-coaxial deformation. The CFB itself can be considered as a km-scale shear zone. However, deformation is highly heterogeneous within it, preserving lozenges of intrusive rocks and even pillow basalts locally. The CAZ of interest occur at the scale of the anastomosing shear-zone network that makes up the CFB internally. Since most of the protoliths in the CFB were meta-basalt to meta-gabbros, which have experienced very high, non-coaxial strain, displacement markers and thus clear shear-zone indicators are rarely present. Foliation density was used as a tentative proxy for increased strain in the field, identifying T1 as a candidate for a shear-zone derived CAZ. In order to estimate relative strain intensity more quantitatively, the foliation density of each transect was measured on photographs of hand specimens cut in the plane perpendicular to the S_2 foliation and parallel to the L_2 lineation. The spacing between each foliation marker (microlithons and cleavage domains) was measured using ImageJ (Schneider et al., 2012) and then plotted as inverse over distance along transect (Figure 13). In addition, microscopy was used to examine thin sections for micro-mechanisms of deformation qualitatively, which can also serve as proxy for strain intensity (Burkhard, 1993; Burlini and Bruhn, 2005; Ferrill et al., 2004). More quantitative strain gauges such as strain inversion from twins or the analysis of crystallographically preferred orientations with electron backscatter diffraction are beyond the scope of this project. Moreover, due to the complex polyphase nature of ductile deformation fabrics in the DGGB, these methods would probably yield ambiguous results.

To test for possible differences in protolith of a CAZ and its respective host rock, immobile trace-element concentrations were examined using LA-ICP-MS. An idealised expected pattern of the changes to lithology, chemistry, and strain is shown (Figure 12). If CAZ and host-rock protoliths were different, one would expect significant differences in the

content of immobile trace elements. In addition, all samples were characterised mineralogically by using a combination of X-ray Diffration (XRD) analysis for modal mineral composition along with X-Ray Fluorescence (XRF) for major oxide composition. This was necessary due to many of the minerals being at, or below the resolution of a standard petrographic microscope making identification and quantification difficult.

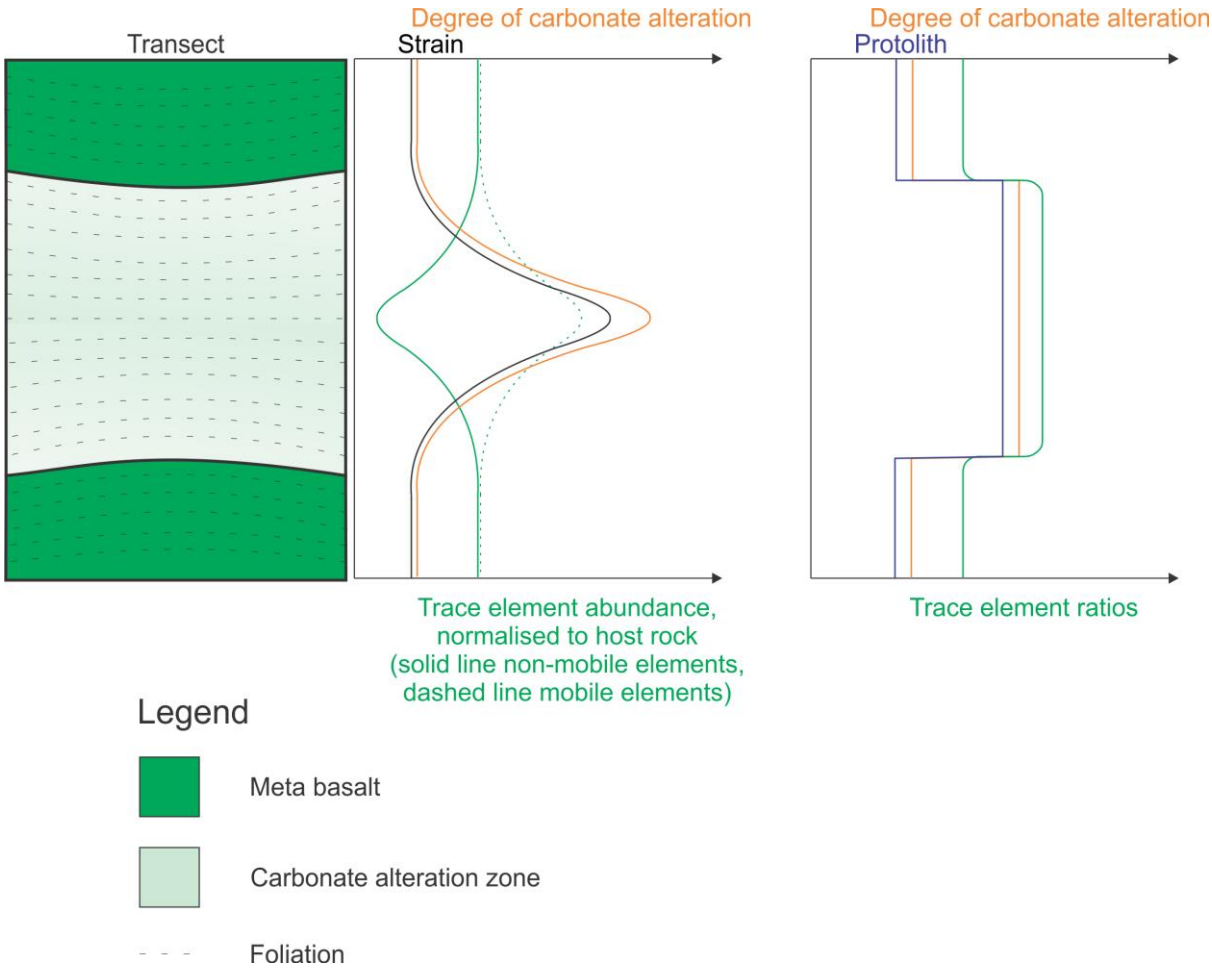

Figure 12: Idealised alteration transect. Central zone of highly carbonate altered rock surrounded by adjacent host mafic rock at upper and lower bounds. Centre of image shows an idealised schematic of the expected changes due to carbonate alteration focusing along a zone of strain localisation whereas the right side shows the expected changes if the carbonate alteration is a result of protolith difference.

3.4 Petrography

Samples were prepared at the Banyo Pilot Precinct by cutting the hand samples with a rock saw. Oriented samples were cut in three mutually orthogonal planes and labelled with the following suffices: [a] parallel to both S_2 and L_2, [b] perpendicular to both S_2 and L_2, and

[c] perpendicular to S_2 and parallel to L_2. Standard thin sections were polished to a 1-µm finish with an approximately 30 µm thickness and left without cover slips for SEM analysis. Critical samples with clear overprinting relationships between carbonate phases were prepared as ultra-thin thin sections with a thickness of < 10 µm to better identify the texture and deformation mechanisms of the carbonate.

3.5 Geochemistry

3.5.1 X-Ray Diffraction Mineralogy

Samples were prepared according to standard CARF procedures for particle size reduction (SOP_IFE_CARF 629.02-01) and mounting samples (SOP_IFE_CARF 629.11). The samples were run using a Co XRD using a step size of 0.02° through a range of 4-90° with a time of 43s/step. The incident beam path was 0.5° divergence with 2° anti scatter and the diffracted beam path was 5.0° anti scatter with 0.04 rad Soller Slits. The power used was 40kV with a 40mA current using a XPERT-PRO diffractometer system. The data analysis was completed using a combination of two software packages: HighScore 4.0 for phase identification and TOPAS version 5 for phase quantification.

3.5.2 Wavelength Dispersive X-ray Spectroscopy

Major element data was acquired by wavelength dispersive X-ray spectroscopy (WDS-XRF) analysis for 25 samples (Appendix A), carried out by Mr. Gavin Miller CARF at QUT. Standard procedures as described by Rayment and Lyons (2011) were followed for the loss-on-ignition process with slight variations in masses used due to the platinum crucible size which is machine-specific. The flux was a 50:50 lithium metaborate-lithium tetraborate at a 1:7.7 ratio of sample to flux. Due to problems of some glass discs cracking during cooling these samples were completed using a 1:15.4 ratio of sample to flux. The samples that were diluted relative to flux due to cracking are noted in the relevant table in the results section. The instrument technical specifications were as follows:

XRF specification:

WD-XRF:

- Panalytical Axios 1kw system
- Rh anode Xray tube
- 4 crystals: LIF200, PE 20mm, PX1, LIF220
- 3 detectors – Scintillation, sealed Xe and P10 flow proportional detectors
- The major element analyses were acquired using a general silicates application that was calibrated using international USGS and other 'standard' rocks.

USGS and SARM standards were used for quality assurance/quality control:

ED-XRF:

- SPECTRO XEPOS energy dispersive X-ray fluorescence (ED-XRF) 50 Watt
- Palladium X-ray tube
- The secondary targets are: HOPG (Bragg crystal), Molybdenum, Aluminium Oxide (Barkla Scatter crystal), Palladium, Zinc, Caesium, Cobalt and Zirconium (of these 8, routine use is of the HOPG, Mo and Co targets for major and trace element analyses as set up by Spectro for QUT)
- Silicon drift detector fitted with an 8 µm Be window, limiting it's detection range from sodium to uranium)
- Measurement conducted in Helium gas atmosphere

USGS standards were used for quality assurance/quality control:

Ox Fluxer:

- Claisse The Ox Fluxer for electric fusion

- 1050 °C was used for fusion

3.5.3 Laser-Ablation Inductively Coupled Mass Spectrometry

Trace element data was acquired by laser-ablation inductively coupled mass spectrometry (LA-ICP-MS) by use of CARF, QUT facilities. The process was non-standard and is detailed as follows:

- Cut hand specimens into approximately 10 g using a rock saw at BPP. Care was taken to cut away any surficial oxidised outer surface and cut surfaces were sanded to remove any potential contaminants from the rock saw. When visible, veins that clearly post-dated the D_2 event were removed to ensure that only D_2 material is considered.
- Crushed the rock to approximately 2 mm grain size powder using a hardened steel jaw crusher.
- Powdered the sample using an agate mill to approximately < 100 µm size fraction. Before the each sample was processed, the rock saw, jaw crusher and agate mill were thoroughly cleaned with compressed air and ethanol.
- Following this, the CARF SOP 629.02-01 was followed for micronizing material reducing the size fraction to < 10 µm.
    - The micronized powder then underwent a LOI procedure using 0.2000g (± 0.010g) of sample to 0.8000g of 98.5:1.5 lithium metaborate:lithium bromide flux and agitate by shaking it in a capped container till it is homogenised.
- The glass beads were mounted onto the LA-ICP-MS stage with blue-tack to ensure their position did not change during data acquisition.
- Two runs of ablation were required to be run due to the number of elements being analysed. Each run was performed with five ablation spots. The details of each run is listed (Table 1):

- Standards used to calibrate the results were NIST 610, NIST 612 and AGV-2.

	Run 1 (Oct 2015)	Run 2 (Dec 2015)
Spot size	50 µm	65 µm
Repetition rate	6 Hz	7 Hz
Energy	75%	70 %
Dwell time	30s	30s

Table 1: LA-ICP-MS run details

Chapter 4: Relative timing of carbonate alteration

4.1 Results

4.1.1 The field scale: Outcrop and hand specimen observations

Transect 1 (Figure 14) is located on the elevated Snake Ridge, near the transition from the South Muccan Shear Zone (SMSZ) to the Central Fold Belt (CBF) (Wiemer et al., 2016). The CAZ is approximately 3 m wide and bounded by a moderately foliated mafic schist to the north and south. The mafic schist is altered and very fine grained making field identification of the mineralogical make up difficult. From field observations the mineralogy appeared to be dominantly carbonate and chlorite with occasional ghosts of plagioclase laths and oxides with carbonate and quartz veining cross cutting the host rock. Geochemical analysis in section 5.2.1 confirmed the field observations and quantified this mineralogy. Transect 2 (Figure 15) is located approximately 200 m South of Transect 1 within the CFB, and is comprised of a north and south mafic schist bounding a pervasively carbonate altered zone. The carbonate alteration zone in Transect 2 is approximately 8 m wide and macroscopically appears more homogenous and less foliated than Transect 1.

A penetrative, steeply dipping, approximate E-W trending foliation is observed throughout both transects which is defined in hand specimen by a strong SPO of chlorite and carbonate minerals. The greenstone forms topographic ridges on the metre scale relative to the recessive carbonate where weathering and erosion appear concentrated.

The greenstone never overprints the carbonate material. It is pervasively veined by both carbonate and quartz veins with vein widths ranging from millimetres to tens of centimetres. Rare ghosts of plagioclase ± pyroxene crystals can be seen away from the mapped transects on ridge outcrops of intrusive mafic rocks.

Measurement of the foliation densities of each transect confirms the qualitative field observation which motivated the choice of transects. T1 shows an increase in foliation density within the CAZ whereas T2 shows a more homogenous to somewhat decreased foliation density within the carbonate alteration zone (Figure 13).

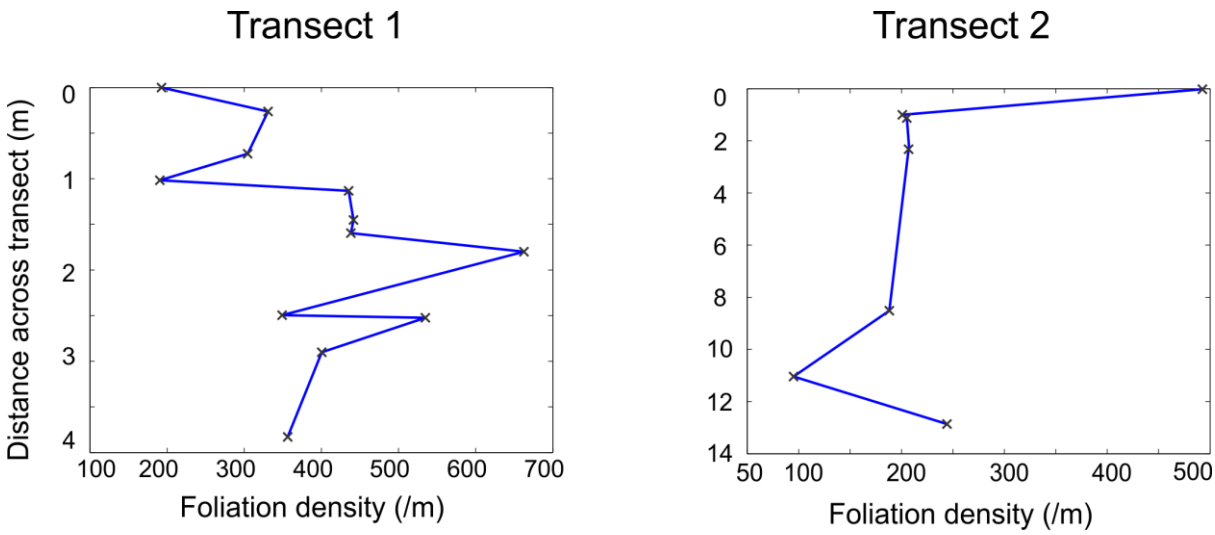

Figure 13 Foliation density measurements from Transect 1 and 2. Measurements taken from image analysis on cut hand specimens viewing the plane perpendicular to the D_2 foliation and parallel to the lineation

Within the carbonate alteration zones multiple generations of carbonates are observed. The subscripts used for foliation, veining and deformation will follow the nomenclature established by Wiemer et al. (2016).

4.1.1.1 D_2 characteristics

From field and hand specimen observation the oldest observed carbonate, C_2, appears to be aphanitic, grey-white material that shows local foliation running E-W. It is typically found near the centre of the alteration zones.

The progressive nature of the D_2 event is illustrated by the limbs of tight carbonate folds being transposed during deformation, resulting in rare hinge closures (Figure 16). The overprinting and relative age relationships are confirmed by the petrographic analysis presented below. Figure 17 shows an F_2 crenulation folds of consisting of alternating layers

of orange ankerite and a grey anomalous carbonate + quartz matrix showing S_2 foliation. The accompanying photomicrograph shows that the stretched C_2 carbonate minerals are clearly folded around the hinge. They present evidence of crystal-plastic deformation by grain size reduction, stretching and a strong SPO forming the S_2 foliation.

4.1.1.2 D_3 Characteristics

Figure 14 shows the overprinting relationship between D_2 and D_3 in the field which is observed as F_2 tight folds being overprinted by gentle F_3 folds. The C_2 material is overprinted by carbonate C_3 that shows clusters of euhedral to subhedral crystals typically 1 to 2 mm but up to 5 mm in size. The overprinting relationship between these two carbonates is best exposed in T2 (Figure 15).

4.1.1.3 D_4 Characteristics

C_4 carbonates appear as cataclasites with as sub-angular to sub-rounded clasts of older carbonates from 2 mm to 30 mm in size in a fine-grained, grey-white carbonate matrix. The width of the C_4 cataclastic zones in map view ranges from 0.1 to 0.75 m. They trend NS and generally cross-cuts the regional foliation. This can be seen in T2 but is also observed in other CAZ throughout the CFB. Displacement markers for C_4 cataclasites were absent. A hand specimen shows a younger carbonate vein cross cutting the S_2 foliated layers of chlorite cleavage domains and the red-brown ankerite microlithons (Figure 18). The younger carbonate is blocky, lacks any SPO or foliation typical of the older generation.

The C_4 cataclastic carbonate can be observed cross cutting all other phases, typically showing a north-south trend ranging in width from metre scale (Figure 15) to millimetre scale (Figure 18). It is dominantly composed of ultrafine grained carbonate matrix and contains angular to sub-angular clasts of older carbonate ± quartz clasts indicating it postdates the other phases.

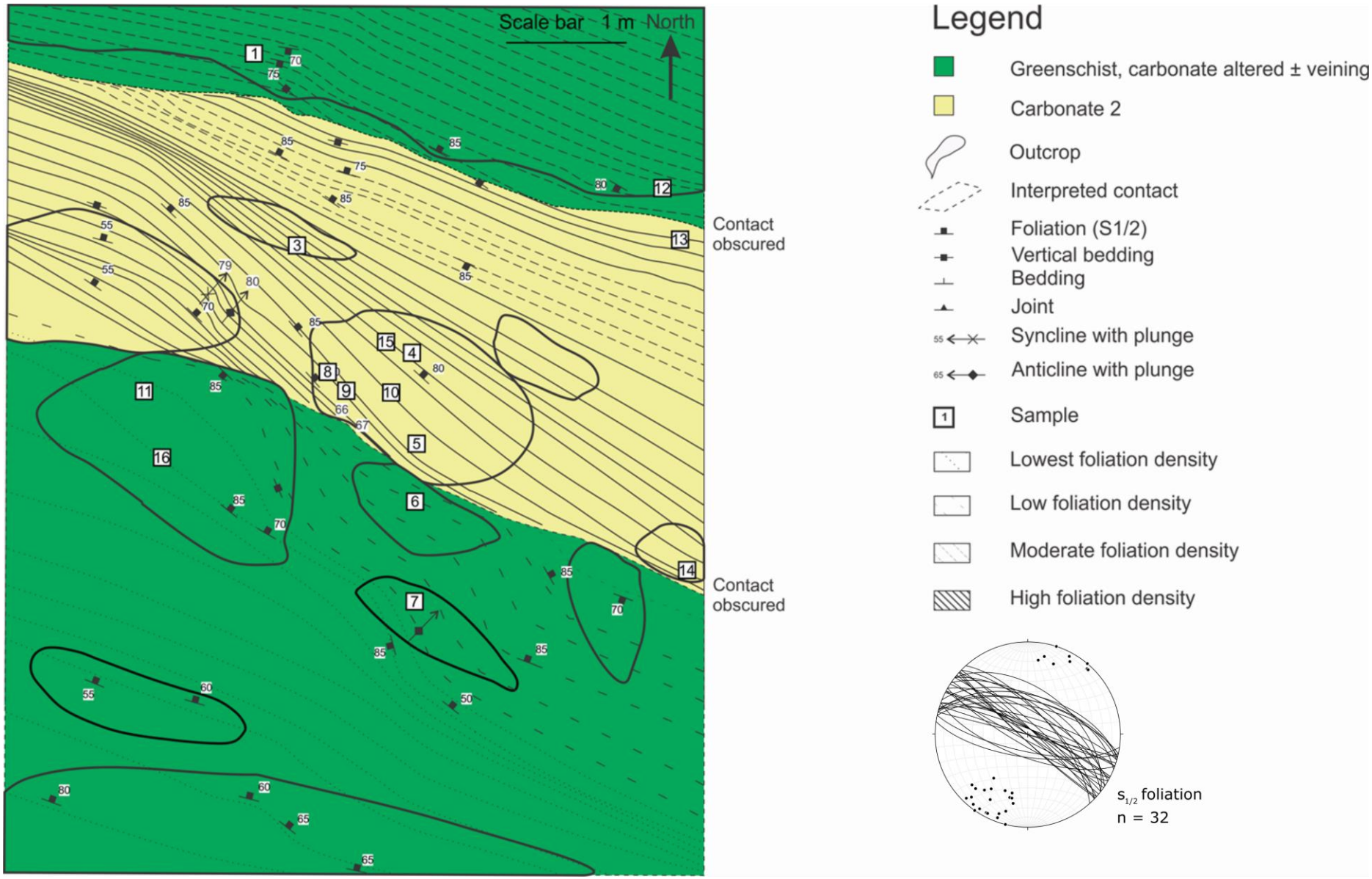

Figure 14 Transect 1 litho-structural map with sampling locations and extent of outcrop

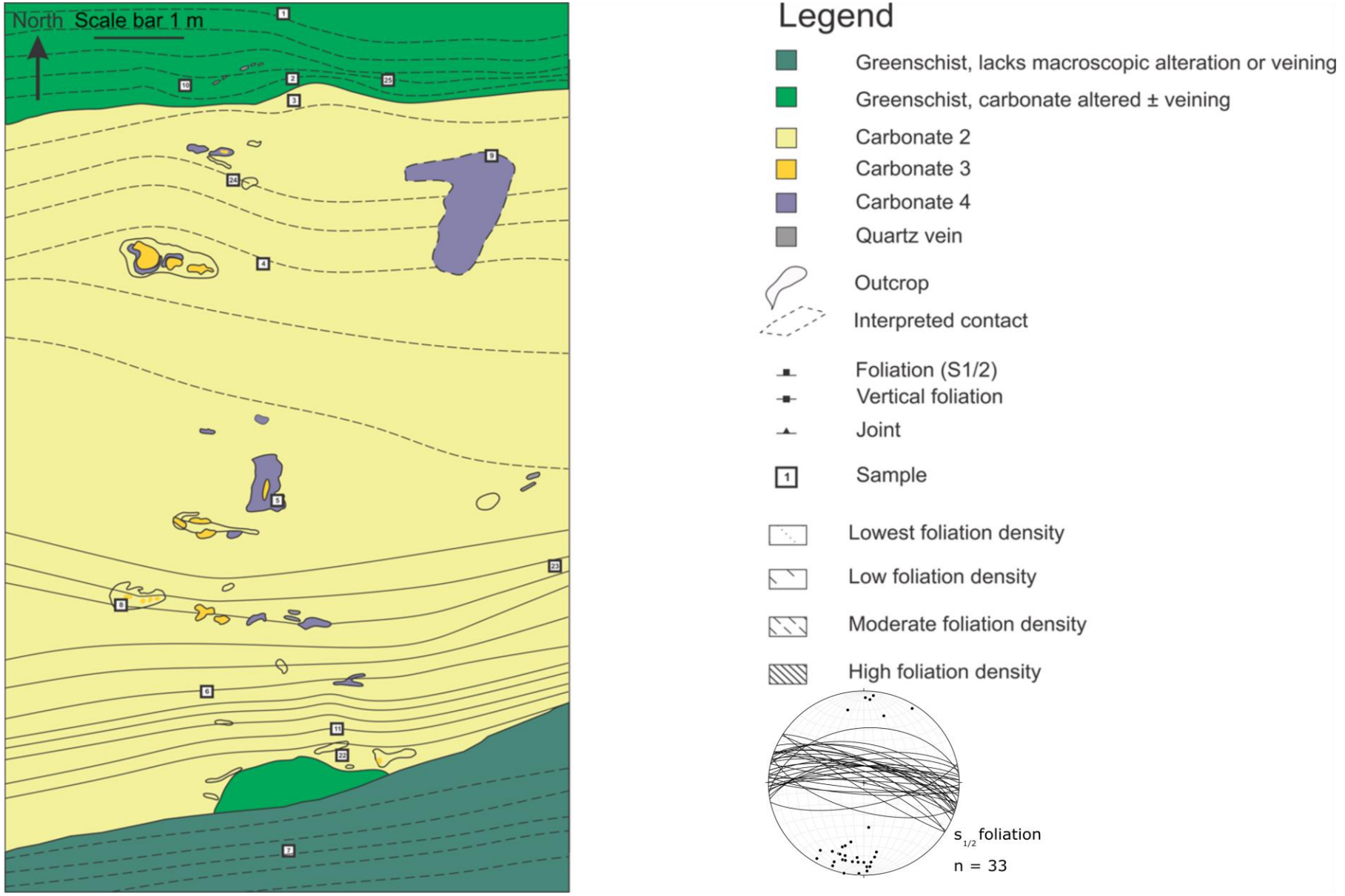

Figure 15 Transect 2 litho-structural map with sampling locations and extent of outcrop

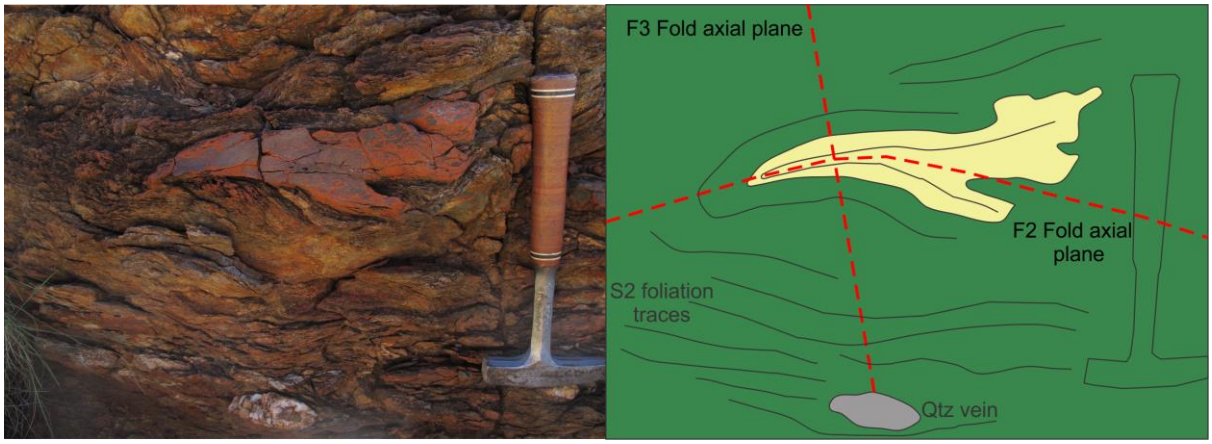

Figure 16 Field photo of a tight F_2 folded carbonate overprinted by a gentle F_3 fold. Rock hammer gives scale. (Modified from a photo by Schrank, (2016 personal communication))

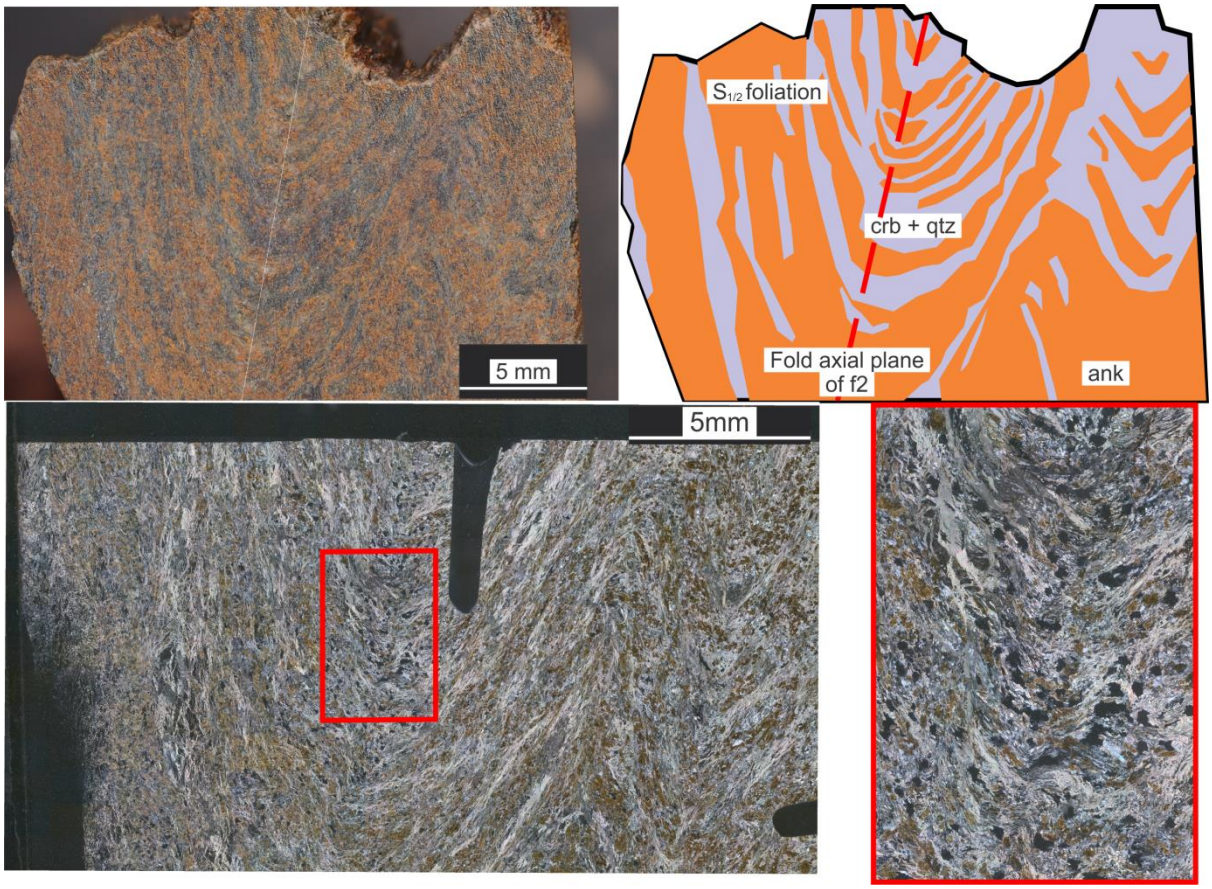

Figure 17 Photograph of F_2 folded carbonate and interpretative sketch. Associated thin section and detailed inset of the bands of ankerite and carbonate + quartz. Sample 2-22b, photomicrograph is in XPL, sample prepared perpendicular to both S_2 and L_2.

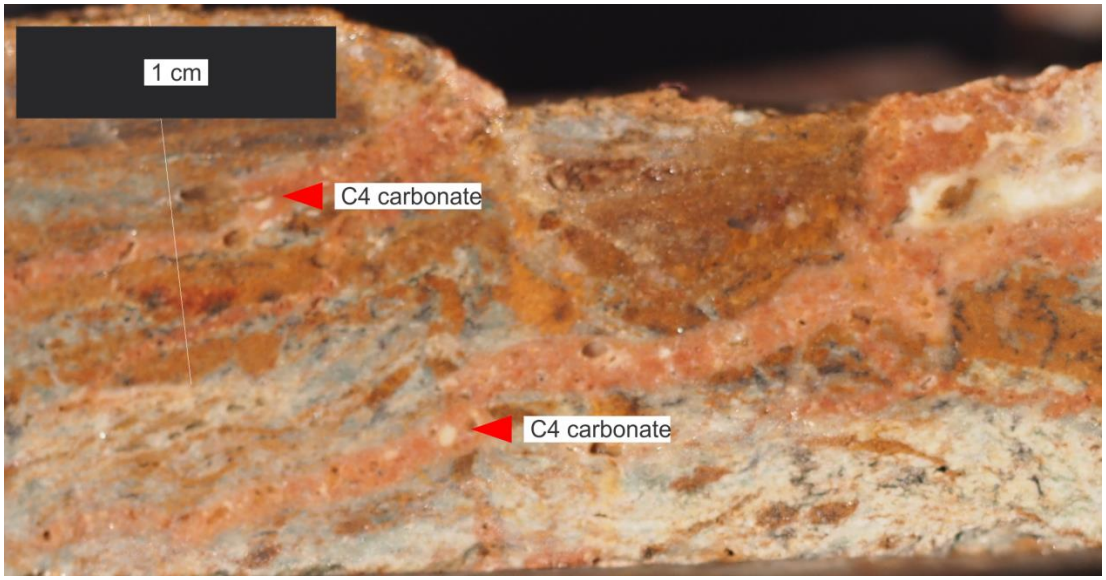

Figure 18 Photograph of C_4 carbonate cataclastite containing sub-angular clasts of older carbonate Sample 1-5

4.1.2 The micro-scale: petrographic results

4.1.2.1 D_1 characteristics

In both transects, D_1 structures could not be observed. This is not surprising, given the high deformation intensity of D_2, which reactivated and overprinted S_1 foliations, as shown by Wiemer et al. (2016).

4.1.2.2 D_2 characteristics

D_2 structures are characterised by a spaced foliation of gradational, wriggly, anastomosing cleavage domains defined by microcrystalline (~20 µm wide grains) quartz ± chlorite ± carbonate (Figures 19, 20, 21) and microlithons of stretched ankerite ± dolomite, typically 1 mm long and < 250 µm wide,. Up to 20 µm wide type-II twins (Burkhard, 1993) are common in the carbonates making up the micro-lozenges which the finer grained material surrounds. In rare cases type-III curved twins are observed. These carbonates also show sweeping, undulose extinction and curved to lobate grain boundaries. The cleavage domains show evidence of dynamic recrystallisation resulting in grain size reduction of both the carbonate and quartz fraction. Quartz displays stretched grains with bulging (BLG) and sub-grain rotation (SGR) (Figures 19, 20) dynamic recrystallisation (Passchier and Trouw, 2005;

Stipp et al., 2002). A strong SPO of the carbonate and chlorite (Figure 19). Twinning of carbonates in the cleavage domains is not observed. Hinges of tight to isoclinal F_2 folds can be observed in thin section. C_2 carbonates are clearly folded around these hinges (Figure 19). Within Figure 19b, note the location of (1) and (2) in the ultrathin photomicrograph. It can be seen in the left limb (1) that the carbonate grain size is increased, extinction is less sweeping, grain geometry is approaching straight rather than lobate, and twinning is observed suggesting later recovery processes. The right limb (2) shows carbonate that has undergone grain size reduction, shows strongly sweeping extinction and grain contacts are lobate to undulating indicating intense ductile deformation. Point (4) shows that the F_2 carbonate has overprinting microcrystalline quartz. Figure 19c point (1) again shows the F_2 quartz with significant grain size reduction overprinted by F_2 carbonate.

Local heterogeneity in the characteristics is sometimes observed (Figures 22, 23). Variability in the carbonate grain size can be seen though the textures and fabrics are conformable to adjacent D_2 fabrics.

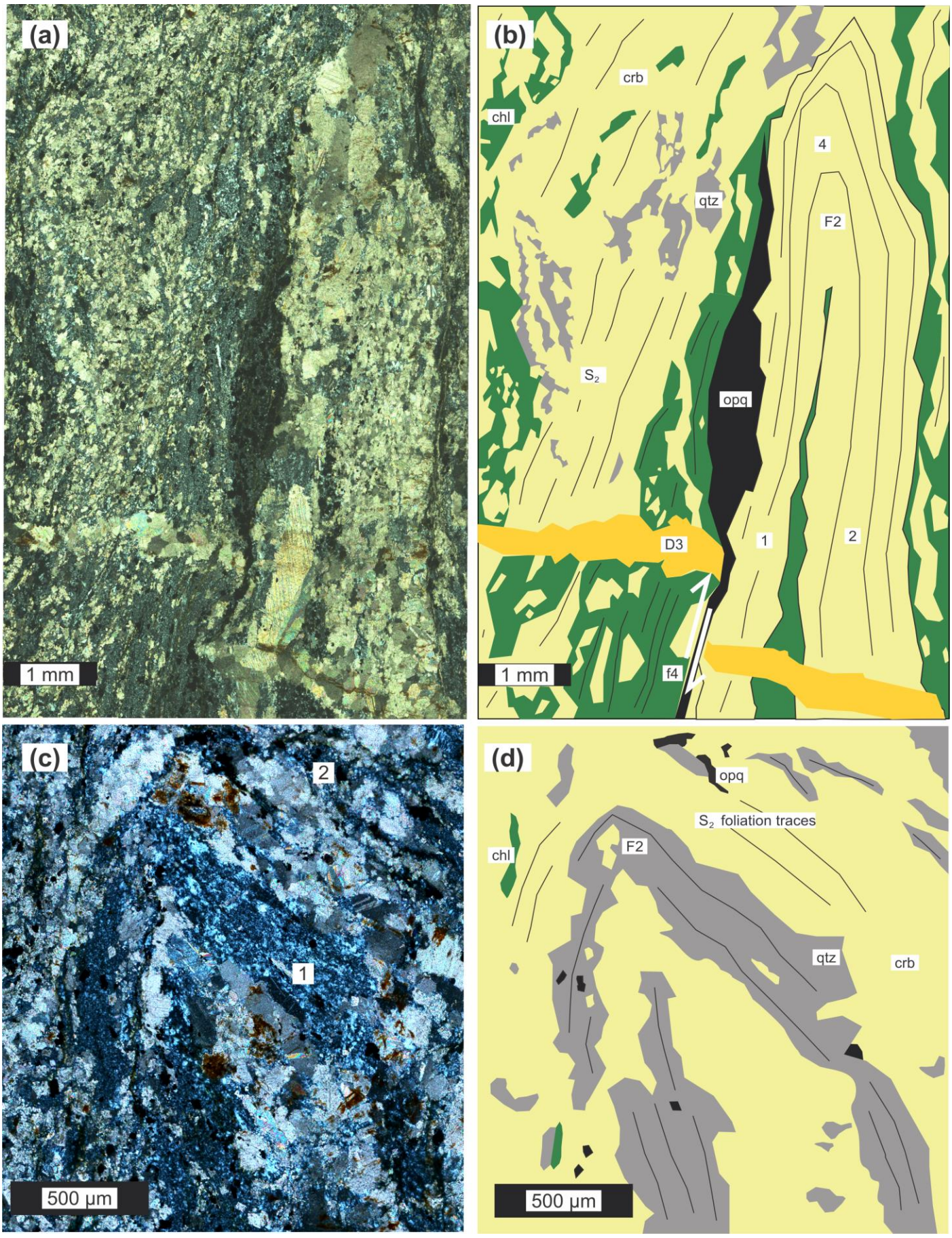

Figure 19: a) Ultrathin photomicrograph of F_2 folded carbonate cross cut by D_3 carbonate vein which is later offset in a dextral fashion by a f_4 micro-fault. b) Interpretative sketch of (a) illustrating overprinting relationships. c) Detail of just above the hinge at the top of (a). Saturation was changed to improve texture visibility. Quartz and carbonate show a strong SPO. d) Interpretative sketch of (c) showing strong SPO of carbonate and quartz. Slide 2-2c, XPL, slide prepared perpendicular to S_2 and parallel to L_2.

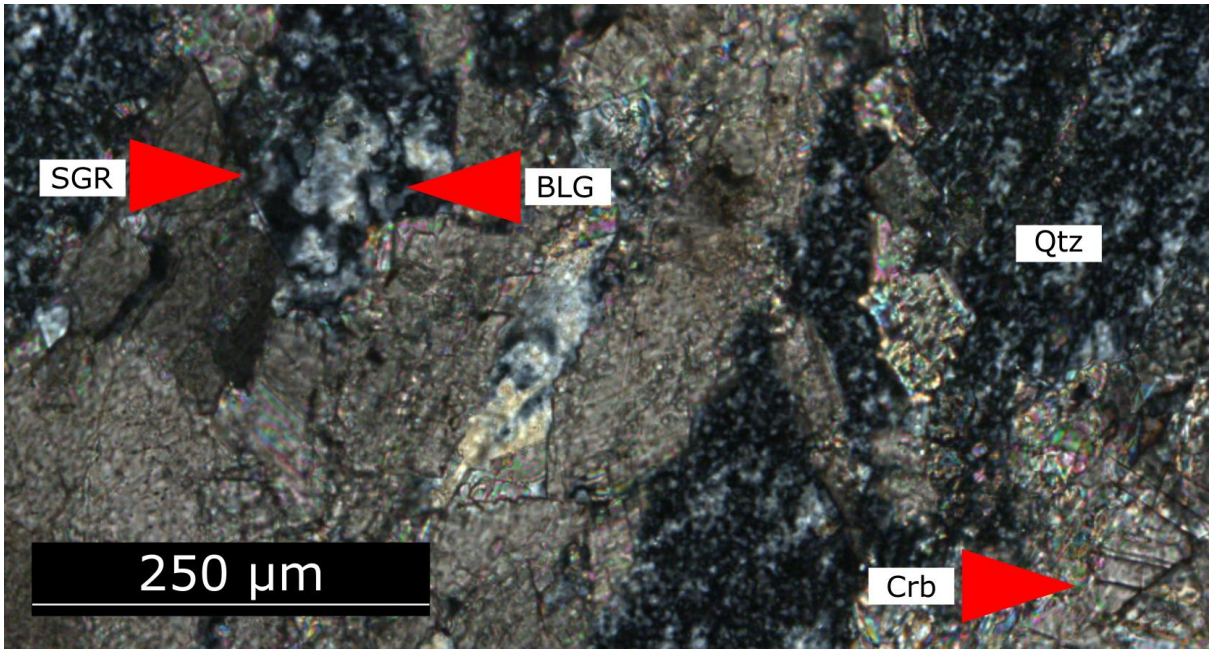

Figure 20: Photomicrograph showing evidence of the dynamic recrystallisation of quartz resulting in grain size reduction by bulging (BLG) and sub-grain rotation (SGR) processes. Sub-grains are being formed as indicated with the misorientation of the quartz extinction. Bulging recrystallisation as indicated by the lobate contacts. Extensive grain size reduction of quartz is visible in the top left and right of the micrograph however due to the very fine grain size approaching the resolution limit of a petrographic microscope clear identification of the processes at work is uncertain. Carbonate shows thick, type-II twins and forms micro-lozenges surrounded by the quartz. Carbonate crystal geometry ranges from dominantly sutured, however some rare straight contacts are visible. Carbonate extinction is undulose. Slide 2-2c, XPL, section perpendicular to S_2 and parallel to L_2, S_2 foliation runs top to bottom in image.

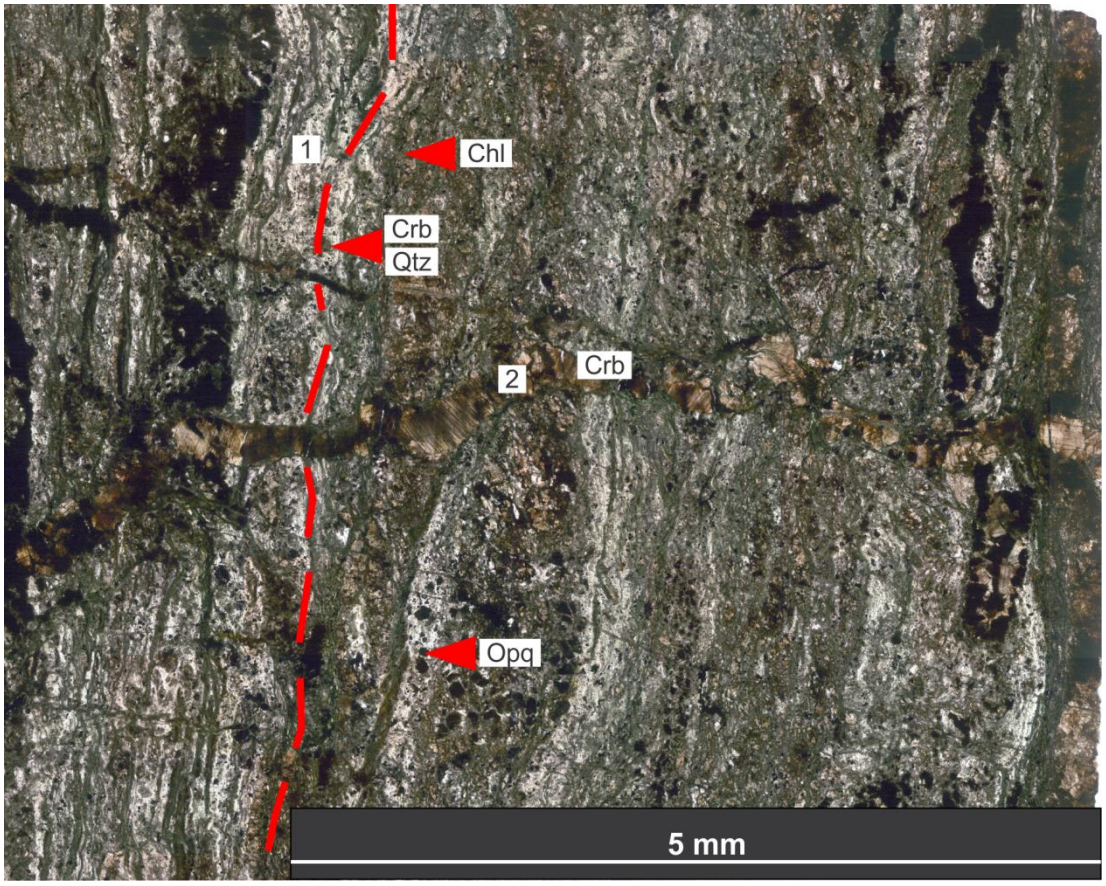

Figure 21: Slide 2-1b illustrates the S_2 foliated carbonate + quartz + chlorite being overprinted by a C2 carbonate vein 1) Trace of S_2 in red with s strong SPO of the minerals which defines the foliation. Opaques are euhedral-subhedral and found within the S_2 foliated material, being almost entirely absent in the D_3 vein. 2) A D_3 carbonate vein that cross cuts the foliation and shows typical D_3 textures described in text; large crystal size (~200 um), common type II twinning and minor-absent undulose extinction. Slide 2-1b, XPL, section perpendicular to both S_2 and L_2. Top of image is approximately west, D_3 vein runs approximately N-S.

4.1.2.3 D_3 characteristics

C_3 carbonates are mainly emplaced within veins. Figure 19 shows a C_3 vein that cross cuts an isoclinally folded C_2 carbonate, later offset dextrally by a micro-fault. Syn-D_3 carbonate is observed as gentle-openly folded veins with larger crystal size (~200 µm) and frequent to pervasive type II twinning (Burkhard, 1993; Ferrill, 1991; Ferrill et al., 2004) (Figure 21).

There are D_3 quartz veins emplaced (Figure 24) that show evidence of later recovery, namely straight grain boundaries and clear extinction. Rare BLG recrystallisation of these veins can be observed.

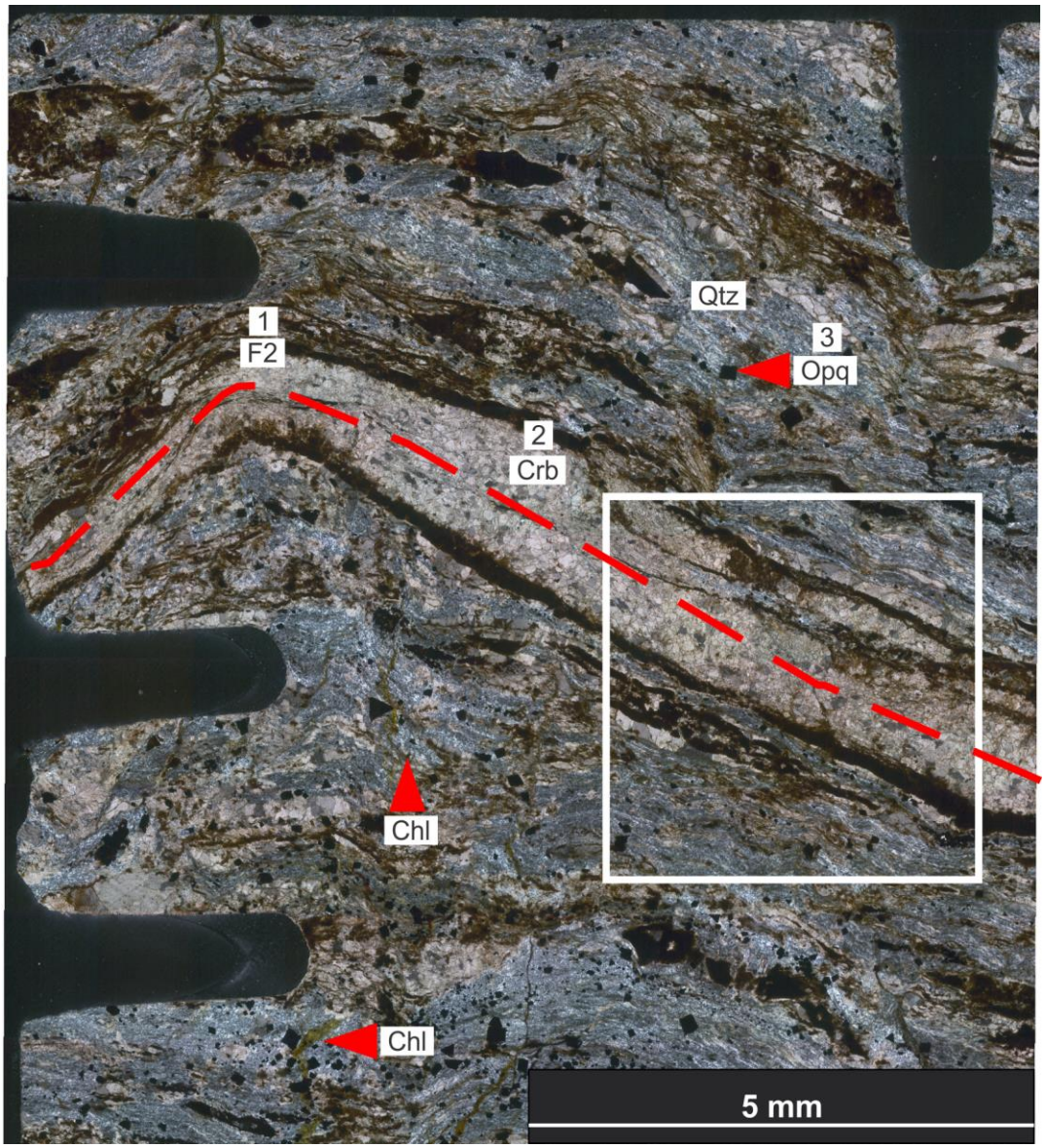

Figure 22: 1) Red dashed line shows trace of F_2 fold axial plane, showing folding of the S_2 foliation. 2) The D_2 carbonate shows local textural heterogeneity of some larger crystals. 3) Later D_4 euhedral opaque minerals can be seen to be dominantly within the microcrystalline quartz zones, overgrowing the existing quartz. Slide 1-16c, XPL, prepared perpendicular to S_2 and parallel to L_2. White box locates Figure 23

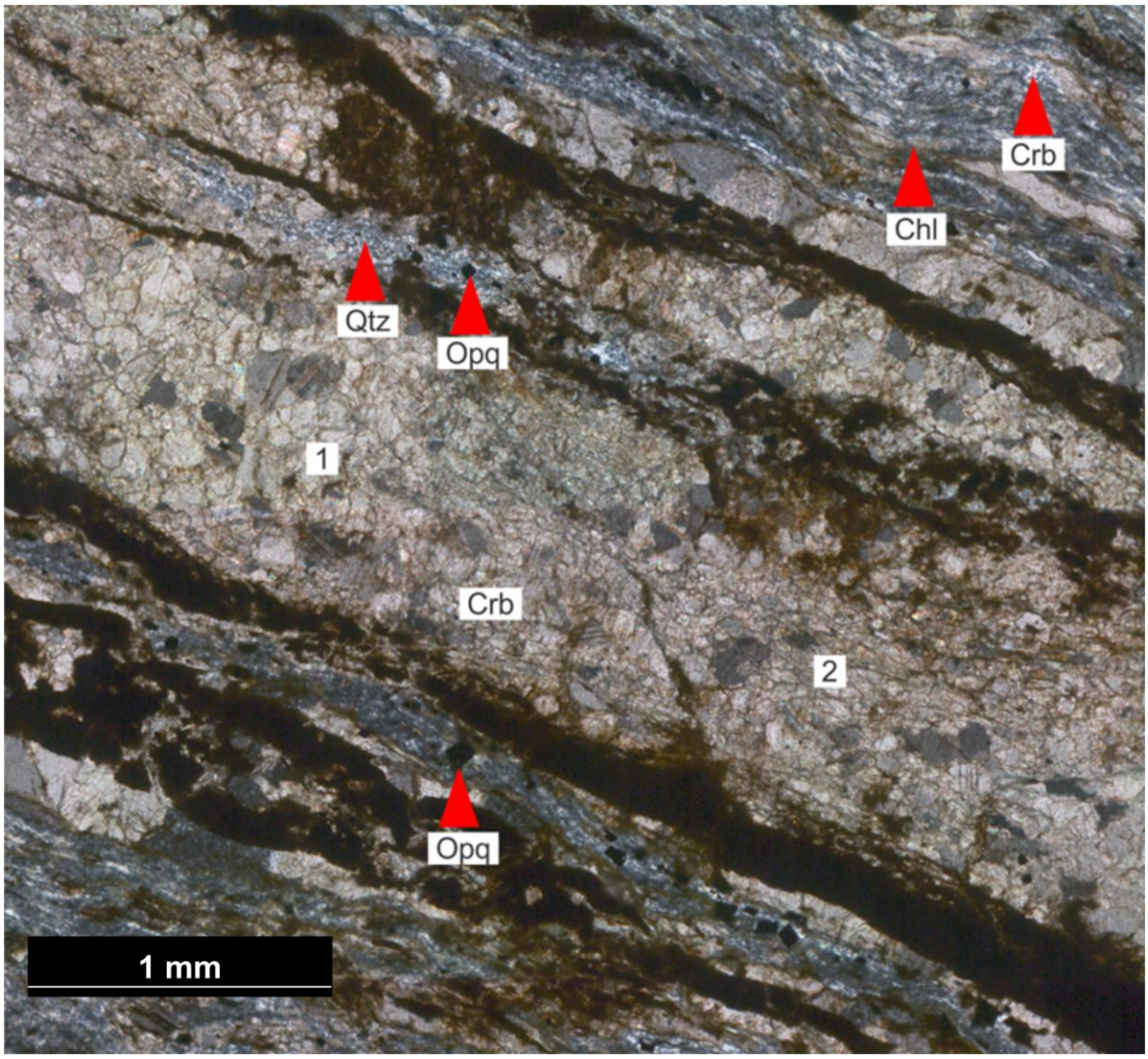

Figure 23: Photomicrograph of inset in Figure 22. 1) Local heterogeneity as evidenced by occasional larger carbonate crystals. Twinning is common and sweeping extinction is observed. 2) S-C fabric within the carbonate that is conformable with the adjacent S_2 foliation. Thin brown slip surfaces are observable at the margins of the carbonate above and below the (2) marker. Opaques are euhedral to subhedral and overgrow the microcrystalline quartz fraction suggesting they are a late feature. Sample 1-16c, XPL, same orientation as Figure 22

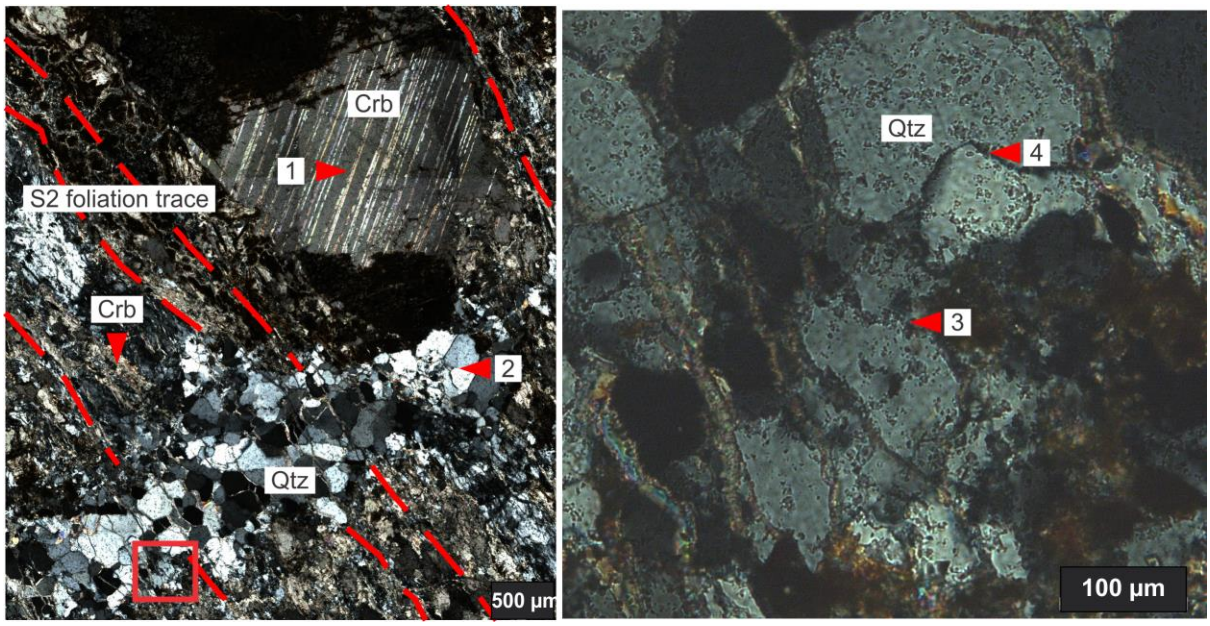

Figure 24 a) Photomicrograph showing cross cutting relationship between S_2 foliated carbonate and D_3 quartz vein. 1) Carbonate shows thick type II twins extending across the entire crystal face. S_2 foliation defined by carbonate with elongate, strongly SPO crystals. 2) Evidence of annealing of the quartz by grain boundary area reduction processes as crystal boundaries are straight as opposed to lobate or sutured and extinction is no longer undulose. Note that many quartz crystals seek triple point junctions with angles of approximately 120° which is typical of the annealing process. Red box shows inset of detail 3) Incomplete annealing that preserves BLG texture as evidenced by lobate contacts bulging into adjacent quartz grains, approaching the limit of the resolution of the microscope but becomes more obvious when compared to 4) Straight, annealed crystal contact to illustrate the difference with the preserved lobate contact of (3). Slide 1-7, XPL, section prepared perpendicular to S_2 foliation and parallel to L_2.

4.1.2.4 D_4 characteristics

C_4 carbonates are generally cataclastites with angular to sub-angular fragments of older carbonate and quartz ± chlorite. Their contacts vary from sub-parallel to S_2 to cutting it at high angles (Figure 25). The contact between older host rock and this D_4 carbonate is sharp and the cataclastite shows a decrease in abundance and size of older clasts towards the contact. Euhedral to subhedral D_4 Fe-Ti oxides, typically 50 µm, overgrow the microcrystalline D_2 quartz material (Figure 22).

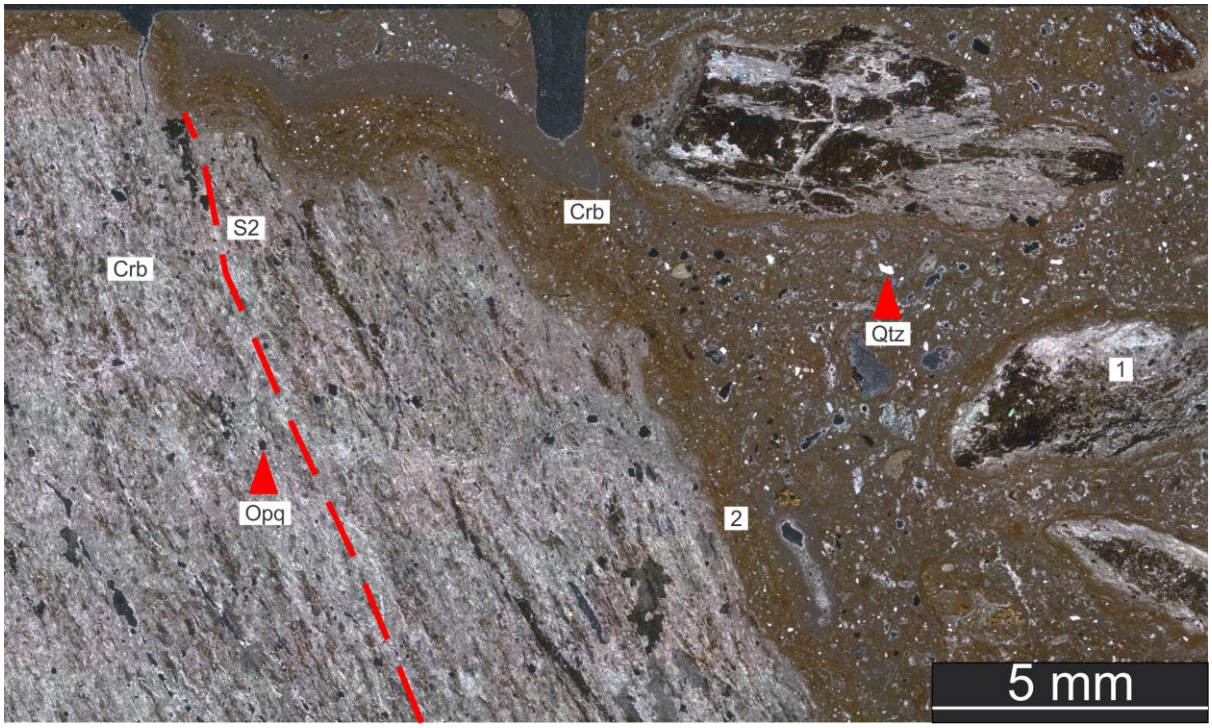

Figure 25: Near vertical S_2 foliation cut by a D_4 cataclastic carbonate which contains sub-angular clasts of quartz and carbonate material preserving S_2 foliation (1). 2) Note the decrease in clast size and abundance moving towards the contact, ie from (1) to (2). Slide 1-10b, XPL, slide prepared perpendicular to both S_2 and L_2.

4.2 Discussion

To determine the relative timing of carbonate alteration, overprinting relationships have been established along with textural evidence to test if the carbonates attributed to a particular deformation event are not a later feature preferentially replacing an existing mineral as a pseudomorph. Based on the field mapping, hand specimen and petrographic observations, the following can be established with high confidence.

[1] Primary carbonate is formed and preserved in the interstices of pillow basalts (Figure 9) and therefore likely contributes significantly to the carbonate budget of this greenstone keel.

[2] S_2 contains C_2 carbonates interpreted to be pre- to syngenetic with D_2. They make up at least 50 % of the S_2 foliation and appear in the isoclinal to tight F_2 folds on the outcrop

(Figure 16), hand specimen (Figure 17), and thin-section scale (Figures 17, 19a and c). Their stretched shapes making an SPO with S_2, SC-fabrics (Figure 23), and their microstructures are indicative of penetrative crystal-plastic deformation by twinning (types II and III) and dynamic recrystallisation. At the latest, C_2 carbonates must have formed early during D_2, which has been established as a protracted progressive high-strain event (Wiemer et al. 2016) or even earlier. If they are derived from seafloor or near-surface metasomatism of extrusive protoliths or metasomatic processes deeper in the crust cannot be assessed with the current information.

[3] D_3 is associated with C_3 carbonate veins and quartz. The former show type-II twins, the latter annealing fabrics and relict BLG recrystallization. This suggests that they experienced ongoing crystal-plastic deformation at somewhat elevated temperatures after their brittle emplacement. However, qualitatively, strain intensity in D_3 veins is significantly lower than in D_2 structures.

[4] C_4 carbonates are rare in the studied transects and appear in cataclastic faults and micro-faults (Figure 25). They do not exhibit a discernible ductile overprint and appear to be dominantly brittle structures.

Therefore, it is established that carbonate alteration occurred throughout the entire deformation history of the DGGB. The following discussion will address the possible significance of the large proportion of crystal-plastically deformed carbonates for the keel formation event D_2.

As shown in the following chapter (Figure 26), the proportion of carbonates within the CAZ ranges from ca. 50 to 60% while it is generally $\leq$ 30% in the host rock. These carbonates show intense crystal-plastic, i.e., ductile, deformation as do the associated tectosilicates, and must have been emplaced prior to or early on during the sagduction of the

greenstone keel. Therefore, it can be expected that they have a large impact on the effective rheology of the keel. This is discussed in the next chapter.

Chapter 5: Are the carbonate alteration zones host rock controlled or induced by a coupled strain localisation processes?

Geochemical analysis was carried out to characterise and compare the samples in the light of the question: do the CAZ and the host rock stem from the same protolith? As the rocks are Archaean and underwent multiple phases of deformation and exposure, alteration is likely to obscure much of the original geochemistry. Therefore, any meaningful geochemical analysis must be made on species, which can be shown to be immobile during alteration. Based on the field, hand specimen and petrographic analyses, it is clear that the multiple deformation and metasomatic events have obliterated any primary textural evidence, which may have assisted in identifying definite characteristics of different protoliths.

5.1 Results

To characterise the mineralogy and chemical composition samples geochemical analysis was performed. The focus of this study is on the major overturn event D_2, as both CAZ dominantly consist of S_2 foliations samples were filtered during preparation to remove later veining or late stage alteration minerals so that the geochemical data relates to D_2 minerals only.

5.1.1 X-Ray Diffraction (XRD): bulk mineralogy

The results of the XRD analysis for both transects are presented as function of their distance across each transect (Figure 26). The lithological field context is denoted by the background shading. It should be noted that the lithological contact was obscured in places, especially in T1, and this is reflected by the dashed line. The plots group all carbonates (calcite, Mg-calcite, dolomite and ankerite) together to aid visualisation, and the breakdown of mafic/ultramafic rock forms a solid solution of carbonates (Chapter 2).

Carbonates are typically < 30 %, but can make up to 50% in the host rocks of both transects, in agreement with petrographic analysis (Figures 19, 20, 21). The second most common mineral is quartz with percentages between 20 and 40%. The third most common phase is chlorite with amounts of 10 to 20%, as expected in the host rock. Within both CAZ, there is an increase in the carbonate fraction up to 60%, and associated decrease in both quartz and chlorite abundance down to a minimum of 2% and 5% respectively. The relative depletion of chlorite likely explains the distinct colour change, which aided lithological contact identification during field mapping. Talc is almost entirely found within the CAZ. There is a high fraction of non-diffracting material throughout both transects, up to 35%. The non-diffracting material could be either organic or amorphous clays. Based on the complete lack of organic material observed in the petrographic analysis it is likely that the non-diffracting material reported is entirely composed of amorphous clays. As the focus of this study is on the D_2 event, the type of clay resulting from late stage alteration and weathering is not important to this study and further identification is outside the scope.

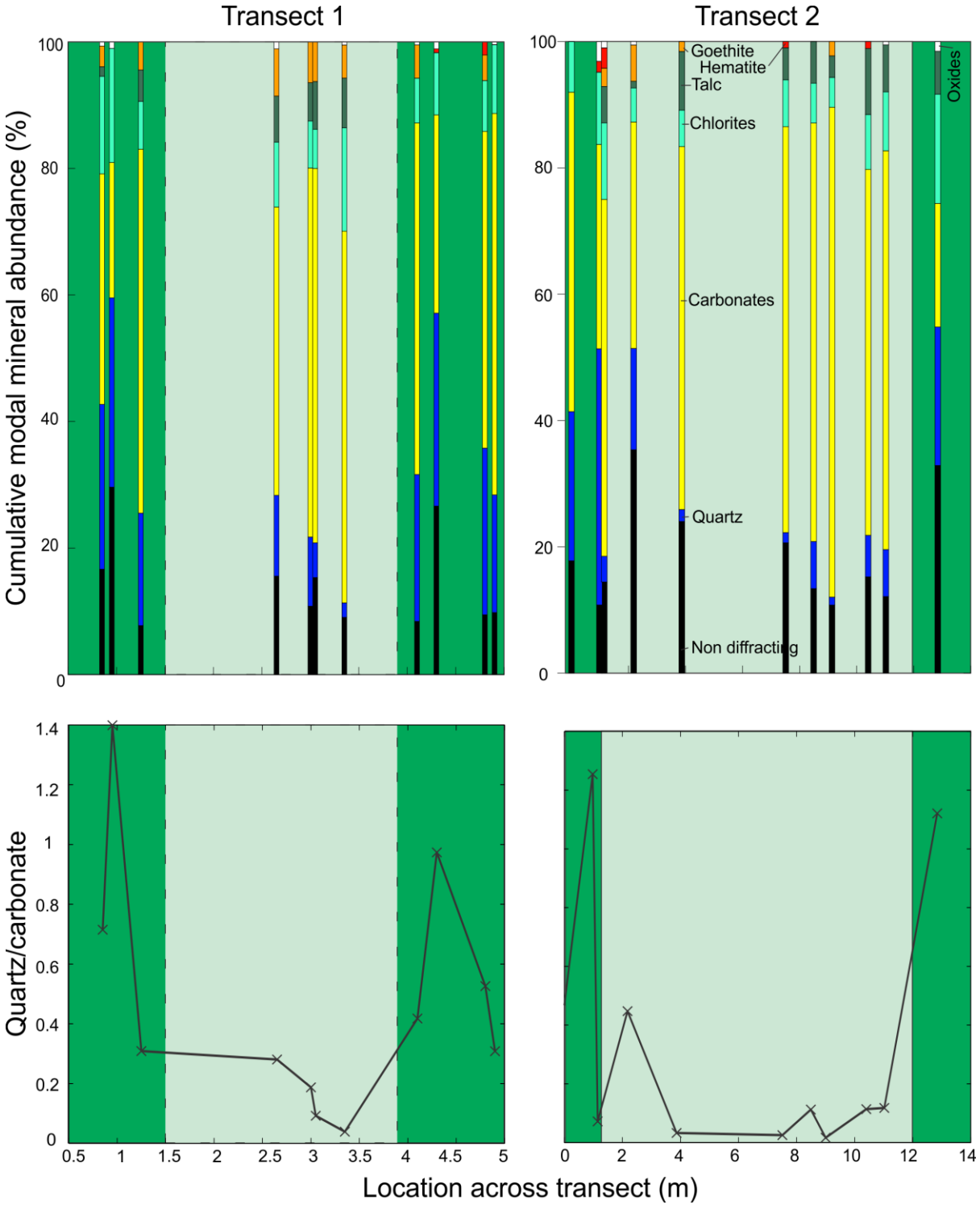

Figure 26 XRD analysis of Transect 1 grouped by type of mineralogy. Dark green background is the extent of the host rock and central light green is the CAZ. Note the inferred lower contact and lack of sampling due to poor outcrop. See Appendix A for data

5.1.2 WDS-XRF analysis: major and minor oxides

The results of the WDS-XRF analysis for major and minor oxides for both transects are presented as function of distance across each transect (Figure 27). The changes observed in major oxides across the CAZs are a decrease in SiO_2 by ca. 20 %, increase in CaO by ca. 10 % in T1 and ca. 20 % in T2. A minor increase in MgO is observed in both transects but there is scatter in the data. Fe_2O_3 seems to be ca. 5 % more common in the host rock of both transects than the CAZ. However it is clear that the trend in the data is ambiguous.

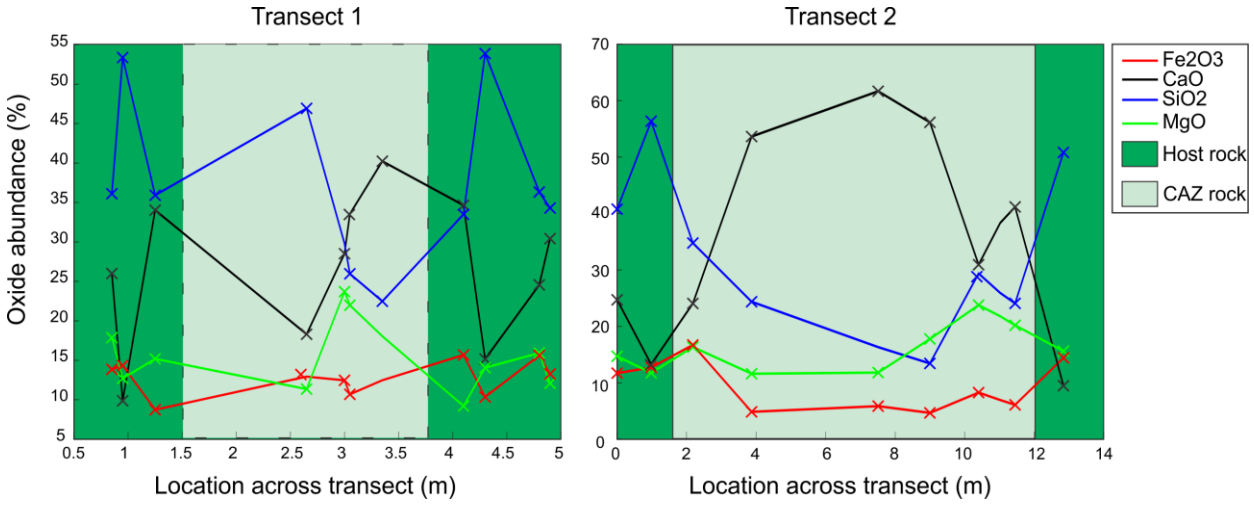

Figure 27 Major oxides of Transect 1 and 2 plotted against spatial position along transect. Dark green shading shows the extent of the host rock and light green indicates the CAZ. See Appendix B for data

5.1.2 Oxides in Harker diagrams: comparison to less deformed pillow basalts up sequence

Figures 28 and 29 are Harker diagrams comparing the major element oxides of Transect 1 and 2 plotted against MgO to the Mt Ada basalt to place the later geochemical interpretation in context. The Mt Ada basalts (MAB) overlie the CFB in the Low Strain Belt and are less deformed and altered than the rocks studied here. Some lozenges of the CFB preserve remnants of pillow basalt. Therefore, it is instructive to compare the host rock and CAZ of the studied transects to relatively fresher pillow basalts from the same greenstone keel. Typically, Harker diagrams show other major oxides such as Na_2O, K_2O, Al_2O_3.

However, in this study, they were completely depleted from both the host rocks and the CAZ and thus omitted.

In T1 (Figure 28), samples of both host and CAZ rock have experienced significant depletion in SiO_2 (of the order 30-50 % loss) relative to the less deformed overlying MAB. TiO_2 abundance in the host-rock samples is similar to the lower concentrations of the MAB. However, the CAZ samples are depleted in TiO_2 with increasing MgO abundance. Fe_2O_3 has similar concentrations within the host rock relative to the MAB but has similar to slightly depleted relative abundance within the CAZ. Relative to the MAB, CaO has been enriched in the host rock and highly enriched in the CAZ with increasing MgO content. This is consistent with the XRD analysis, which shows an increase in modal carbonates. Cr_2O_3 concentrations in T1 are similar to the highest recorded values of Cr_2O_3 in the MAB. The host rock has a slightly higher average concentration of Cr_2O_3 relative to the CAZ. However, all samples of the transect exhibit comparable or greater concentrations of Cr_2O_3 than the maxima measured in the rest of DGGB .

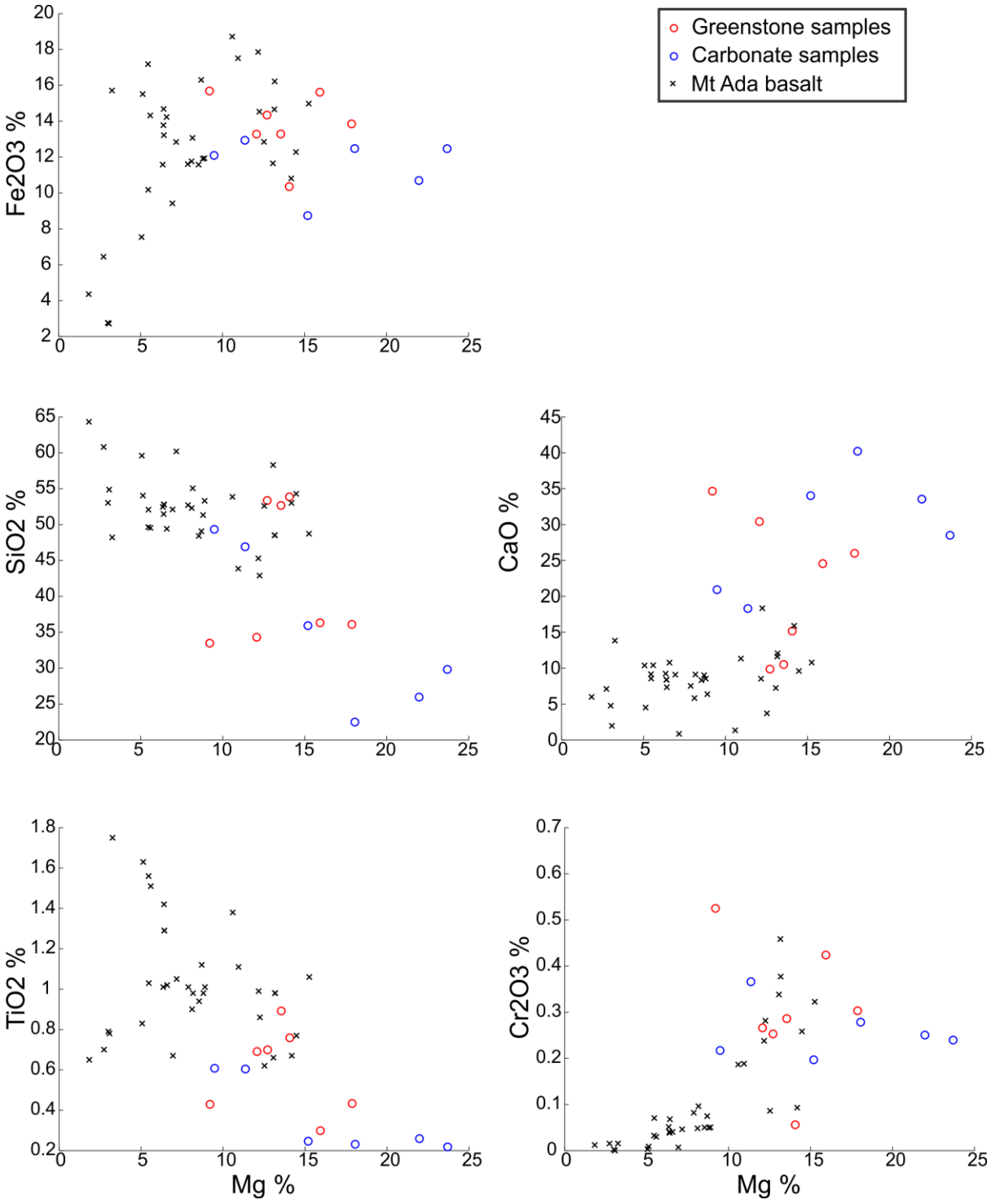

Figure 28 Harker diagrams of major elements plotted against MgO for Transect 1 with comparative chemistry of the Mt Ada basalt.

Overall, the Harker diagrams for T2 (Figure 29) shows similar trends in the host rock as T1. Relative to the MAB, there is a clear trend of SiO_2 depletion (of the order 20-50% depletion). The abundance of TiO_2 in T2 host rock is similar to the lower concentration within the MAB, and the CAZ shows depletion. The Fe_2O_3 abundance in the host rock has similar concentrations relative to the MAB but shows clear depletion within the CAZ. The abundance of CaO in the host rock of T2 increases with increasing MgO levels and resembles the MAB samples. This contrasts to T1, where the host rock is also enriched in CaO relative to MAB levels. Both transects, however, show even larger CaO enrichment within the CAZ. The abundance of Cr_2O_3 in T2 relative to the MAB shows greater variability than observed in T1. The host rock samples show similar levels to the MAB ranging from the lowest recorded MAB to above the highest recorded in MAB. The CAZ Cr_2O_3 show similar heterogeneity though tend to be of a similar level to the highest recorded Cr_2O_3 in the MAB.

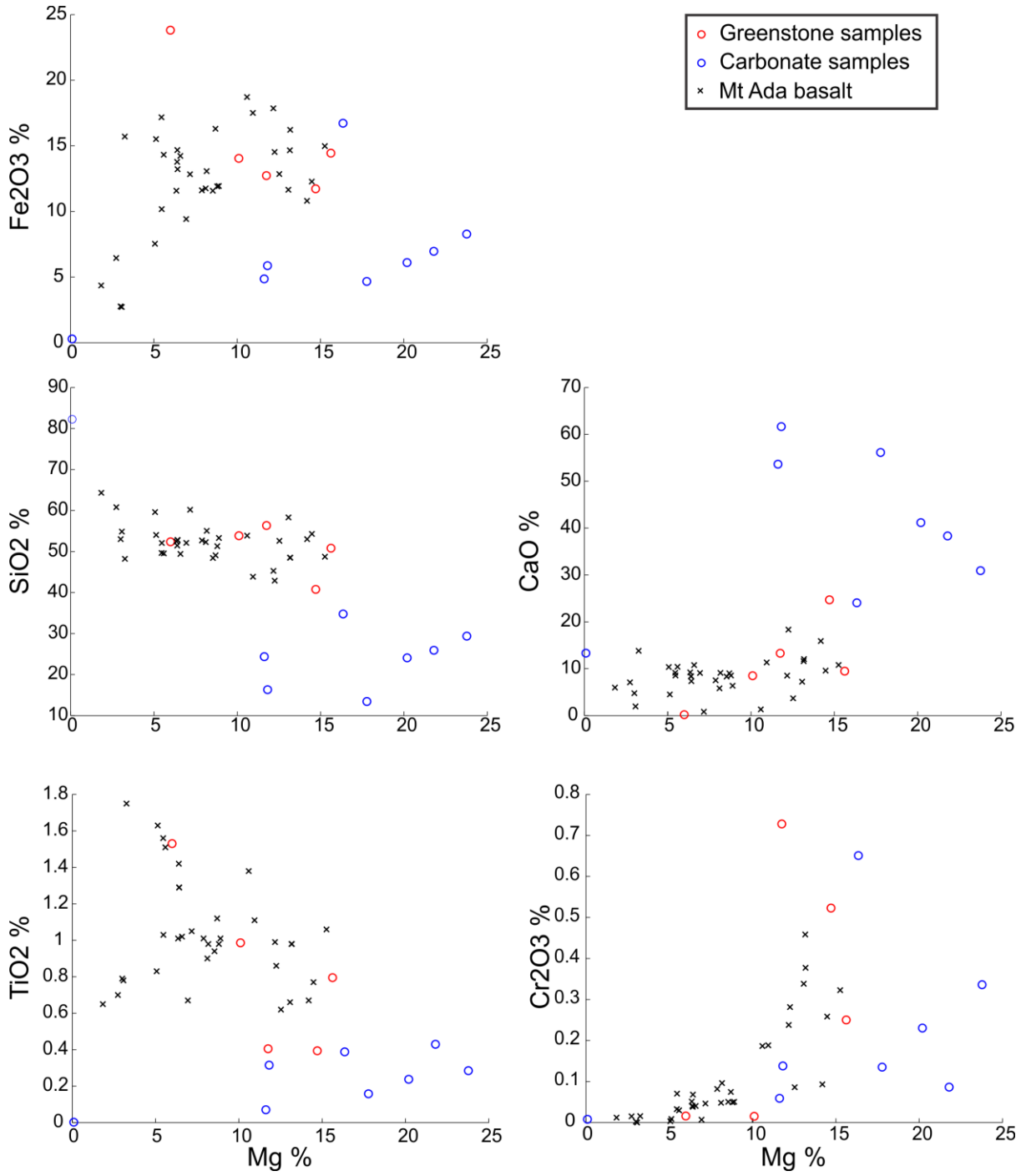

Figure 29 Harker diagrams of major elements plotted against MgO for Transect 1 with comparative chemistry of the Mt Ada basalt.

5.1.3 REE and trace element data

Trace and rare earth element (REE) data produced from LA-ICP-MS analysis was normalised to primitive mantle of McDonough and Sun 1995 and plotted as multi-element diagrams (Figures 30, 31). Two samples of a representative ultramafic lithology from the South Muccan Shear Zone are included (green lines). The grey shaded area represents the upper and lower bounds of the Komati komatiite from Barberton, South Africa (Puchtel et al., 2013). The multi element diagrams for both transects show scatter on the left hand side for the reactive elements such as Cs, Rb, Ba. These elements are highly mobile and as such, the scatter in the data is reasonable. Negative anomalies are pronounced for Cr and Ni in both transects. Co shows a subdued negative anomaly relative to the large anomaly of Cr and Ni. Both transects display a similar trend of positive anomalies for U, and Pb which are species that are relatively incompatible.

Spider diagrams of the REE (Figure 32) show a flat trend similar to modern tholeiitic basalts in both transects. T1 shows a minor negative Eu anomaly whereas in T2 the negative Eu anomaly is much more pronounced.

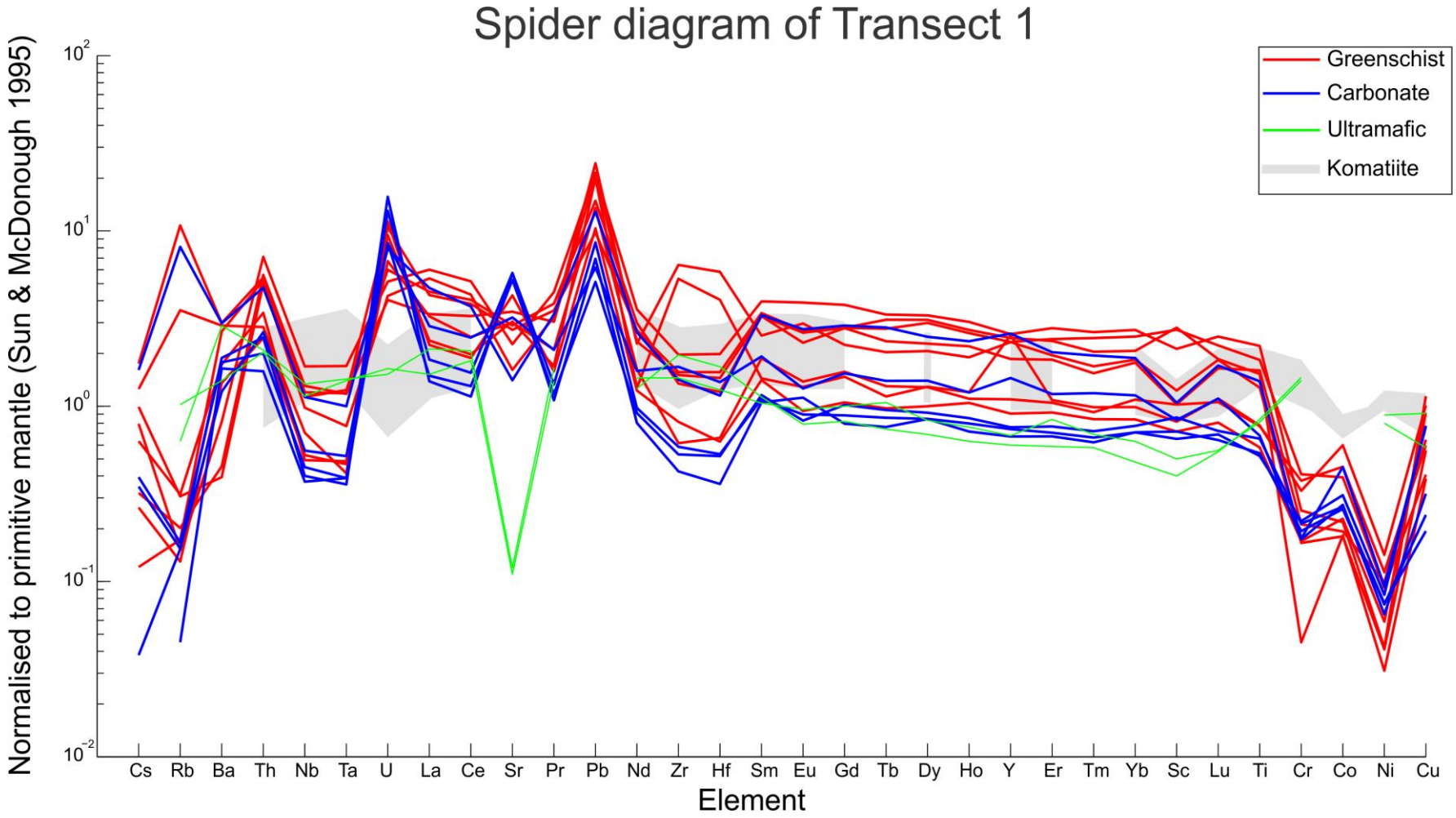

Figure 30 Transect 1 REE and trace elements plotted normalised against McDonough and Sun 1995. Grey background is Komati komatiite data from Barberton. See Appendix C for Doolena Gap data, see Puchtel et al. (2013) for komati data.

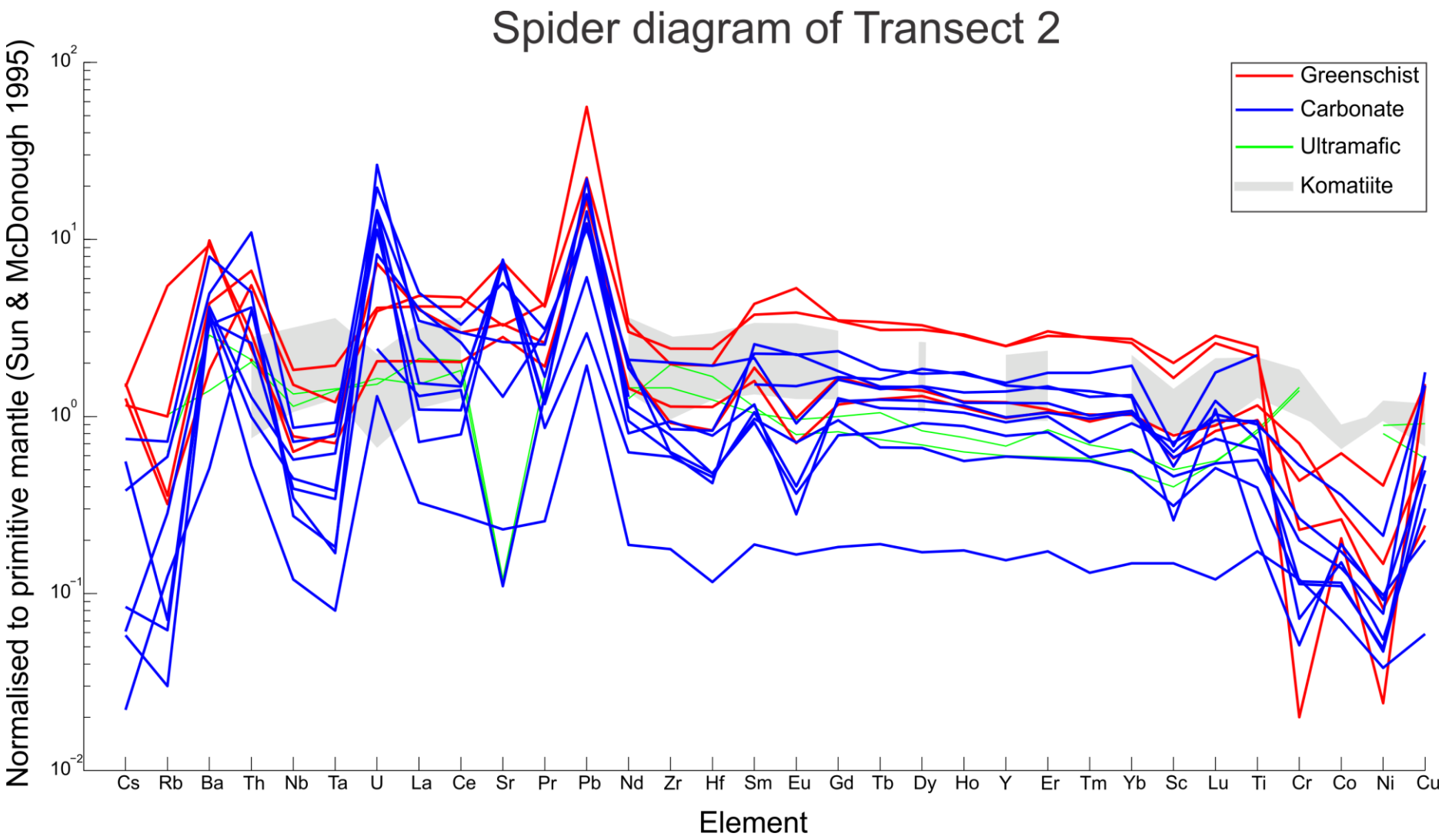

Figure 31 Transect 2 REE and trace elements plotted normalised against McDonough and Sun 1995. Grey background is Komati komatiite data from Barberton. See Appendix C for Doolena Gap data, see Puchtel et al. (2013) for komati data.

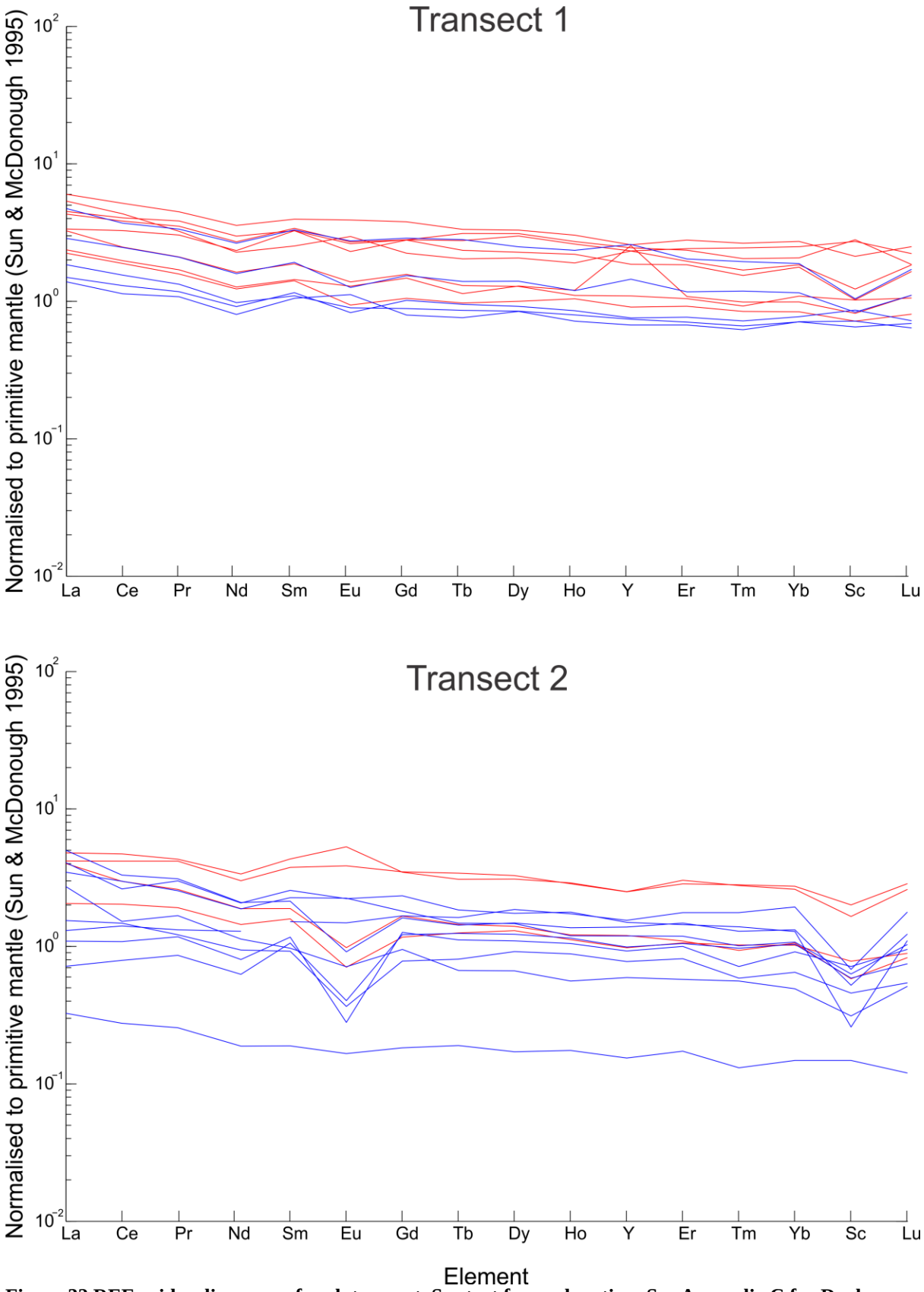

Figure 32 REE spider diagrams of each transect. See text for explanation. See Appendix C for Doolena Gap data.

5.2 Discussion

Geochemical analysis shows that there was a large addition of major species MgO, CO_2 and CaO to the transects along with the removal of SiO_2 (Figures 28, 29). The REE pattern (Figure 32) shows that the currently observed mineralogy of carbonate ± quartz ± chlorite is not primary in nature as the samples display trace element signatures that indicate a mafic protolith due to the flat REE pattern that is typical of modern tholeiitic basalts.

Plagioclase has a high partition coefficient for Eu so will readily take available Eu from a melt during crystallisation. If the melt and plagioclase are then separated, for example by fractionating plagioclase phencrysts or batch melting, there will be a negative Eu anomaly as the Eu had been taken up by the plagioclase. Interpreting the multi-element plots and REE spider diagrams, it is apparent based on the negative Eu anomaly that the source of the T2 samples experienced plagioclase removal.

The subdued negative Eu anomaly in T1 suggests that this was not the case, or much less pronounced than in the case of T2. Ni and Cr have a high partition coefficient for peridotite minerals such as olivine and pyroxene (and accessory magnetite) so the negative anomaly observed suggests that the source for the transect rocks experienced partial melting in equilibrium with these minerals that were left in the residuum. Observing the large negative anomaly of Ni, Cr for both transects and minor negative anomalies for Eu and Co relative to the pattern of the Komati data it is likely that the protolith for both transects was not komatiitic in nature as the patterns displayed in the multi-element plots do not match the Komati pattern.

5.2.1 Isocon analysis

In any system that has been metasomatically altered, there will be some trace and REE that remain immobile and some that are mobile (Grant, 1986, 2005; Mori et al., 2003; Polat

and Hofmann, 2003). The following isocon analysis of trace and REE data is presented to establish, which species are immobile during alteration and so can be used to examine potential protolith differences. The isocon analysis method followed is as described by Grant (1986). The method can be summarised as a way of determining the chemical changes of a system that has experienced mass transfer. Grant (1986) summarised work by Gresens (1967) relating the mass and concentration of chemical species in a system by the following: $C_i^A = M^O/M^A (C_i^O + \Delta C_i)$ where C_i is the concentration of a species, M is the mass and superscripts ^{O} and ^{A} relate to the original and altered value respectively. In an altered system for each species there will be an equation where M^O/M^A is a constant. The method relies on finding the immobile species for which $\Delta C_i = 0$ and plots these on a line termed the isocon, or a line of no chemical change. Critical to the method is identifying a sample that is representative of the least altered rock to plot the altered values against. Due to the extensive alteration only a best case sample is possible in this study to act as a comparison sample rather than an actual protolith. The closest approximation of fresh, unaltered rock in the transects based on field mapping, petrographic analysis and a low LOI value was sample 2-7. Sample 2-7 is from the southern end of Transect 2 composed of dominantly chlorite and quartz with minimal carbonate minerals and or veining. It had a LOI value of 15 %, the second lowest value recorded. In addition, isocon analysis was also performed for a relatively unaltered sample from Wiemer et al. (2016). This sample came from the northern end of the CFB and was representative of the mafic host Mt Ada basalt and displayed no signs of carbonate alteration. The isocons for both samples were essentially identical suggesting the illustrated choice of sample 2-7 as representative is justified.

Six representative samples which were chosen, three for each transect. These were to represent each bounding host rock and one for the CAZ in the centre. These were compared to sample 2-7 (Figure 33). Scaling factors were applied to all species for ease of visibility of

the graphical solution. Isocons were then determined by linear regression while controlling the intercept such that it intersected the origin. Following the method described by Grant (1986), there are sometimes multiple possible isocons that could be produced, however the method states that the most typically immobile elements such as Zr, Al_2O_3, and/or REEs are preferred if multiple solutions are possible. This study presents isocons plotted by linear regression rather than simultaneous solutions, as the method suggests, to better quantify the suitability of isocon as local heterogeneity results in some scatter of the data.

Polat and Hofmann (2003) have shown intense carbonate alteration can mobilise some typically immobile species which is the case in DGGB. As such, due to the extensive carbonate alteration there is expected scatter observed of typically immobile species.

For T1 samples 1-12, 1-8 and 1-7 show Ti and Al_2O_3 depletion. In T2 samples 2-1, 2-5 and 2-2 similarly show a depletion of Ti and Al_2O_3. Most REE in the transects plot close to the isocon as would be expected, however due to the scaling used in the method of Grant (1986) the low abudances of REE result in the REE data plotting near the origin where scatter is naturally minimised. Of the REE the most scatter is noted in values of Y. The major species Fe_2O_3, SiO_2 and MgO show strong variability in their relative depletion in all samples. CaO strongly varies in degree but is enriched in all samples which is consistent with the Harker diagram analysis comparing the transects values to the local Mt Ada basalt values.

This isocon analysis shows that there is major variability in the behaviour of the major elements Fe_2O_3, SiO_2 and MgO, and some variability in the trace elements such as Y and Ti, possibly arising from the heterogeneity in the samples and/or from the severe carbonate alteration. It is therefore inadvisable to consider these species for protolith comparison and characterisation. Generally, the isocon is defined by the REEs, Cr, and Al_2O_3. Therefore, the most appropriate species to consider are Cr and Al_2O_3 with Ti and the REE as secondary choice.

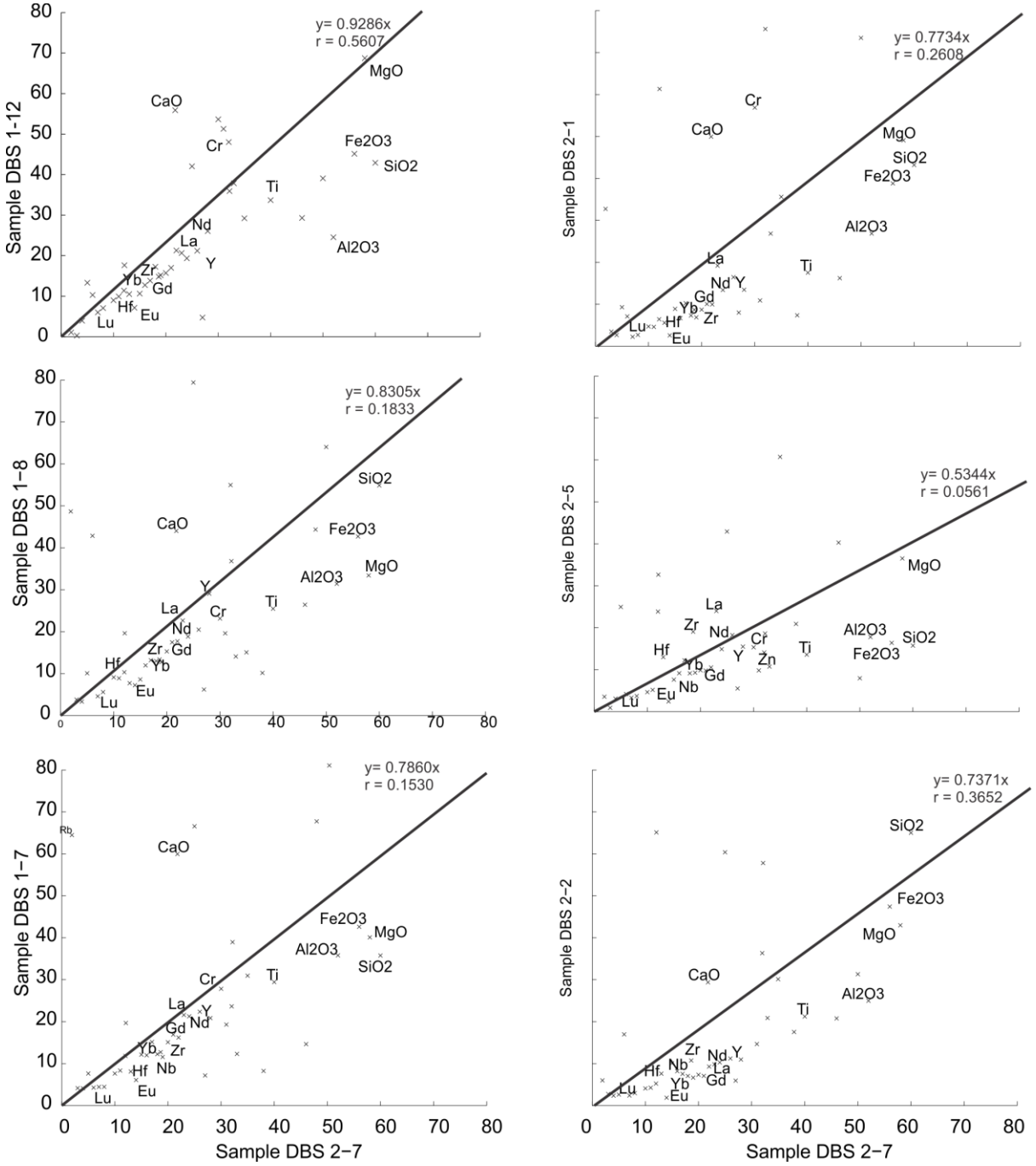

Figure 33: Isocon diagrams comparing samples to the least altered, protolith approximation sample 2-5. Plotted data is all trace and REE however labels were only attached to the most commonly used immobile species for clarity.

5.2.2 Discrimination analysis and diagrams

Local heterogeneities can produce different absolute concentrations of trace elements in the protolith. During metasomatic alteration these absolute concentrations will naturally change. Despite this natural variance in absolute concentrations of trace elements, the behaviour of species relative to one another will typically remain consistent (Smithies et al., 2005; White, 2013). Therefore, examining ratios of trace elements and REE can provide more useful information about the protolith than examining absolute concentrations.

Examining the ratios of Gd/Yb and Al_2O_3/TiO_2 and comparing the primitive mantle values (McDonough and Sun, 1995) can show if the source lithology is from a relatively evolved or primitive source as Yb and Al_2O_3 are more compatible than Gd and TiO_2 respectively (Smithies et al., 2005). Samples with values above the Gd/Yb and below the Al_2O_3/TiO_2 of primitive mantle would indicate that the protolith formed from a melt sourced from a primitive source. Both transects data for Gd/Yb and Al_2O_3/TiO_2 were compared to primitive mantle values and it was found that all samples had larger Gd/Yb relative to primitive mantle values (i.e. > 1.3) and all but one sample had lower Al_2O_3/TiO_2 values (i.e. < 20). Additionally the ratios for both host and CAZ rock cluster closely together. Therefore it can be determined that both host and CAZ samples were from a relatively primitive source and do not display any differences in these ratios which suggests a shared protolith.

Figure 34 compares values of the ratio of Al_2O_3/TiO_2 and Cr_2O_3 normalised to their respective maximum value across each transect as a function of distance. If the CAZ were protolith-controlled, one would expect a variance in these immobile species comparing host rock to CAZ. Such variability is not observed.

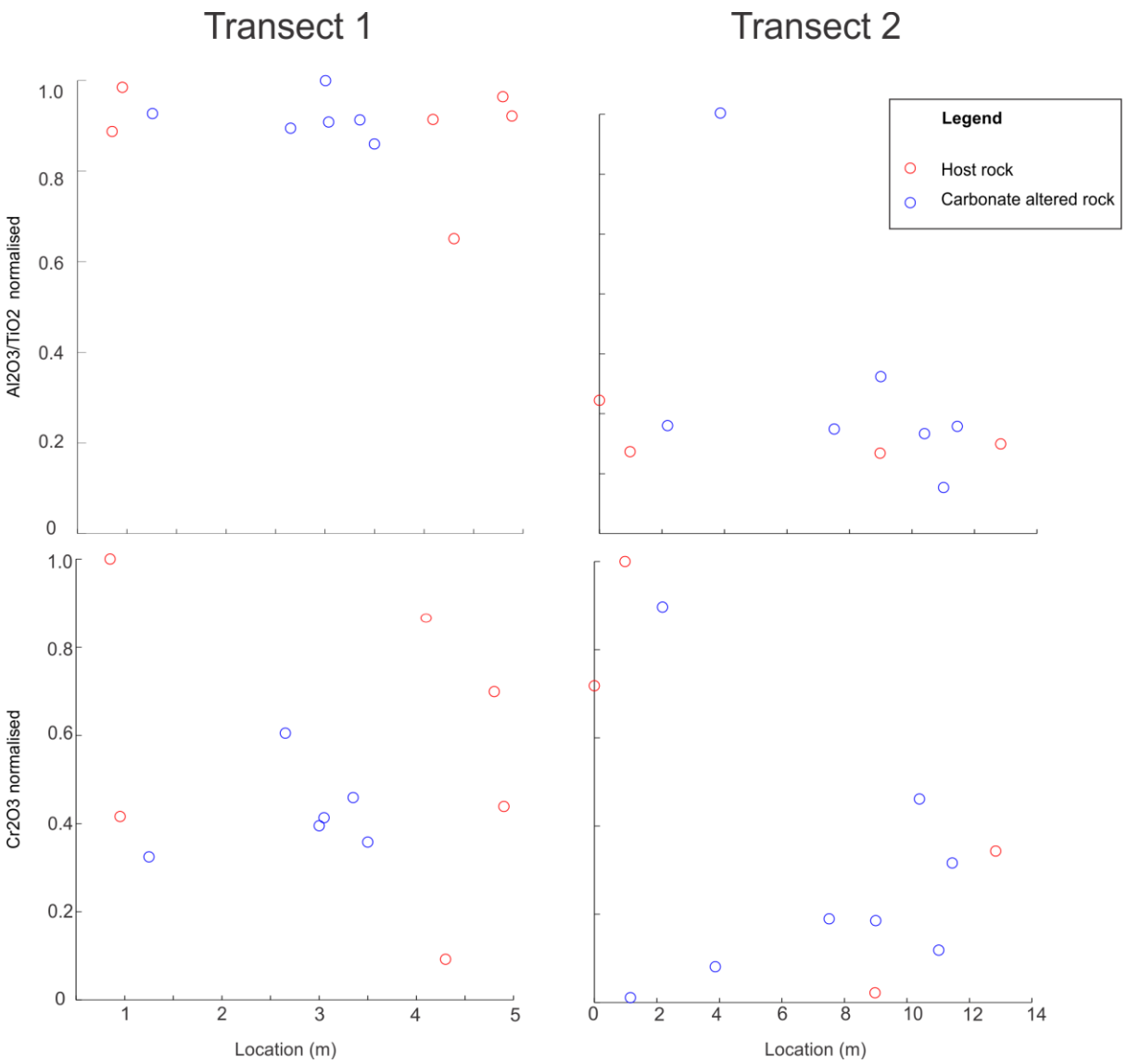

Figure 34 Discrimination geochemical diagram showing values for Al_2O_3/TiO_2 and Cr_2O_3 plotted against spatial distribution for both transects

5.2.3 Carbonate alteration source

A source explanation for the carbonate alteration is needed. As discussed in the literature review, likely sources could be primary carbonate from the pillow basalt interstices, mantle degassing, or exsolving fluids released during magma crystallisation. In the Low Strain Belt of DGGB, there is interstitial primary carbonate in the pillow basalts (Fig. 9). Since the interstices and vesicles of pillow basalt can make up to 40 % of it volumetrically (Wells et al., 1979), primary carbonate may be a significant source. This could be tested further with isotope analysis (Allwood et al., 2010; Kamber and Webb, 2001).

Ultramafic-mafic rock readily alters by serpentinisation or talc-carbonate alteration (see Chapter 2 for equation reaction). Examining the XRD results, it is clear that the CAZ are made up of dominantly quartz ± carbonates ± talc which are the expected products of talc-carbonate alteration of serpentinites. The serpentinisation of the original ultramafic-mafic rock can be facilitated by either:

[1] Hydration of exsolving fluids from the ascending Muccan dome, which originally sat below DGGB. It is reasonable to expect that hydrous fluids exsolved from this body during crystallisation. Such buoyant and hot fluids would have ascended into the overlying DGGB, thereby initiating fracturing and serpentinisation of the ultramafic-mafic rock.

[2] Sea water infiltrating into the greenstone. The presense of pillow basalts in the LSB indicate that sea water is a viable source of water for the proposed serpentinisation of the greenstone. The associated rapid cooling of the extruding basalt through sea water likely caused penetrative fracture systems in the upper oceanic crust through thermal-elastic stresses (Korenaga, 2007) which may have acted as conduits for sea water.

Mantle degassing of CO_2 could result in talc-carbonate alteration of the DGGB, consuming serpentine and producing talc + carbonates, the composition of which would depend on the available amounts of Ca, Mg, and Fe. Calcite, dolomite and ankerite are all in the system, with dolomite the largest carbonate component.

Therefore, there are ample potential sources for the initial carbonate alteration of the greenstone belt. Carbonate alteration during and post-dating the major D_2 event likely involves recycling and reworking of carbonate. Field and hand specimen observations show that the CAZ is dominantly carbonate that is foliated parallel to the S_2 foliation. This constitutes a volumetrically large source of locally available carbonate. If a dominantly carbonate body of rock is fractured and deformed, creating pathways for fluid, fluid

composition of the fluid will likely reflect local chemistry. Additionally, the S_2-foliated carbonate has experienced significant grain size reduction, increasing the available surface area, thus facilitating dissolution of carbonate minerals during fluid advection. Hence, the source of carbonate for the D_3 and D_4 related events are likely reworked older carbonate. In order to demonstrate the relative contribution of the sources, an investigation of isotopes and trace elements would be needed. Ratios of some trace elements and isotope data can be useful in determining the source of fluids (Allwood et al., 2010; Bolhar et al., 2005; Kamber and Webb, 2001). This isotope analysis is outside the scope of this study but would constitute a useful target for further study.

5.2.4 Protolith or shear-zone controlled alteration?

The geochemical analyses do not support the notion that the CAZ and their respective host rocks were derived from different protoliths. This is based on the following pieces of evidence:

[1] The multi-element and REE spider diagrams (Figures 30, 31, 32) show that the trace and REE patterns for both host and CAZ are parallel to sub-parallel, suggesting a similar source.

[2] The analysis of Gd/Yb to Al_2O_3/TiO_2 examined if the source of host rock and CAZ was primitive or evolved. No difference could be observed between host and CAZ. Additionally, the data for both host and CAZ samples clustered closely. If the CAZ and host rock derived from different protoliths, then the degree of evolution of the source and distinct groupings of the ratios would be expected. This was not observed.

[3] Examining the discrimination plot of immobile species plotted against spatial distribution (Figure 34) showed that there was no clear change of Cr_2O_3 or the ratio of Al_2O_3/TiO_2 across the transect. If the carbonate alteration was controlled by a difference in protolith, this data would be expected to show an abrupt change, coinciding with the contact

for the CAZ, as shown in the idealised transect behaviour (Figure 12). As there is no clear change it is unlikely that the carbonate alteration was controlled by a protolith difference.

These interpretations are subject to some ambiguities and shortcomings. The validity of the method for establishing isocons to determine the immobility of trace and REE has been questioned by some authors (Baumgartner and Olsen, 1995; Mukherjee and Gupta, 2008), especially when dealing with highly altered rocks. Importantly, the method requires a sample with the original rock composition. This is problematic in this study because the least altered sample of a former basalt has approximately 20 % carbonate minerals and a LOI of 15 %. It has been shown that carbonate alteration in particular can mobilise some trace elements (Polat and Hofmann, 2003). The heterogeneity of the typically immobile species (Zr, Ti, Hf, Al_2O_3, REE) throughout the transects also makes interpretation difficult.

The hypothesis that the CAZ were formed due to protolith controls can be rejected based on the evidence presented. However, this does not mean that the alternate hypothesis of strain localisation control can be accepted. Firstly, there were no displacement markers found in either transect to prove that the CAZ are actually shear zones. Quantifying strain from fabrics alone is difficult for the CAZ and the host rock. This is because both host rock and CAZ have experienced large degrees of heterogeneous non-coaxial finite strain, show large mineralogical and chemical heterogeneity on all scales, and D_2 was overprinted by three more deformation and metasomatic alteration events. Moreover, there is little to no experimental work on the rheology and microfabric of carbonates such as ankerite and siderite. Therefore, quantifying strain is very challenging. Additionally, the classic structural-geology assumption of space as a substitute for time cannot be used if one cannot even determine qualitatively the strain distribution in space. Nevertheless, the increase in foliation density in T1 may perhaps be the result of a local increase in strain. Yet this is quite a tentative speculation because, according to Rutter (1999), schists tend to have distributed strain and fabric intensity.

Therefore, the intensity of foliation is not a reliable marker of strain in these rocks. Because the host rocks and their CAZ examined display such texture, foliation density cannot be used as a reliable indicator of relative strain in these transects.

In other examples of shear zones in carbonates such as the Glarus thrust (Poulet et al., 2014), one can observe carbonate acting in an episodic manner, alternating between slow ductile and fast brittle slip events. This complex behaviour is explained by feedbacks. Poulet et a. (2014) show that ductile creep can cause shear heating, which in turn triggers endothermic carbonate breakdown reactions driving a fast slip period through chemical pressurisation. This is associated with a consumption of the excess shear heat, and the system returns to stable ductile creep. Thus, the shear zone continually oscillates between ductile and brittle rheology, and this can be seen in the mutual overprint of associated structures in the field. Poulet et al. (2014) state that this oscillating system behaviour can become a lot more complicated when one considers, for example, the release of additional hydrous phases through devolatisation from other minerals, reactive oxides like CaO and MgO forming hydroxides, infiltrating external fluids or high pressures resulting in hydraulic fracturing. The DGGB most likely experienced all these phenomena at some stage of its deformation history. Potential hydrous reactions due to exsolving fluids from the Muccan dome are likely. Complex reactions of major reactive oxides such as CaO, MgO and Fe_2O_3 would have been common because of their large abundance, and post-D_2 hydraulic fracturing is ubiquitous. Given the large strain of D_2, the preservation potential of episodic hydraulically induced D_2 brittle structures is low.

Finally, one could envisage that other differences in protolith properties, which are not compositional in nature, can explain localised metasomatism. The rock fabric can vary. For example, grain size distribution and vesicle contents in basalt flows are heterogeneously distributed (Wells et al., 1979). They in turn control the hydraulic conductivity of the rock

(Guéguen et al., 1996), which affects how fluids access and interact with the protolith. All of these initial features have been wiped out completely. Therefore, it seems difficult to test textural differences in protolith.

Chapter 6: Implications

I demonstrated conclusively that carbonate alteration is associated with all deformation phases documented in the CFB of the DGGB. The volumetrically most important contribution to the carbonate budget is made by the carbonates forming the penetrative regional S_2-foliation. While the formation of CAZ seems not to be controlled by host-rock composition, it was not possible with the methods employed here to demonstrate that they formed as a result of coupled strain localisation processes such as those proposed by Poulet et al. (2014). Nevertheless, it is an important finding that all D_2 fabrics contain large volumina of carbonate minerals. The host rocks feature 20% up to 50%, and the CAZ usually show an enrichment of up to 60% carbonate minerals. My microstructural observations imply that these carbonates formed during the early stages of D_2 or even prior to D_2. Given their large volumetric percentage and the observation that they are usually arranged in laterally extensive interconnected layers (rather than isolated inclusions), one can expect that they have a significant impact on the bulk rheology of the greenstone keel (Handy, 1994; Montési, 2013).

Carbonate minerals are known to be weak relative to the mineral assemblage of greenstones (Xu et al., 2009). Figure 35 shows a comparison of the strength profiles for carbonates (Solnfhofen limestone and Carrara marble) and quartz that illustrates, for a given temperature and grain size, it is expected that carbonates exhibit lower strength than quartz (Brodie and Rutter, 2000) under the greenschist-facies conditions expected for the DGGB: approximately 300-500°C temperature and grain sizes for the D_2 carbonate and quartz of ca. 5-100 μm. It is important, however, to keep limitations of this interpretation in mind. The experimental studies cited here are based on relatively clean calcite and limestone whereas the rocks in this study are certainly not clean carbonates. Studies on the rheological effect of

Mg concentration in carbonate highlight the potentially large impact of such ions (Kushnir et al., 2015; Xu et al., 2009). Moreover, pinning of grain boundaries by second phases has a major impact on rheology (Herwegh et al., 2003) and is expected to be common in the 'dirty' carbonates examined here. In addition, experimental studies typically focus on monomineralic compositions (Brodie and Rutter, 2000; Kushnir et al., 2015; Rutter, 1999). In the DGGB the mineral assemblages are polymineralic and have 'dirty' carbonates with a near solid solution observed from calcite to dolomite to ankerite in addition to quartz ± chlorite ± talc ± accessory oxides. Previous authors state that such polyphase assemblages have drastically different behaviour (Burlini and Bruhn, 2005; Rutter, 1999). Additionally, Dell'Angelo and Tullis (1996) have shown that just 15% of a weaker phase can result in strain weakening of the package of rock. Bestmann et al. (2000) show that, when examining carbonates that have compositions with both dolomite and calcite, strain weakening and localisation occur. Finally, the strain rates are extrapolated from laboratory conditions to geological strain rates, which may not be valid (Paterson, 2001). For these reasons, care needs to be taken when interpreting empirically derived strength profiles for carbonates and quartz to the geological scenario of the DGGB.

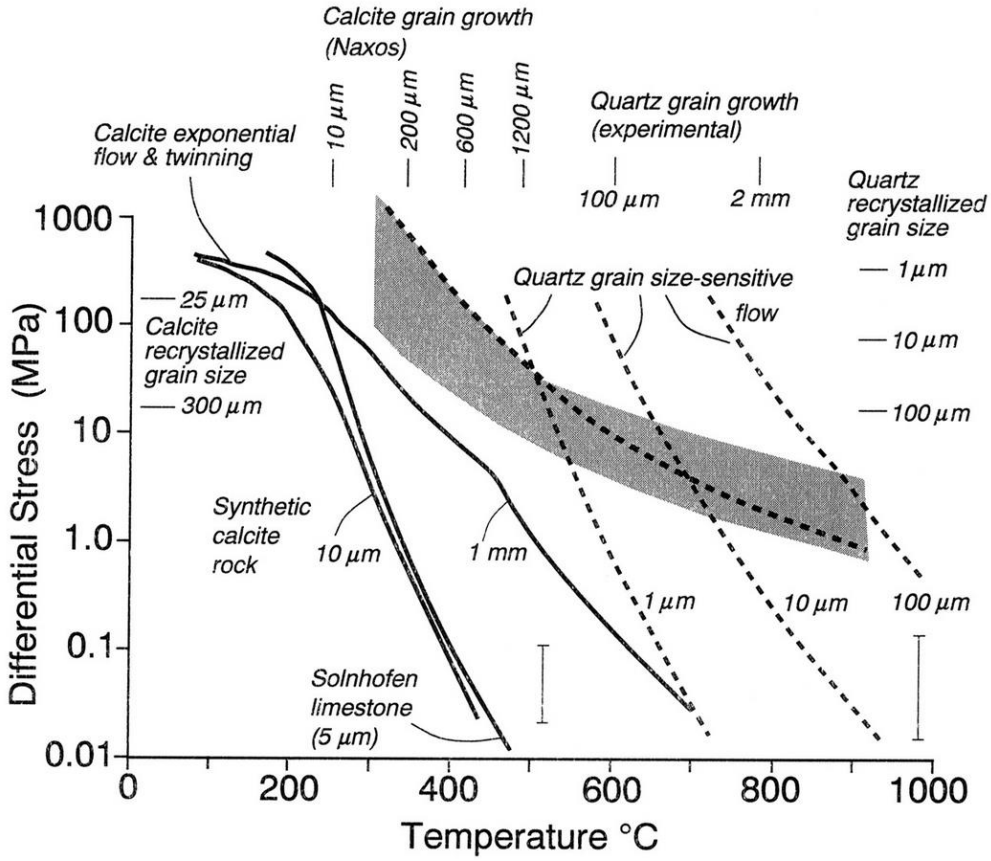

Figure 35 Comparison of the strength of carbonates (Solnhofen limestone and Carrara marble) to quartz. Quartz dashed lines indicate grain size sensitive flow and shaded area represents the upper and lower bounds from four quartz plastic flow experiments indicating that quartz deformation is by intracrystalline plastic processes; i) average wet quartzite ii) Black Hills quartzite iii) and iv) two hot pressed Brazilian quartz from the study cited. (Brodie and Rutter, 2000)

Keeping these caveats in mind, if we accept the notion that the carbonates were likely weaker than the quartz, it follows that carbonate alteration constitutes an important weakening mechanism for Archaean tectonics. The significant portion of carbonate in the host rock (up to 60% locally in this study) has likely played a large role in changing the rheology of the keel rock. It may be an important weakening mechanism postulated in some numerical studies (Collins et al., 1998; Thébaud and Rey, 2013).

Chapter 7: Conclusions

This study delivers the following conclusions:

[1] Carbonate alteration has occurred throughout the entire geological history of the greenstone belt of Doolena Gap associated with all deformation events.

[2] Carbonates associated with the S_2-foliation, which accommodated the main overturn event, constitute the most important volumetric proportion of carbonates in the CFB. They must have formed prior to or early on during D_2.

[3] Geochemical analyses suggest that CAZ are not a consequence of compositional variances in protolith.

[4] It remains unclear if CAZ formed through coupled strain localization processes or due to non-compositional protolith differences such as fabric and hydraulic conductivity.

[5] D_2 carbonates are volumetrically most significant in both host rocks and CAZ in the CFB. They form laterally extensive layers. Therefore, they likely affected the bulk rheology of the keel during the overturn event. If one accepts the tentative notion that carbonates are generally weaker under wet, greenschist-facies conditions than tectosilicates, it follows that carbonate alteration is a major weakening mechanism in greenstone belts.

Chapter 8: Bibliography

Allwood, A.C., Kamber, B.S., Walter, M.R., Burch, I.W., Kanik, I., 2010. Trace elements record depositional history of an Early Archean stromatolitic carbonate platform. Chemical Geology 270, 148-163.

Alt, J.C., Anderson, T.F., Bonnell, L., 1989. The geochemistry of sulfur in a 1.3 km section of hydrothermally altered oceanic crust, DSDP Hole 504B. Geochimica et Cosmochimica Acta 53, 1011-1023.

Andreani, M., Luquot, L., Gouze, P., Godard, M., Hoise, E., Gibert, B., 2009. Experimental study of carbon sequestration reactions controlled by the percolation of CO2-rich brine through peridotites. Environmental Science & Technology 43, 1226-1231.

Arndt, N., Teixeira, N., White, W., 1989. Bizarre geochemistry of komatiites from the Crixas greenstone belt, Brazil. Contributions to Mineralogy and Petrology 101, 187-197.

Bach, W., Paulick, H., Garrido, C.J., Ildefonse, B., Meurer, W.P., Humphris, S.E., 2006. Unraveling the sequence of serpentinization reactions: Petrography, mineral chemistry, and petrophysics of serpentinites from MAR 15°N (ODP Leg 209, Site 1274). Geophysical Research Letters 33.

Bagas, L., 2001-2002. Stratigraphic revision of the Warrawoona and Gorge Creek Groups in the Kelly greenstone belt, Pilbara Craton, Western Australia. Geological Survey or Western Australia.

Bailey, R., 1990. Trapping of aqueous fluids in the deep crust. Geophysical Research Letters 17, 1129-1132.

Baumgartner, L.P., Olsen, S.N., 1995. A least-squares approach to mass transport calculations using the isocon method. Economic Geology 90, 1261-1270.

Bestmann, M., Kunze, K., Matthews, A., 2000. Evolution of a calcite marble shear zone complex on Thassos Island, Greece: microstructural and textural fabrics and their kinematic significance. Journal of Structural Geology 22, 1789-1807.

Bjerga, A., Konopasek, J., Pedersen, R.B., 2015. Talc–carbonate alteration of ultramafic rocks within the Leka Ophiolite Complex, Central Norway. Lithos 227, 21-36.

Blatt, H., Tracy, R., Owens, B., 2006. Petrology: Igneous, sedimentary and metamorphic, 3 ed. WH Freeman, New York.

Bolhar, R., Van Kranendonk, M.J., Kamber, B.S., 2005. A trace element study of siderite–jasper banded iron formation in the 3.45 Ga Warrawoona Group, Pilbara Craton—formation from hydrothermal fluids and shallow seawater. Precambrian Research 137, 93-114.

Boulter, C.A., Bickle, M.J., Gibson, B., Wright, R.K., 1987. Horizontal tectonics pre-dating upper gorge creek group sedimentation pilbara block, western australia. Precambrian Research 36, 241-258.

Brace, W.F., Kohlstedt, D.L., 1980. Limits on lithospheric stress imposed by laboratory experiments. Journal of Geophysical Research: Solid Earth 85, 6248-6252.

Brodie, K., Rutter, E., 2000. Deformation mechanisms and rheology: why marble is weaker than quartzite. Journal of the Geological Society 157, 1093-1096.

Burgmann, R., Dresen, G., 2008. Rheology of the Lower Crust and Upper Mantle: Evidence from Rock Mechanics, Geodesy, and Field Observations. Annual Review of Earth and Planetary Sciences 36, 531-567.

Burkhard, M., 1993. Calcite twins, their geometry, appearance and significance as stress-strain markers and indicators of tectonic regime: a review. Journal of structural geology 15, 351-368.

Burlini, L., Bruhn, D., 2005. High-strain zones: Laboratory perspectives on strain softening during ductile deformation, Geological Society Special Publication, pp. 1-24.
Burov, E.B., 2011. Rheology and strength of the lithosphere. Marine and Petroleum Geology 28, 1402-1443.
Chardon, D., Choukroune, P., Jayananda, M., 1998. Sinking of the Dharwar basin (South India): implications for Archaean tectonics. Precambrian Research 91, 15-39.
Chen, S.F., Morris, P.A., Pirajno, F., 2005. Occurrence of komatiites in the Sandstone greenstone belt, north-central Yilgarn Craton. Australian Journal of Earth Sciences 52, 959-963.
Collins, W.J., 1989. Polydiapirism of the Archean Mount Edgar Batholith, Pilbara Block, Western Australia. Precambrian Research 43, 41-62.
Collins, W.J., Van Kranendonk, M.J., Teyssier, C., 1998. Partial convective overturn of Archaean crust in the east Pilbara Craton, Western Australia: driving mechanisms and tectonic implications. Journal of Structural Geology 20, 1405-1424.
Connolly, J.A.D., Podladchikov, Y.Y., 2004. Fluid flow in compressive tectonic settings: Implications for midcrustal seismic reflectors and downward fluid migration. J. Geophys. Res. 109.
Conrad, C.P., Molnar, P., 1997. The growth of Rayleigh-Taylor-type instabilities in the lithosphere for various rheological and density structures. Geophysical Journal International 129, 95-112.
de Bremond d'Ars, J., Lécuyer, C., Reynard, B., 1999. Hydrothermalism and diapirism in the Archean: gravitational instability constraints. Tectonophysics 304, 29-39.
Dell'Angelo, L.N., Tullis, J., 1996. Textural and mechanical evolution with progressive strain in experimentally deformed aplite. Tectonophysics 256, 57-82.
Dimanov, A., Raphanel, J., Dresen, G., 2011. Newtonian flow of heterogeneous synthetic gabbros at high strain: Grain sliding, ductile failure, and contrasting local mechanisms and interactions. European Journal of Mineralogy 23, 303-322.
Dimroth, E., Cousineau, P., Leduc, M., Sanschagrin, Y., 1978. Structure and organization of Archean subaqueous basalt flows, Rouyn-Noranda area, Quebec, Canada. Canadian Journal of Earth Sciences 15, 902-918.
Drazin, P.G., Reid, W.H., 1981. Hydrodynamic stability. Cambridge University Press.
Ferrill, D.A., 1991. Calcite twin widths and intensities as metamorphic indicators in natural low-temperature deformation of limestone. Journal of Structural Geology 13, 667-675.
Ferrill, D.A., Morris, A.P., Evans, M.A., Burkhard, M., Groshong Jr, R.H., Onasch, C.M., 2004. Calcite twin morphology: A low-temperature deformation geothermometer. Journal of Structural Geology 26, 1521-1529.
Ferry, J.M., Gerdes, M.L., 1998. Chemically reactive fluid flow during metamorphism. Annual Review of Earth and Planetary Sciences 26, 255-287.
Fusseis, F., Handy, M.R., Schrank, C., 2006. Networking of shear zones at the brittle-to-viscous transition (Cap de Creus, NE Spain). Journal of Structural Geology 28, 1228-1243.
Fusseis, F., Regenauer-Lieb, K., Liu, J., Hough, R.M., De Carlo, F., 2009. Creep cavitation can establish a dynamic granular fluid pump in ductile shear zones. Nature 459, 974-977.
Gogus, O.H., Pysklywec, R.N., 2008. Near-surface diagnostics of dripping or delaminating lithosphere. Journal of Geophysical Research 113, B11404.
Goldfarb, R., Groves, D., Gardoll, S., 2001. Orogenic gold and geologic time: a global synthesis. Ore geology reviews 18, 1-75.
Grant, J.A., 1986. The isocon diagram; a simple solution to Gresens' equation for metasomatic alteration. Economic Geology 81, 1976-1982.
Grant, J.A., 2005. Isocon analysis: A brief review of the method and applications. Physics and Chemistry of the Earth, Parts A/B/C 30, 997-1004.

Green, M.G., Sylvester, P.J., Buick, R., 2000. Growth and recycling of early Archaean continental crust: geochemical evidence from the Coonterunah and Warrawoona Groups, Pilbara Craton, Australia. Tectonophysics 322, 69-88.
Guéguen, Y., Gavrilenko, P., Le Ravalec, M., 1996. Scales of rock permeability. Surveys in Geophysics 17, 245-263.
Handy, M.R., 1994. Flow laws for rocks containing two non-linear viscous phases: a phenomenological approach. Journal of Structural Geology 16, 287-301.
Harlov, D.E., Austrheim, H., 2013. Metasomatism and the Chemical Transformation of Rock. Springer Berling Heidelberg, Berlin.
Herwegh, M., Xiao, X., Evans, B., 2003. The effect of dissolved magnesium on diffusion creep in calcite. Earth and Planetary Science Letters 212, 457-470.
Hickman, A.H. (2004), Two contrasting granite-greenstone terranes in the Pilbara craton, Australia: evidence for vertical and horizontal tectonic regimes prior to 2900 Ma, Precambrian Research 131, 153-172.
Hickman, A.H., 2012. Review of the Pilbara Craton and Fortescue Basin, Western Australia: Crustal evolution providing environments for early life. Island Arc 21, 1-31.
Hippertt, J., Davis, B., 2000. Dome emplacement and formation of kilometre-scale synclines in a granite–greenstone terrain (Quadrila´tero Ferrı´fero, southeastern Brazil). Precambrian Research 102, 99-121.
Kamber, B.S., Webb, G.E., 2001. The geochemistry of late Archaean microbial carbonate: implications for ocean chemistry and continental erosion history. Geochimica et Cosmochimica Acta 65, 2509-2525.
Kamenetsky, V.S., Kamenetsky, M.B., 2010. Magmatic fluids immiscible with silicate melts: Examples from inclusions in phenocrysts and glasses, and implications for magma evolution and metal transport. Geofluids 10, 293-311.
Kelemen, P.B., Matter, J., 2008. In situ carbonation of peridotite for CO2 storage. Proceedings of the National Academy of Sciences 105, 17295-17300.
Kemp, A.I.S., Hawkesworth, C.J., Paterson, B.A., Kinny, P.D., 2006. Episodic growth of the Gondwana supercontinent from hafnium and oxygen isotopes in zircon. Nature 439, 580-583.
Klein, F., Garrido, C.J., 2011. Thermodynamic constraints on mineral carbonation of serpentinized peridotite. Lithos 126, 147-160.
Kloppenburg, A., White, S. H., Zegers, T. E., 2001. Structural evolution of the Warrawoona Greenstone Belt and adjoining granitoid complexes, Pilbara Craton, Australia: Implications for archaean tectonic processes. Precambrian Research 112, 107-147.
Korenaga, J., 2007. Thermal cracking and the deep hydration of oceanic lithosphere: a key to the generation of plate tectonics? Journal of Geophysical Research: Solid Earth 112.
Kull, H.J., 1991. Theory of the Rayleigh-Taylor instability. Physics Reports 206, 197-325.
Kushnir, A.R., Kennedy, L., Misra, S., Benson, P., White, J., 2015. The mechanical and microstructural behaviour of calcite-dolomite composites: An experimental investigation. Journal of Structural Geology 70, 200-216.
Lahaye, Y., Arndt, N., Byerly, G., Chauvel, C., Fourcade, S., Gruau, G., 1995. The influence of alteration on the trace-element and Nd isotopic compositions of komatiites. Chemical Geology 126, 43-64.
Lee, C.T.A., 2006. Geochemical/petrologic constraints on the origin of cratonic mantle. Archean geodynamics and environments, 89-114.
Lin, S., 2005. Synchronous vertical and horizontal tectonism in the Neoarchean: Kinematic evidence from a synclinal keel in the northwestern Superior craton, Canada. Precambrian Research 139, 181-194.

Lowe, D.R., 1983. Restricted shallow-water sedimentation of Early Archean stromatolitic and evaporitic strata of the Strelley Pool Chert, Pilbara Block, Western Australia. Precambrian Research 19, 239-283.
Marshak, S., 1999. Deformation style way back when: thoughts on the contrasts between Archean/Paleoproterozoic and contemporary orogens. Journal of Structural Geology 21, 1175-1182.
Marshak, S., Alkmim, F., Jordt-Evangelista, H., 1992. Proterozoic crustal extension and the generation of dome-and-keel structure in an Archaean granite-greenstone terrane. Nature 357, 491-493.
Marshak, S., Tinkham, D., Alkmim, F., Brueckner, H., Bornhorst, T., 1997. Dome-and-keel provinces formed during Paleoproterozoic orogenic collapse-core complexes, diapirs, or neither?: Examples from the Quadrilátero Ferrífero and the Penokean orogen. Geology 25, 415-418.
McDonough, W.F., Sun, S.s., 1995. The composition of the Earth. Chemical Geology 120, 223-253.
Montési, L.G., 2013. Fabric development as the key for forming ductile shear zones and enabling plate tectonics. Journal of Structural Geology 50, 254-266.
Mori, Y., Nishiyama, T., Yanagi, T., 2003. Mass transfer and reaction paths in alteration zones around carbonate veins in the Nishisonogi metamorphic rocks, southwest Japan. American Mineralogist 88, 611-623.
Mukherjee, P., Gupta, P., 2008. Arbitrary scaling in ISOCON method of geochemical mass balance: An evaluation of the graphical approach. Geochemical Journal 42, 247-253.
Murphy, J.B., Hynes, A.J., 1986. Contrasting secondary mobility of Ti, P, Zr, Nb, and Y in two metabasaltic suites in the Appalachians. Canadian Journal of Earth Sciences 23, 1138-1144.
Nijman, W., Willigers, B.J.A., Krikke, A., 1999. Tensile and compressive growth structures: relationships between sedimentation, deformation and granite intrusion in the Archaean Coppin Gap greenstone belt, Eastern Pilbara, Western Australia. Precambrian Research 95, 277-302.
O'Neill, C., Debaille, V., 2014. The evolution of Hadean–Eoarchaean geodynamics. Earth and Planetary Science Letters 406, 49-58.
Ordóñez-Calderón, J. C., Polat, A., Fryer, B. J., Gagnon, J. E., Raith, J. G., Appel, P. W. U., 2008. Evidence for HFSE and REE mobility during calc-silicate metasomatism, Mesoarchean (∼3075 Ma) Ivisaartoq greenstone belt, southern West Greenland. Precambrian Research 161, 317-340.
Passchier, C.W., Trouw, R.A.J., 2005. Microtectonics. Springer.
Paterson, M., 2001. Relating experimental and geological rheology. International Journal of Earth Sciences 90, 157-167.
Polat, A., Hofmann, A.W., 2003. Alteration and geochemical patterns in the 3.7–3.8 Ga Isua greenstone belt, West Greenland. Precambrian Research 126, 197-218.
Polat, A., Longstaffe, F., Weisener, C., Fryer, B., Frei, R., Kerrich, R., 2012. Extreme element mobility during transformation of Neoarchean (ca. 2.7Ga) pillow basalts to a Paleoproterozoic (ca. 1.9Ga) paleosol, Schreiber Beach, Ontario, Canada. Chemical Geology 326-327, 145-173.
Poulet, T., Veveakis, M., Herwegh, M., Buckingham, T., Regenauer-Lieb, K., 2014. Modeling episodic fluid-release events in the ductile carbonates of the Glarus thrust. Geophysical Research Letters 41, 7121-7128.
Puchtel, I.S., Blichert-Toft, J., Touboul, M., Walker, R.J., Byerly, G.R., Nisbet, E.G., Anhaeusser, C.R., 2013. Insights into early Earth from Barberton komatiites: Evidence from

lithophile isotope and trace element systematics. Geochimica et Cosmochimica Acta 108, 63-90.
Putnis, A., Austrheim, H., 2010. Fluid- induced processes: metasomatism and metamorphism. Geofluids 10, 254-269.
Pysklywec, R.N., Cruden, A.R. 2004. Coupled crust-mantle dynamics and intraplate tectonics: Two-dimensional numerical and three-dimensional analogue modeling Geochemistry, Geophysics, Geosystems 5, 10.
Rakovan, J., 2005. Pillow Basalt. Rocks and Minerals 80.
Rayment, G.E., Lyons, D.J., 2011. Soil chemical methods: Australasia. CSIRO Publishing, Collingwood, Vic.
Regenauer-Lieb, K., Petit, J.P., Yuen, D., 1999. Quasi-adiabatic shear zones in the lithosphere: Numerical and experimental approaches. Electronic Geosciences 4.
Regenauer-Lieb, K., Yuen, D.A., 2003. Modeling shear zones in geological and planetary sciences: Solid- and fluid-thermal-mechanical approaches. Earth-Science Reviews 63, 295-349.
Rey, P.F., Philippot, P., Thébaud, N., 2003. Contribution of mantle plumes, crustal thickening and greenstone blanketing to the 2.75-2.65 Ga global crisis. Precambrian Research 127, 43-60.
Robin, C.M.I., Bailey, R.C., 2009. Simultaneous generation of Archean crust and subcratonic roots by vertical tectonics. Geology 37, 523-526.
Rumble, D., 1994. Water circulation in metamorphism. Journal of Geophysical Research: Solid Earth 99, 15499-15502.
Rushmer, T., Jackson, M., 2006. Impact of melt segregation on tonalite–trondhjemite–granodiorite (TTG) petrogenesis. Earth and Environmental Science Transactions of the Royal Society of Edinburgh 97, 325-336.
Rutter, E.H., 1999. On the relationship between the formation of shear zones and the form of the flow law for rocks undergoing dynamic recrystallization. Tectonophysics 303, 147-158.
Schneider, C.A., Rasband, W.S., Eliceiri, K.W., 2012. NIH Image to ImageJ: 25 years of image analysis. Nat methods 9, 671-675.
Smithies, R.H., Champion, D., Van Kranendonk, M.J., Hickman, A., 2007. Geochemistry of volcanic rocks of the Northern Pilbara craton, Western Australia, in: Resources, D.o.I.a. (Ed.). Geological Survey of Western Australia, Perth, p. 53.
Smithies, R.H., Champion, D.C., Van Kranendonk, M.J., 2009. Formation of Paleoarchean continental crust through infracrustal melting of enriched basalt. Earth and Planetary Science Letters 281, 298-306.
Smithies, R.H., Van Kranendonk, M.J., Champion, D.C., 2005. It started with a plume - Early Archaean basaltic proto-continental crust. Earth and Planetary Science Letters 238, 284-297.
Stipp, M., Stünitz, H., Heilbronner, R., Schmid, S.M., 2002. The eastern Tonale fault zone: a 'natural laboratory' for crystal plastic deformation of quartz over a temperature range from 250 to 700 °C. Journal of Structural Geology 24, 1861-1884.
Sulem, J., Famin, V., 2009. Thermal decomposition of carbonates in fault zones: Slip-weakening and temperature-limiting effects. Journal of Geophysical Research: Solid Earth 114.
Thébaud, N., Rey, P.F., 2013. Archean gravity-driven tectonics on hot and flooded continents: Controls on long-lived mineralised hydrothermal systems away from continental margins. Precambrian Research 229, 93-104.
Tucker, M.E., Wright, V.P., 1990. Carbonate Sedimentology. Blackwell Science, Victoria, Australia, p. 482.
Van Kranendonk, M.J., 2004. Preface: Archaean Tectonics 2004: A review. Precambrian Research 131, 143-151.

Van Kranendonk, M.J., 2006. Volcanic degassing, hydrothermal circulation and the flourishing of early life on Earth: A review of the evidence from c. 3490-3240 Ma rocks of the Pilbara Supergroup, Pilbara Craton, Western Australia. Earth-Science Reviews 74, 197-240.
Van Kranendonk, M.J., 2010. Geology of the Coongan 1:100,000 sheet. Geological Survey of Western Australia 1:100,000 Geological Series Explanatory Notes, 67.
Van Kranendonk, M.J., Collins, W.J., Hickman, A., Pawley, M.J., 2004. Critical tests of vertical vs. horizontal tectonic models for the Archaean East Pilbara granite–greenstone terrane, Pilbara Craton, Western Australia. Precambrian Research 131, 173-211.
Van Kranendonk, M.J., Webb, G.E., Kamber, B.S., 2003. Geological and trace element evidence for a marine sedimentary environment of deposition and biogenicity of 3.45 Ga stromatolitic carbonates in the Pilbara Craton, and support for a reducing Archaean ocean. Geobiology 1, 91-108.
Wells, G., Bryan, W.B., Pearce, T.H., 1979. Comparative morphology of ancient and modern pillow lavas. The Journal of Geology, 427-440.
White, W.M., 2013. Geochemistry, 1 ed. Wiley, Somerset.
Wiemer, D., Schrank, C., Murphy, D., Hickman, A., 2016. Lithostratigraphy and structure of the early Archaean Doolena Gap greenstone belt: implications for dome-and-keel development in the East Pilbara Terrane, Western Australia.
Wingate, M.T.D., 1999. Ion microprobe baddeleyite and zircon ages for Late Archaean mafic dykes of the Pilbara Craton, Western Australia. Australian Journal of Earth Sciences 46, 493-500.
Winter, J.D., 2010. An introduction to igneous and metamorphic petrology. Prentice Hall, Upper Saddle River, N.J.
Xu, L., Renner, J., Herwegh, M., Evans, B., 2009. The effect of dissolved magnesium on creep of calcite II: Transition from diffusion creep to dislocation creep. Contributions to Mineralogy and Petrology 157, 339-358.
Yardley, B.W.D., 2013. The Chemical Composition of Metasomatic Fluids in the Crust, Metasomatism and the Chemical Transformation of Rock: The Role of Fluids in Terrestrial and Extraterrestrial Processes. Springer Berlin Heidelberg, Berlin, Heidelberg, pp. 17-51.
Zegers, T.E., Barley, M.E., Groves, D.I., McNaughton, N.J., White, S.H., 2002. Oldest gold: Deformation and hydrothermal alteration in the early Archaen shear zone-hosted Bamboo Creek deposit, Pilbara, Western Australia. Economic Geology 97, 757-773.
Zharikov, V.A., Pertsev, N.N., Rusinov, V.L., Callegari, E., Fettes, D.J., 2007. Metasomatism and metasomtic rocks. IUGS Subcommision on the Systematics of Metamorphic Rocks.
Zibra, I., Gessner, K., Smithies, H.R., Peternell, M., 2014. On shearing, magmatism and regional deformation in Neoarchean granite-greenstone systems: Insights from the Yilgarn Craton. Journal of Structural Geology 67, Part B, 253-267.

Chapter 9: Appendices

Appendix A: XRD data

All minerals listed are in modal % of the total mineralogy except for the quartz/carbonate ratio which is unitless.

Sample	Location (m)	r weight percent	Non diffracting	Quartz	Carbonates	Chlorites	Talc	Goethite	Hematite	Oxides	Qtz/Crb
1-01	0.95	6.916	29.63	29.92	21.39	18.05	0	0	0	1.01	1.40
1-03	2.65	8.795	15.56	12.78	45.56	10.26	7.29	7.46	0	1.09	0.28
1-06	4.1	5.430	8.41	23.22	55.56	7.08	0	5.26	0	0.47	0.42
1-07	4.9	7.578	9.81	18.59	60.3	10.88	0	0	0	0.43	0.31
1-10	3.35	7.960	9.05	2.29	58.75	16.35	7.85	5.22	0	0.49	0.04
1-11	4.3	7.559	26.63	30.5	31.34	9.84	0	0	0.59	1.1	0.97
1-12	0.85	7.441	16.65	26.06	36.45	15.41	1.52	3.26	0	0.65	0.71
1-13	1.25	6.705	7.75	17.77	57.53	7.53	5	4.41	0	0	0.31
1-14	3.05	8.239	15.35	5.48	59.17	6.21	7.54	6.26	0	0	0.09
1-15	3	7.011	10.81	10.93	58.33	7.42	6.06	6.45	0	0	0.19
1-16	4.8	5.748	9.46	26.34	50.05	8.04	0	4.05	2.06	0	0.53
2-01	0	5.871	17.79	23.63	50.56	8.03	0	0	0	0	0.47
2-02	0.98	5.790	10.79	40.58	32.35	11.43	0	0	1.72	3.12	1.25
2-03	1.15	6.686	14.44	4.07	56.5	12.13	5.75	2.88	3.23	1	0.07
2-04	3.87	13.101	24.02	1.89	57.47	5.77	9.3	1.55	0	0	0.03
2-05	7.51	6.652	20.65	1.61	64.27	7.42	5.08	0	0.98	0	0.03
2-06	10.4	9.160	15.25	6.58	57.93	8.67	10.49	0	1.09	0	0.11
2-07	12.84	9.057	32.89	21.92	19.56	17.31	6.79	0	0	1.52	1.12
2-08c	9	8.346	10.78	1.26	77.55	4.72	3.43	2.26	0	0	0.02
2-09	2.18	5.260	35.38	16.04	35.84	5.4	1.06	5.74	0	0.54	0.45
2-11	11.02	8.418	12.14	7.44	63.14	9.33	7.42	0	0	0.53	0.12
2-23	8.49	8.194	13.4	7.45	66.25	6.31	6.6	0	0	0	0.11

Appendix B: WDS XRF table

		PbO	HfO2	CuO	NiO	Fe2O3	Cr2O3	BaO	TiO2	CaO	K2O	SO3	ZrO2	P2O5	SrO	SiO2	Al2O3	MgO	Na2O
Sample	Result	wt (%)	wt (%)	wt (%)	wt (%)	wt (%)	wt (%)	wt (%)	wt (%)	wt (%)	wt (%)	wt (%)	wt (%)	wt (%)	wt (%)	wt (%)	wt (%)	wt (%)	wt (%)
1-1		0.007	0.001	0.008	0.044	14.345	0.253	0.01	0.699	9.87	0.021	0.036	0.002	0.336	0.003	53.363	6.562	12.711	0.006
1-1	LLD (ppm)	18.595	33.879	9.606	10.579	18.541	18.368	41.902	21.278	24.865	15.568	19.554	36.64	28.603	44.293	50.769	34.356	45.205	42.678
1-3		0.005	-0.002	0.001	0.051	12.935	0.366	0.006	0.604	18.309	0.004	0.023	0	0.038	0	46.917	5.163	11.363	-0.003
1-3	LLD (ppm)	30.116	54.713	15.13	16.116	30.213	30.215	70.457	36.457	43.745	26.775	33.375	59.687	49.35	60.788	74.08	47.82	65.497	65.337
1-6		0.006	0	0.015	0.108	15.686	0.525	0.012	0.429	34.65	0.147	0.035	-0.001	0.05	0.006	33.486	3.73	9.204	0.114
1-6	LLD (ppm)	32.228	58.039	16.237	17.263	31.886	32.23	74.472	38.215	49.018	27.858	32.555	59.324	49.644	53.011	68.733	44.504	62.787	64.081
1-7		0.007	-0.002	0.008	0.075	13.28	0.266	0.012	0.691	30.421	1.275	0.017	-0.001	0.06	0.006	34.302	6.064	12.078	0.027
1-7	LLD (ppm)	20.458	36.748	10.577	11.759	20.185	20.346	46.333	23.628	31.699	17.064	18.845	34.234	27.723	37.973	44.285	32.7	43.994	42.977
1-8		0.008	-0.001	0.009	0.07	12.096	0.217	0.006	0.608	20.93	1.003	0.048	0.001	0.052	0	49.335	4.989	9.485	0.031
1-8	LLD (ppm)	19.412	34.875	10.094	10.881	19.318	19.006	44.391	22.423	28.637	16.576	18.86	34.534	28.145	42.941	48.694	32.478	42.249	40.329
1-10		0.006	0.001	0.002	0.06	12.323	0.278	0.009	0.229	39.996	0.017	0.034	-0.002	0.067	0.018	22.409	2	18.024	0.004
1-10	LLD (ppm)	20.613	36.943	10.761	11.829	20.507	20.537	47.532	24.177	33.72	16.221	18.147	32.408	27.976	31.918	39.23	24.886	44.244	46.559
1-10		0.005	0	0.003	0.062	12.339	0.275	0.004	0.228	39.959	0.016	0.034	-0.001	0.063	0.018	22.429	2.023	18.053	0.003
1-10	LLD (ppm)	20.714	36.901	10.673	11.738	20.551	20.64	47.983	24.553	33.77	16.299	17.956	32.197	28.031	32.19	39.333	24.986	44.263	46.62
1-10		0.008	0.001	0.003	0.064	12.622	0.278	0.007	0.237	40.537	0.018	0.033	-0.002	0.064	0.019	22.611	2.024	18.079	0.003
1-10	LLD (ppm)	20.873	37.718	10.808	12.09	21.103	21.213	48.676	24.908	34.383	16.389	18.488	32.942	27.667	31.936	39.797	25.657	44.499	46.876
1-10		0.009	0.002	0.003	0.066	12.614	0.282	0.006	0.232	40.4	0.017	0.035	0	0.068	0.021	22.485	2.018	18.076	0.001
1-10	LLD (ppm)	20.888	37.826	10.706	11.744	21.032	21.131	48.667	24.886	34.233	16.387	18.406	32.509	27.998	32.079	39.858	25.257	44.366	47.044
1-11		0.008	0.002	0.002	0.021	10.352	0.056	0.004	0.759	15.16	0.007	0.018	-0.002	0.053	0.007	53.869	4.718	14.068	-0.007
1-11	LLD (ppm)	18.466	33.378	9.51	10.49	18.446	18.289	42.675	21.617	26.808	15.427	19.062	35.587	30.419	44.105	50.739	32.523	44.986	43.569
1-12		0.0085	0.0005	0.0050	0.0690	13.853	0.3031	0.0070	0.4336	26.001	0.0175	0.0470	0.0070	0.1295	0.0070	36.098	3.6623	17.875	0.0075
1-12	LLD (ppm)	39.433	71.415	20.391	22.747	39.206	38.511	89.883	45.965	59.667	32.479	36.816	66.224	56.693	77.195	88.642	57.487	91.406	92.887
1-13		0.005	-0.002	0.002	0.043	8.611	0.193	0.004	0.245	33.717	0.028	0.032	0	0.05	0.012	35.748	2.161	15.151	0.015

1-13	LLD (ppm)	19.427	34.945	9.902	11.054	19.505	20.027	46.102	23.61	32.205	16.258	18.401	33.588	27.319	36.973	44.628	25.728	43.242	44.077
1-13		0.007	-0.002	0.001	0.046	8.789	0.199	0.006	0.244	34.127	0.029	0.036	-0.001	0.056	0.013	35.983	2.177	15.243	0.013
1-13	LLD (ppm)	19.751	35.899	10.24	11.277	19.884	20.205	47.157	24.019	32.669	16.29	18.589	33.404	28.371	37.156	44.22	26.2	43.344	44.558
1-13		0.007	0.001	0.003	0.044	8.777	0.198	0.008	0.248	34.198	0.03	0.035	0	0.052	0.013	36.034	2.183	15.183	0.016
1-13	LLD (ppm)	19.897	35.774	10.173	11.091	19.836	20.101	46.807	23.983	32.505	16.158	18.552	33.275	28.182	38.081	44.435	26.843	43.274	44.334
1-13		0.006	0.002	0.002	0.044	8.773	0.197	0.004	0.249	34.068	0.028	0.035	-0.002	0.057	0.009	35.899	2.185	15.191	0.013
1-13	LLD (ppm)	19.783	35.652	10.032	11.002	19.966	20.263	47.145	24.089	32.766	16.394	18.652	32.83	27.625	38.007	44.429	25.975	43.55	44.535
1-14		0.003	0.001	0.001	0.053	10.444	0.25	-0.001	0.252	33.11	0.012	0.013	0	0.041	0.015	25.73	2.217	21.853	0.006
1-14	LLD (ppm)	19.588	35.053	9.994	11.134	19.534	19.508	46.046	23.212	31.607	16.136	17.881	32.824	26.334	33.128	40.645	25.605	45.99	48.22
1-14		0.006	0.001	0	0.057	10.772	0.252	0.004	0.259	33.65	0.012	0.013	0.001	0.046	0.014	26.083	2.244	22.063	0.005
1-14	LLD (ppm)	20.117	36.366	10.296	11.468	19.959	20.463	47.579	24.139	32.218	16.252	18.345	32.038	25.86	34.175	41.387	25.627	46.335	48.795
1-14		0.007	0.001	0.002	0.055	10.797	0.251	0.005	0.263	33.749	0.013	0.012	0	0.043	0.017	26.068	2.265	22.003	0.004
1-14	LLD (ppm)	20.191	36.244	10.317	11.796	20.081	20.275	46.819	24.116	32.184	16.113	18.457	33.008	27.438	33.385	41.165	25.884	46.386	48.81
1-14		0.008	0.001	0.001	0.056	10.77	0.249	0.007	0.263	33.648	0.013	0.013	-0.001	0.048	0.016	25.994	2.263	21.991	0.002
1-14	LLD (ppm)	20.116	36.444	10.385	11.55	20.084	20.303	46.849	23.779	32.083	16.075	18.374	33.232	27.205	33.854	41.171	26.046	46.463	49.037
1-15			0.001	0	0.057	12.312	0.237	0.006	0.217	28.305	0.005	0.023	-0.001	0.042	0.021	29.643	2.07	23.607	0.003
1-15	LLD (ppm)	19.59	35.468	10.179	11.169	19.541	19.532	45.573	22.992	30.792	15.963	18.271	32.414	28.841	34.996	41.975	25.776	47.503	49.99
1-15		0.006	-0.001	0.001	0.056	12.512	0.241	0.003	0.219	28.543	0.005	0.026	-0.002	0.048	0.017	29.884	2.078	23.692	0.006
1-15	LLD (ppm)	20.08	36.19	10.5	11.466	19.856	19.819	46.338	23.182	30.753	16.243	18.366	32.967	28.091	35.992	43.095	25.915	47.58	50.004
1-15		0.007	0.002	0.001	0.055	12.517	0.241	0.005	0.217	28.667	0.004	0.025	-0.003	0.043	0.019	29.886	2.088	23.735	0.007
1-15	LLD (ppm)	19.939	36.005	10.333	11.656	19.809	19.995	46.25	23.532	30.866	16.437	18.822	33.146	28.791	35.379	42.678	25.751	47.46	49.904
1-15		0.005	0.002	0	0.058	12.524	0.239	0.005	0.221	28.546	0.006	0.024	-0.001	0.046	0.013	29.856	2.091	23.749	0.013
1-15	LLD (ppm)	20.055	36.132	10.341	11.281	19.914	19.93	46.274	23.441	30.879	16.084	18.551	32.82	26.931	36.051	42.518	26.105	47.692	49.91
1-16		0.004	0.003	0.002	0.075	15.616	0.424	-0.001	0.299	24.561	0.008	0.02	-0.005	0.058	0.016	36.319	2.751	15.938	0.01
1-16	LLD (ppm)	31.42	56.526	15.61	16.746	31.032	31.119	72.451	37.401	45.838	26.982	33.204	59.576	47.47	54.07	70.354	42.908	66.693	68.891
1-17		0.007	-0.003	0.013	0.029	13.285	0.286	0.006	0.892	10.509	0.005	0.01	0.013	0.087	0	52.674	7.666	13.552	0.019
1-17	LLD (ppm)	18.595	33.702	9.593	10.423	18.51	18.247	41.743	21.189	25.07	15.428	18.836	34.986	29.115	44.625	50.716	35.625	45.98	43.299

		PbO	HfO2	CuO	NiO	Fe2O3	Cr2O3	BaO	TiO2	CaO	K2O	SO3	ZrO2	P2O5	SrO	SiO2	Al2O3	MgO	Na2O
Sample name	Result type	wt (%)	wt (%)	wt (%)	wt (%)	wt (%)	wt (%)	wt (%)	wt (%)	wt (%)	wt (%)	wt (%)	wt (%)	wt (%)	wt (%)	wt (%)	wt (%)	wt (%)	wt (%)
2-1		0.006	-0.001	0.018	0.293	11.722	0.523	0.022	0.394	24.703	0.512	0.02	0.003	0.032	0.009	40.77	4.493	14.711	0.012
2-1	LLD (ppm)	19.589	35.387	10.202	11.306	19.507	19.703	44.579	22.806	29.826	16.441	18.879	33.547	28.529	39.894	46.092	30.841	44.638	44.157
2-2		0.005	0.005	0.005	0.094	12.732	0.728	0.02	0.405	13.289	0.05	0.035	0.001	0.032	0.005	56.346	3.861	11.757	0.02
2-2	LLD (ppm)	18.755	33.906	9.643	10.653	18.61	18.784	42.614	21.493	26.211	15.715	19.04	35.222	30.658	45.619	50.995	31.41	43.499	41.918
2-3		-0.002	0.005	-0.003	0.001	0.284	0.008	-0.001	0.002	13.313	0.031	0.013	-0.018	0.004	0.001	82.259	0.173	0.092	0.02
2-3	LLD (ppm)	27.371	49.463	13.307	13.597	28.146	28.748	67.359	35.297	42.418	26.392	33.047	61.352	49.862	72.216	84.988	42.012	54.868	51.645
2-4		0.006	0.001	0.001	0.063	4.776	0.058	0.017	0.071	53.069	0.057	0.042	-0.002	0.032	0.003	24.2	1.521	11.564	0.004
2-4	LLD (ppm)	20.281	36.304	10.363	11.503	20.436	21.209	49.636	25.439	37.196	16.777	18.19	31.951	26.164	31.935	39.942	23.655	40.333	41.994
2-4		0.008	0	0	0.066	4.885	0.06	0.015	0.07	53.744	0.061	0.043	-0.002	0.031	0.002	24.437	1.527	11.66	0.007
2-4	LLD (ppm)	20.808	37.227	10.648	11.665	20.858	21.842	50.682	25.941	37.563	16.528	18.042	32.588	26.819	32.402	39.985	23.761	40.476	42.209
2-4		0.008	0.001	0.001	0.067	4.892	0.059	0.013	0.069	53.976	0.059	0.043	-0.004	0.032	0.002	24.492	1.546	11.636	0.004
2-4	LLD (ppm)	20.943	37.213	10.772	11.899	20.84	21.843	51.172	26.293	37.872	16.931	18.037	32.635	27.676	32.432	39.902	23.974	40.617	42.519
2-4		0.008	-0.001	0.001	0.067	4.897	0.059	0.019	0.071	53.733	0.059	0.044	0.001	0.032	0.001	24.363	1.54	11.629	0.005
2-4	LLD (ppm)	20.827	37.181	10.58	11.766	20.73	21.759	50.542	26.021	37.689	16.856	17.858	31.445	26.651	32.705	39.842	24.051	40.613	42.344
2-5		0.01	0	0.003	0.035	5.866	0.138	0.018	0.315	61.662	0.078	0.075	0.006	0.046	0.022	16.325	3.263	11.82	0.02
2-5	LLD (ppm)	21.392	38.01	10.883	12.221	21.29	22.237	52.066	26.725	39.673	17.209	17.843	31.748	27.091	28.066	36.944	25.95	41.573	42.914
2-6		0.001	-0.001	0.004	0.074	8.277	0.336	0.008	0.285	30.919	0.002	0.014	-0.003	0.029	0.028	29.374	2.904	23.775	0.006
2-6	LLD (ppm)	30.265	54.807	14.941	15.831	30.62	31.11	72.655	37.858	47.996	27.531	33.082	58.116	49.514	51.503	68.109	42.997	70.648	74.794
2-7		0.006	0.003	-0.001	0.053	14.439	0.25	0.002	0.795	9.485	0.01	0.086	0.009	0.072	0	50.819	7.803	15.622	0.011
2-7	LLD (ppm)	18.813	33.854	9.648	10.838	18.4	18.097	42.03	21.283	24.85	15.601	18.946	35.799	30.733	44.763	49.78	36.559	47.294	44.936
2-8c		0.003	0.001	0.001	0.036	4.555	0.132	-0.007	0.155	55.483	0.036	0.025	-0.005	0.018	0.026	13.305	1.925	17.663	0.012
2-8c	LLD (ppm)	31.397	56.627	15.645	16.675	32.113	32.91	77.708	40.175	54.977	27.695	32.358	57.003	47.587	40.217	60	37.453	65.116	70.333
2-8c		0.007	0.003	0.004	0.038	4.705	0.134	0.005	0.159	56.281	0.036	0.029	-0.003	0.021	0.03	13.471	1.946	17.818	0.011
2-8c	LLD (ppm)	32.163	58.311	16.065	17.076	32.838	33.709	79.117	40.944	55.804	28.066	32.398	57.025	47.262	41.962	60.491	39.076	66.236	71.064
2-8c		0.003	-0.002	0.002	0.038	4.718	0.138	-0.001	0.157	56.523	0.038	0.028	0.002	0.029	0.026	13.513	1.948	17.818	0.008

2-8c	LLD (ppm)	32.323	58.416	16.142	17.03	32.571	33.284	79.448	41.754	55.897	28.096	32.169	56.503	44.777	42.858	61.034	38.398	65.764	71.205
2-8c		0.004	0.003	0.004	0.039	4.71	0.136	0.012	0.161	56.294	0.034	0.031	-0.004	0.028	0.029	13.467	1.934	17.809	0.008
2-8c	LLD (ppm)	32.492	58.281	16.055	17.398	32.707	33.684	78.97	41.131	55.709	28.19	31.974	57.394	47.189	41.673	60.23	38.675	66.3	71.267
2-9		0.006	-0.001	0.02	0.151	16.721	0.651	0.001	0.388	24.071	0.004	0.044	-0.003	0.053	0.008	34.77	4.067	16.354	0.032
2-9	LLD (ppm)	31.597	57.62	15.754	16.933	31.19	31.086	72.633	37.191	45.683	27.131	32.618	58.878	49.382	55.074	70.071	45.316	67.954	69.665
2-11		0.005	0	0.002	0.039	6.868	0.085	0.01	0.425	38.022	0.007	0.012	-0.003	0.036	0.024	25.792	3.527	21.786	0.004
2-11	LLD (ppm)	19.551	35.037	9.949	11.048	19.61	20.249	47.065	23.901	33.388	16.263	18.458	31.982	26.362	33.496	40.861	28.312	46.82	48.748
2-11		0.006	0.002	0.004	0.039	6.985	0.089	0.008	0.434	38.324	0.007	0.013	-0.002	0.04	0.022	25.965	3.553	21.807	0.003
2-11	LLD (ppm)	19.886	35.629	10.097	11.179	19.962	20.231	47.765	24.391	33.824	16.314	18.137	32.947	27.38	33.25	40.811	28.13	47.073	48.9
2-11		0.007	0.002	0.002	0.042	7.001	0.085	0.008	0.429	38.575	0.007	0.011	-0.001	0.036	0.026	26.054	3.573	21.796	0.012
2-11	LLD (ppm)	19.766	35.515	10.168	11.183	19.926	20.537	47.618	24.573	33.581	16.652	18.267	32.638	28.198	33.181	41.225	27.857	46.793	48.626
2-11		0.008	0	0.001	0.041	6.989	0.086	0.003	0.431	38.346	0.009	0.012	-0.003	0.041	0.027	25.908	3.532	21.817	0.003
2-11	LLD (ppm)	19.833	35.714	10.194	11.1	19.815	20.512	48.209	24.534	33.472	16.197	18.418	32.317	27.336	33.265	41.444	28.174	46.956	48.778
2-15		0.005	0.002	0.012	0.014	13.985	0.016	0.008	0.985	8.467	0.018	0.059	0.005	0.08	0.014	53.636	9.802	10.061	1.779
2-15	LLD (ppm)	18.496	33.487	9.633	10.547	18.235	17.685	41.942	21.098	24.16	15.394	19.384	35.143	29.312	44.813	50.929	39.101	45.72	42.878
2-15		0.005	0	0.013	0.015	14.064	0.015	0.013	0.983	8.491	0.018	0.061	0.003	0.082	0.015	53.948	9.861	10.125	1.776
2-15	LLD (ppm)	18.51	33.837	9.684	10.587	18.47	17.837	41.931	21.079	24.271	15.501	19.319	35.609	29.292	44.871	50.884	38.89	45.718	43.295
2-15		0.006	0.003	0.013	0.015	14.081	0.015	0.009	0.988	8.53	0.017	0.061	0	0.083	0.016	53.999	9.849	10.107	1.776
2-15	LLD (ppm)	18.627	33.673	9.565	10.427	18.452	17.873	41.85	21.268	24.57	15.674	19.404	35.472	28.407	45.24	50.5	38.459	45.957	43.148
2-15		0.005	0.002	0.012	0.015	14.05	0.015	0.011	0.988	8.497	0.018	0.061	0	0.083	0.021	53.872	9.868	10.093	1.776
2-15	LLD (ppm)	18.579	33.753	9.602	10.518	18.472	17.938	42.009	21.493	24.344	15.476	19.403	35.209	29.249	44.934	50.59	38.563	45.75	43.268
2-23		0.005	-0.001	0.002	0.055	5.935	0.224	0.009	0.23	40.548	0.007	0.024	-0.001	0.036	0.025	23.873	2.465	20.069	0.008
2-23	LLD (ppm)	19.462	34.782	9.979	11.035	19.784	20.132	46.735	23.931	33.732	16.112	17.98	32.347	26.386	32.561	39.555	25.496	45.093	47.127
2-23		0.008	0.005	0.002	0.057	6.141	0.234	0.003	0.24	41.278	0.008	0.026	-0.003	0.039	0.03	24.137	2.48	20.251	0.005
2-23	LLD (ppm)	20.023	36.013	10.3	11.352	20.124	20.796	48.665	25.017	34.341	16.22	18.567	33.209	26.081	32.354	40.262	25.95	45.335	47.486
2-23		0.007	0.002	0.003	0.058	6.17	0.23	0.008	0.241	41.512	0.008	0.024	-0.003	0.041	0.027	24.181	2.496	20.228	0.002
2-23	LLD (ppm)	20.214	36.18	10.228	11.299	20.338	20.862	48.552	24.353	34.704	16.26	18.562	32.245	26.791	32.482	40.367	25.414	45.518	47.547
2-23		0.007	-0.001	0.002	0.058	6.158	0.233	0.008	0.239	41.348	0.006	0.025	-0.002	0.04	0.022	24.129	2.492	20.243	0.002
2-23	LLD (ppm)	20.139	36.097	10.261	11.287	20.195	20.772	48.009	24.664	34.411	16.537	18.365	32.349	27.011	33.352	39.896	25.812	45.453	47.646

Monitor standards																	
	PbO	HfO2	CuO	NiO	Fe2O3	Cr2O3	BaO	TiO2	CaO	K2O	SO3	ZrO2	P2O5	SrO	SiO2	Al2O3	MgO	Na2O
SARM 6 certified					17	0.42	0.00	0.02	0.28	0.010			0.01	0.0004	38.96	0.3	43.51	0.04
SARM6 measured	0.005	0.002	-0.001	0.258	17.541	0.434	0.001	0.013	0.245	0.005	0.023	-0.006	0.004	-0.004	39.089	0.252	44.483	0.013
SARM6 measured	0.006	-0.001	-0.002	0.26	17.45	0.432	0.003	0.011	0.243	0.004	0.021	-0.005	0.003	0	38.957	0.25	44.334	0.011
Average	0.0055	0.0005	-0.002	0.259	17.496	0.433	0.002	0.012	0.244	0.0045	0.022	-0.006	0.0035	-0.002	39.023	0.251	44.409	0.012
Delta					-0.496	-0.013	-9E-04	0.008	0.036	0.0055			0.0065	0.0024	-0.063	0.049	-0.899	0.028
StDev	0.0005	0.0015	0.0005	0.001	0.0455	0.001	0.001	0.001	0.001	0.0005	0.001	0.0005	0.0005	0.002	0.066	0.001	0.0745	0.001
StDev/average (%)	9.1%	300.0%	-33.3%	0.4%	0.3%	0.2%	50.0%	8.3%	0.4%	11.1%	4.5%	-9.1%	14.3%	######	0.2%	0.4%	0.2%	8.3%
SARM 2 certified					1.4	0.0018	0.27	0.04	0.68	15.35			0.12	0.007	63.63	17.34	0.46	0.43
SARM2 measured	0.003	-0.002	-0.001	0.001	1.392	0.004	0.282	0.035	0.644	15.405	0.015	-0.002	0.109	0	62.634	16.698	0.445	0.403
SARM2 measured	0.004	0.001	0.001	0	1.395	0.002	0.283	0.037	0.647	15.447	0.016	-0.003	0.108	0.007	62.705	16.703	0.446	0.4
Average	0.0035	-5E-04	0	0.0005	1.3935	0.003	0.2825	0.036	0.6455	15.426	0.0155	-0.003	0.1085	0.0035	62.67	16.701	0.4455	0.4015
Delta					0.0065	-0.001	-0.013	0.004	0.0345	-0.076			0.0115	0.0038	0.9605	0.6395	0.0145	0.0285
StDev	0.0005	0.0015	0.001	0.0005	0.0015	0.001	0.0005	0.001	0.0015	0.021	0.0005	0.0005	0.0005	0.0035	0.0355	0.0025	0.0005	0.0015
StDev/average (%)	14.3%	######	######	100.0%	0.1%	33.3%	0.2%	2.8%	0.2%	0.1%	3.2%	-20.0%	0.5%	100.0%	0.1%	0.0%	0.1%	0.4%
BCR 2 certified					13.8	0.0026	0.08	2.26	7.12	1.79			0.35	0.05	54.1	13.5	3.59	3.16
BCR2 measured	0.008	0.003	0	0.002	14.122	0.003	0.078	2.23	7.046	1.818	0.096	0.02	0.36	0.04	54.439	13.376	3.597	3.18
BCR2 measured	0.004	0	0.002	0.003	14.089	0.004	0.082	2.227	7.033	1.798	0.097	0.022	0.35	0.035	54.41	13.352	3.616	3.183
Average	0.006	0.0015	0.001	0.0025	14.106	0.0035	0.08	2.2285	7.0395	1.808	0.0965	0.021	0.355	0.0375	54.425	13.364	3.6065	3.1815
Delta					-0.305	-9E-04	-0.004	0.0315	0.0805	-0.018			-0.005	0.0115	-0.324	0.136	-0.017	-0.021
StDev	0.002	0.0015	0.001	0.0005	0.0165	0.0005	0.002	0.0015	0.0065	0.01	0.0005	0.001	0.005	0.0025	0.0145	0.012	0.0095	0.0015
StDev/average (%)	33.3%	100.0%	100.0%	20.0%	0.1%	14.3%	2.5%	0.1%	0.1%	0.6%	0.5%	4.8%	1.4%	6.7%	0.0%	0.1%	0.3%	0.0%
AGV 2 certified					6.69	0.0025	0.13	1.05	5.2	2.88			0.48	0.078	59.3	16.91	1.79	4.19
AGV2b measured	0.007	-0.001	0.004	0.003	6.853	0.003	0.133	1.017	5.158	2.927	0.01	0.026	0.476	0.078	59.573	16.696	1.805	4.217
AGV2b measured	0.004	0.003	0.004	0.003	6.838	0.002	0.132	1.02	5.156	2.931	0.01	0.024	0.473	0.07	59.617	16.671	1.793	4.213
Average	0.0055	0.001	0.004	0.003	6.8455	0.0025	0.1325	1.0185	5.157	2.929	0.01	0.025	0.4745	0.074	59.595	16.684	1.799	4.215
Delta					-0.155	0	-0.005	0.0315	0.043	-0.049			0.0055	0.0038	-0.295	0.2265	-0.009	-0.025

StDev	0.0015	0.002	0	0	0.0075	0.0005	0.0005	0.0015	0.001	0.002	0	0.001	0.0015	0.004	0.022	0.0125	0.006	0.002
StDev/average (%)	27.3%	200.0%	0.0%	0.0%	0.1%	20.0%	0.4%	0.1%	0.0%	0.1%	0.0%	4.0%	0.3%	5.4%	0.0%	0.1%	0.3%	0.0%
SARM1 certfied					2	0.0018	0.01	0.09	0.78	4.99			0.02	0.001	75.7	12.08	0.06	3.36
SARM1 measured	0.007	0.001	-0.002	0	1.984	0.002	0.033	0.083	0.739	5.036	0.031	0.035	0.007	-0.006	75.548	11.82	0.05	3.313
SARM1 measured	0.004	0	-0.001	0	1.974	0.003	0.029	0.084	0.734	5.015	0.036	0.034	0.006	-0.009	75.455	11.823	0.049	3.305
Average	0.0055	0.0005	-0.002	0	1.979	0.0025	0.031	0.0835	0.7365	5.0255	0.0335	0.0345	0.0065	-0.008	75.502	11.822	0.0495	3.309
Delta					0.021	-7E-04	-0.018	0.0065	0.0435	-0.035			0.0135	0.0087	0.1985	0.2585	0.0105	0.051
StDev	0.0015	0.0005	0.0005	0	0.005	0.0005	0.002	0.0005	0.0025	0.0105	0.0025	0.0005	0.0005	0.0015	0.0465	0.0015	0.0005	0.004
StDev/average (%)	27.3%	100.0%	-33.3%	######	0.3%	20.0%	6.5%	0.6%	0.3%	0.2%	7.5%	1.4%	7.7%	-20.0%	0.1%	0.0%	1.0%	0.1%

Appendix C: LA-ICP-MS data

	COMMENT CELL	Ca ppm	Sc ppm	Ti ppm	Sr ppm	Y ppm	La ppm	Ce ppm	Pr ppm	Nd ppm	Sm ppm	Eu ppm	Gd ppm	Tb ppm	Dy ppm	Ho ppm	Er ppm	Tm ppm	Yb ppm	Lu ppm	Pb ppm	Th ppm	U ppm
1-1	Average	52898.40	19.90	2279.88	32.09	9.98	3.47	7.26	0.82	3.72	1.03	0.46	1.22	0.20	1.39	0.28	0.86	0.11	0.81	0.12	3.64	0.40	0.13
	Standard deviation	540.81	0.47	23.97	0.47	0.11	0.07	0.17	0.01	0.12	0.05	0.03	0.08	0.00	0.07	0.02	0.03	0.01	0.04	0.02	0.18	0.02	0.00
1-3	Average	88767.68	13.51	1205.93	63.85	6.23	1.86	4.13	0.53	2.65	0.78	0.19	0.84	0.14	0.94	0.18	0.51	0.08	0.51	0.07	0.93	0.21	0.23
	Standard deviation	526.64	0.21	34.65	1.22	0.13	0.05	0.07	0.01	0.14	0.07	0.03	0.07	0.01	0.02	0.01	0.04	0.01	0.05	0.00	0.04	0.02	0.03
1-6	Average	168232.00	13.24	1398.76	60.52	10.94	1.54	3.31	0.43	2.13	0.58	0.20	0.80	0.11	0.87	0.18	0.47	0.07	0.44	0.07	3.00	0.22	0.28
	Standard deviation	1821.46	0.26	27.00	1.25	0.07	0.04	0.07	0.03	0.01	0.06	0.03	0.10	0.01	0.03	0.02	0.03	0.01	0.05	0.01	0.12	0.02	0.02
1-7	Average	143357.29	16.63	2920.03	57.43	8.00	2.92	6.78	0.98	4.87	1.32	0.35	1.52	0.23	1.53	0.33	0.81	0.10	0.78	0.11	2.23	0.43	0.17
	Standard deviation	1557.53	0.22	29.53	0.79	0.16	0.05	0.08	0.01	0.03	0.16	0.04	0.23	0.01	0.15	0.03	0.02	0.01	0.04	0.01	0.08	0.01	0.00
1-8	Average	104426.69	16.92	2514.89	27.96	11.16	3.06	6.21	0.85	4.25	1.34	0.42	1.57	0.28	1.68	0.35	0.89	0.13	0.83	0.12	1.94	0.38	0.22
	Standard deviation	2423.07	0.62	54.97	0.42	0.20	0.07	0.14	0.03	0.08	0.09	0.04	0.09	0.02	0.10	0.04	0.11	0.02	0.07	0.01	0.07	0.02	0.02
1-10	Average	196688.78	10.55	936.38	114.42	3.18	1.20	2.60	0.34	1.60	0.45	0.14	0.48	0.09	0.57	0.12	0.31	0.04	0.31	0.05	1.29	0.20	0.35
	Standard deviation	1649.00	0.24	14.95	1.68	0.08	0.04	0.05	0.01	0.15	0.04	0.03	0.04	0.01	0.05	0.01	0.01	0.01	0.01	0.00	0.03	0.02	0.01
1-11	Average	77809.35	45.49	2784.04	68.87	10.54	2.17	5.47	0.77	3.76	1.33	0.40	1.52	0.31	2.10	0.41	1.03	0.14	0.91	0.13	3.11	0.45	0.11
	Standard deviation	1131.21	0.73	42.03	1.18	0.20	0.09	0.22	0.02	0.19	0.10	0.02	0.21	0.02	0.15	0.02	0.07	0.01	0.08	0.02	0.18	0.03	0.02
1-12	Average	132951.41	44.21	3318.12	54.24	10.00	2.79	6.43	0.89	4.45	1.38	0.42	1.52	0.27	2.01	0.39	1.06	0.17	1.10	0.15	1.47	0.42	0.29
	Standard deviation	3688.89	1.36	64.64	0.98	0.28	0.13	0.10	0.05	0.36	0.22	0.03	0.13	0.02	0.07	0.04	0.08	0.02	0.08	0.01	0.10	0.04	0.02
1-13	Average	169560.82	11.61	1045.07	85.40	3.90	1.45	3.16	0.40	1.99	0.57	0.14	0.57	0.10	0.67	0.16	0.40	0.06	0.37	0.05	1.55	0.27	0.32
	Standard deviation	2488.68	0.49	32.23	2.20	0.11	0.09	0.08	0.01	0.09	0.09	0.02	0.11	0.00	0.04	0.01	0.02	0.01	0.03	0.00	0.11	0.02	0.01
1-14	Average	165996.99	13.98	1153.19	104.53	3.26	0.97	2.18	0.30	1.46	0.47	0.13	0.55	0.09	0.62	0.13	0.34	0.05	0.34	0.05	0.77	0.16	0.24
	Standard deviation	1591.90	0.33	32.17	0.95	0.12	0.02	0.03	0.02	0.09	0.03	0.02	0.11	0.01	0.02	0.02	0.04	0.01	0.03	0.00	0.05	0.02	0.01
1-15	Average	136801.94	11.61	958.61	114.59	2.89	0.90	1.90	0.27	1.26	0.43	0.17	0.43	0.08	0.57	0.11	0.29	0.04	0.31	0.04	1.04	0.13	0.43
	Standard deviation	2449.44	0.38	24.72	2.06	0.08	0.06	0.03	0.02	0.09	0.04	0.01	0.07	0.01	0.04	0.01	0.05	0.01	0.04	0.01	0.03	0.01	0.02
1-16	Average	121766.39	16.56	1366.27	59.68	4.70	2.11	4.16	0.53	2.76	0.76	0.21	0.86	0.13	0.86	0.16	0.46	0.06	0.48	0.07	2.03	0.19	0.19
	Standard deviation	1232.31	0.48	30.81	0.65	0.12	0.08	0.05	0.03	0.09	0.12	0.03	0.10	0.01	0.05	0.02	0.06	0.01	0.03	0.01	0.10	0.02	0.02
1-17	Average	57525.60	34.39	4012.57	44.94	11.09	3.89	8.65	1.14	5.76	1.61	0.60	2.06	0.33	2.22	0.45	1.22	0.18	1.20	0.17	3.22	0.57	0.14
	Standard deviation	769.20	0.61	120.06	1.33	0.21	0.09	0.21	0.07	0.16	0.10	0.02	0.03	0.02	0.10	0.04	0.04	0.02	0.07	0.02	0.10	0.04	0.01

2-1	Average	119654.64	9.40	1702.38	66.07	5.17	2.60	4.99	0.66	3.05	0.77	0.15	0.90	0.14	0.94	0.18	0.48	0.06	0.47	0.06	2.49	0.23	0.21
	Standard deviation	4159.30	0.54	27.60	1.53	0.12	0.11	0.13	0.04	0.18	0.13	0.01	0.13	0.02	0.06	0.03	0.05	0.01	0.08	0.01	0.08	0.02	0.01
2-2	Average	67940.42	12.64	2079.38	55.89	4.21	1.33	3.40	0.49	2.37	0.64	0.11	0.64	0.12	0.88	0.17	0.46	0.07	0.45	0.06	1.85	0.19	0.07
	Standard deviation	1649.09	1.06	48.06	1.51	0.17	0.07	0.12	0.03	0.12	0.08	0.02	0.08	0.01	0.03	0.01	0.03	0.01	0.03	0.01	0.05	0.01	0.01
2-3	Average	61856.60	2.39	308.67	4.57	0.66	0.21	0.46	0.07	0.32	0.08	0.03	0.10	0.02	0.12	0.03	0.08	0.01	0.07	0.01	0.29	0.04	0.04
	Standard deviation	927.20	0.10	7.71	0.13	0.04	0.01	0.02	0.01	0.04	0.02	0.00	0.01	0.00	0.02	0.00	0.02	0.00	0.00	0.00	0.04	0.01	0.00
2-4	Average	264685.56	4.20	352.57	25.71	6.44	2.64	4.39	0.76	3.50	1.04	0.34	1.27	0.18	1.17	0.26	0.63	0.09	0.57	0.07	1.77	0.40	0.24
	Standard deviation	4297.66	0.57	7.26	0.57	0.20	0.09	0.09	0.04	0.26	0.07	0.02	0.17	0.01	0.13	0.05	0.07	0.01	0.11	0.02	0.09	0.03	0.01
2-5	Average	272428.94	8.46	1334.81	112.71	5.95	3.24	5.53	0.79	3.44	0.87	0.14	0.88	0.14	1.00	0.20	0.65	0.09	0.58	0.08	1.72	0.87	0.54
	Standard deviation	13298.03	0.58	38.13	4.04	0.29	0.14	0.25	0.04	0.23	0.10	0.03	0.14	0.01	0.08	0.02	0.08	0.01	0.05	0.01	0.12	0.06	0.03
2-6	Average	146917.81	9.51	1188.98	146.83	4.25	0.46	1.33	0.22	1.08	0.43	0.06	0.66	0.12	0.83	0.17	0.46	0.07	0.46	0.05	0.44	0.08	0.38
	Standard deviation	4931.66	0.55	25.16	7.01	0.18	0.02	0.07	0.02	0.09	0.04	0.03	0.08	0.02	0.05	0.03	0.10	0.01	0.07	0.01	0.06	0.01	0.01
2-7	Average	51835.03	26.72	4051.06	64.96	10.75	3.11	7.88	1.10	5.65	1.76	0.82	1.88	0.30	2.08	0.43	1.33	0.19	1.15	0.17	8.41	0.44	0.11
	Standard deviation	1723.53	1.02	104.20	1.70	0.37	0.10	0.18	0.05	0.29	0.09	0.06	0.20	0.02	0.15	0.03	0.09	0.01	0.06	0.01	0.18	0.02	0.01
2-8c	Average	258254.88	5.06	707.14	140.86	2.56	1.77	2.55	0.43	1.94	0.39	0.11	0.52	0.07	0.45	0.08	0.25	0.04	0.22	0.03	1.84	0.33	0.73
	Standard deviation	10412.43	0.86	14.23	4.81	0.11	0.09	0.14	0.03	0.33	0.09	0.01	0.11	0.01	0.10	0.03	0.07	0.01	0.14	0.01	0.20	0.04	0.03
2-9	Average	116811.41	10.22	1623.42	52.47	5.12	2.25	4.99	0.65	3.13	0.92	0.35	0.98	0.15	0.99	0.18	0.52	0.07	0.47	0.07	2.70	0.31	0.40
	Standard deviation	1946.71	0.45	24.69	1.34	0.07	0.04	0.22	0.03	0.13	0.07	0.03	0.08	0.01	0.07	0.02	0.02	0.01	0.09	0.01	0.09	0.02	0.02
2-11	Average	183454.91	11.56	1701.12	143.91	3.99	0.71	1.81	0.30	1.43	0.47	0.04	0.69	0.11	0.74	0.16	0.44	0.05	0.40	0.06	0.92	0.10	0.32
	Standard deviation	2858.56	1.16	44.33	4.26	0.16	0.05	0.08	0.04	0.10	0.08	0.02	0.13	0.01	0.08	0.02	0.09	0.01	0.07	0.01	0.05	0.02	0.01
2-15	Average	47967.02	32.49	4594.81	148.07	10.74	2.71	6.99	1.06	4.99	1.53	0.59	1.90	0.34	2.21	0.43	1.25	0.19	1.21	0.19	3.34	0.53	0.11
	Standard deviation	580.21	1.53	175.55	7.30	0.48	0.21	0.37	0.05	0.28	0.24	0.03	0.17	0.02	0.08	0.05	0.12	0.03	0.11	0.03	0.12	0.04	0.01
2-23	Average	193967.13	7.41	1016.32	152.98	3.34	1.00	2.47	0.31	1.63	0.37	0.06	0.43	0.08	0.62	0.13	0.36	0.04	0.29	0.04	3.29	0.21	0.40
	Standard deviation	7887.77	1.05	38.80	6.83	0.18	0.09	0.18	0.04	0.16	0.08	0.01	0.14	0.01	0.18	0.02	0.14	0.01	0.09	0.03	0.29	0.04	0.07
	Monitor standards																						
AGV 2	Average	39088.08	13.49	7106.78	671.93	17.43	37.03	69.82	7.87	30.33	5.39	1.45	4.23	0.57	3.30	0.65	1.73	0.23	1.64	0.23	12.22	6.06	1.86
	Standard deviation	1856.99	0.93	325.35	34.49	1.11	2.60	4.29	0.61	2.07	0.42	0.16	0.57	0.07	0.34	0.07	0.30	0.04	0.21	0.04	0.86	0.33	0.08
NIST 612	Average	85125.00	41.07	43.86	78.18	37.78	35.22	38.23	36.68	35.41	37.80	34.36	36.10	35.97	35.84	37.75	37.50	37.60	38.90	36.25	38.80	37.66	37.40
	Standard deviation	1257.79	0.72	1.82	1.55	0.82	1.23	1.37	1.34	1.16	1.16	1.25	1.46	0.70	0.80	0.98	1.12	1.23	1.18	1.48	0.75	0.76	0.51
NIST 610	Average	83258.33	488.47	499.43	516.75	457.06	431.08	454.59	440.93	431.24	455.77	432.94	430.09	431.28	443.40	451.68	448.26	447.44	461.12	437.67	431.26	461.90	469.81
	Standard deviation	857.54	8.86	6.69	13.97	12.71	17.18	16.95	16.31	17.03	15.84	17.90	20.70	7.85	11.67	12.53	16.64	16.86	16.25	21.57	12.99	8.18	4.95

		Li ppm	B ppm	P ppm	K ppm	Ca ppm	Ti ppm	Ti ppm	V ppm	Cr ppm	Co ppm	Ni ppm	Cu ppm	Cu ppm	Zn ppm	Zn ppm	Ge ppm	Rb ppm	Zr ppm	Nb ppm	Cs ppm	Ba ppm	Nd ppm	Hf ppm	Ta ppm	W ppm	U ppm
1-1	Average	183000.68	166320.08	3.67	-234.28	25654.64	1173.04	1158.46	47.96	435.26	19.05	80.27	16.31	17.25	29.46	28.83	0.55	0.18	67.15	0.64	0.02	2.60	1.96	1.65	0.03	0.10	0.05
	Standard d	6618.09	4101.96	13.45	204.20	724.03	39.95	30.60	1.67	12.23	1.04	2.86	0.66	0.78	2.21	3.29	0.14	0.01	3.42	0.04	0.00	0.23	0.09	0.06	0.01	0.03	0.01
1-3	Average	182714.10	169179.73	43.35	64.93	45331.02	636.21	617.09	36.81	456.15	28.76	127.42	9.06	9.97	22.95	22.63	0.75	0.09	17.61	0.37	0.01	7.99	1.33	0.39	0.02	0.07	0.12
	Standard d	2464.02	5277.14	18.93	184.11	1145.34	2.41	19.39	1.08	6.22	0.43	2.68	0.30	0.48	0.98	1.86	0.23	0.02	0.64	0.01	0.01	0.33	0.05	0.02	0.01	0.03	0.01
1-6	Average	265640.45	238107.66	34.67	-2940.23	80915.81	716.87	689.51	41.28	864.73	62.92	278.56	29.67	30.97	43.66	44.99	0.58	2.12	56.00	0.46	0.03	19.04	1.04	1.15	0.02	0.33	0.11
	Standard d	8970.69	6345.51	26.15	288.67	1830.00	12.75	29.42	1.38	25.45	2.16	9.17	0.87	1.36	2.02	4.79	0.13	0.13	1.74	0.04	0.01	0.62	0.11	0.07	0.01	0.08	0.02
1-7	Average	222396.75	205959.97	59.89	-11292.78	71930.20	1425.00	1447.29	52.25	556.56	20.31	194.81	18.70	19.95	19.95	19.82	0.77	6.45	14.14	0.74	0.04	19.67	2.58	0.34	0.05	0.09	0.07
	Standard d	5278.69	5900.02	27.05	564.91	878.40	47.75	39.67	1.18	10.70	0.53	6.95	0.97	1.13	0.69	2.95	0.24	0.23	0.55	0.03	0.01	0.70	0.21	0.04	0.00	0.03	0.02
1-8	Average	224513.72	210658.73	74.00	-7470.15	51420.88	1252.09	1245.90	50.57	463.09	47.21	184.10	22.58	23.51	21.53	23.98	0.55	4.87	14.88	0.74	0.03	19.64	2.36	0.33	0.04	0.88	0.10
	Standard d	7829.35	8601.76	30.78	616.44	1124.32	29.16	41.67	0.61	6.26	1.08	4.87	0.80	0.36	1.35	1.97	0.23	0.09	0.66	0.06	0.01	0.65	0.19	0.02	0.01	0.15	0.01
1-10	Average	223980.90	218258.04	72.03	116.43	97426.76	479.73	464.34	36.90	580.38	32.62	164.56	22.97	23.42	44.91	42.61	0.80	0.09	6.16	0.26	0.00	12.45	0.84	0.15	0.01	0.10	0.18
	Standard d	7250.73	7261.47	24.97	379.92	2965.75	6.93	15.79	0.60	27.41	0.96	7.37	0.36	1.07	1.12	1.76	0.25	0.04	0.17	0.02	0.01	0.62	0.06	0.02	0.00	0.02	0.02
1-11	Average	228164.51	226618.68	40.96	285.98	37007.17	1338.69	1398.98	83.47	117.33	19.25	60.53	11.39	11.77	37.15	38.41	0.98	0.12	15.81	0.86	0.01	3.00	2.09	0.41	0.04	0.22	0.05
	Standard d	5347.10	6885.45	43.35	393.81	940.16	19.03	46.70	3.05	2.75	0.35	1.36	0.97	1.39	1.83	5.58	0.32	0.02	0.34	0.04	0.00	0.29	0.20	0.02	0.01	0.04	0.01
1-12	Average	311432.12	299710.13	37.56	679.34	64018.08	1661.06	1653.07	90.07	1072.83	41.25	179.56	11.99	12.41	61.91	60.34	0.67	0.10	16.45	0.79	0.00	17.62	2.33	0.44	0.04	0.21	0.13
	Standard d	12925.64	7709.77	48.76	189.41	2105.47	62.71	51.14	4.47	44.43	1.75	5.10	0.71	0.42	6.14	4.74	0.20	0.03	0.50	0.07	0.01	0.42	0.20	0.04	0.01	0.04	0.01
1-13	Average	222779.41	215728.37	95.36	142.70	83823.48	549.98	510.03	31.66	445.73	23.89	116.28	26.96	28.07	36.70	39.07	0.83	0.19	8.56	0.32	0.01	11.43	1.09	0.18	0.02	0.06	0.14
	Standard d	11143.62	6099.46	17.77	399.09	2481.36	27.86	14.46	1.23	7.10	0.70	5.53	1.08	0.55	2.08	2.39	0.37	0.02	0.40	0.03	0.01	0.70	0.04	0.04	0.01	0.02	0.02
1-14	Average	222035.24	218560.77	35.57	137.32	82708.95	622.43	585.70	40.27	560.88	28.04	147.58	5.72	5.94	24.07	23.26	0.80	0.10	5.57	0.30	0.01	11.74	0.83	0.15	0.01	0.16	0.11
	Standard d	6247.83	6395.06	23.15	534.04	1617.19	10.27	14.33	0.51	11.47	0.38	3.12	0.36	0.41	1.35	2.63	0.15	0.03	0.19	0.03	0.00	0.47	0.06	0.02	0.00	0.08	0.01
1-15	Average	220116.18	211327.76	74.36	-324.50	67130.03	506.21	484.99	35.19	508.65	27.16	144.73	7.01	7.42	27.89	28.19	0.74	0.03	4.46	0.24	-0.01	10.83	0.75	0.10	0.01	0.07	0.21
	Standard d	4267.05	3436.48	30.83	764.13	593.99	10.81	6.48	0.78	6.58	0.24	2.86	0.37	0.29	1.55	2.79	0.20	0.02	0.07	0.03	0.01	0.46	0.04	0.04	0.01	0.02	0.01
1-16	Average	245945.20	231953.22	83.83	1157.96	60310.25	710.21	703.10	38.18	986.56	47.36	221.46	17.56	18.20	36.42	33.87	0.75	0.08	6.46	0.35	0.01	8.96	1.31	0.19	0.02	0.14	0.09
	Standard d	5987.44	7441.41	34.67	1923.28	1517.61	17.85	21.92	0.71	16.41	1.03	7.89	0.68	0.40	2.34	3.44	0.42	0.02	0.19	0.02	0.00	0.16	0.11	0.03	0.01	0.03	0.01
1-17	Average	233630.17	232093.88	97.87	2486.52	28284.84	1985.80	1980.11	83.07	667.26	22.85	82.16	33.30	35.15	37.91	36.70	0.86	0.09	20.68	1.11	0.02	5.39	3.16	0.56	0.06	0.21	0.07
	Standard d	7482.69	5357.04	90.53	3534.73	714.86	43.26	62.20	2.20	12.93	0.68	1.50	0.78	0.94	2.27	1.53	0.33	0.03	0.34	0.06	0.01	0.16	0.12	0.06	0.01	0.05	0.01

2-1	Average	221428.35	220595.02	53.57	-57607.09	57738.04	883.81	862.26	27.94	1137.62	64.96	798.57	45.30	46.23	39.27	47.38	0.56	3.27	9.66	0.42	0.03	61.32	1.66	0.24	0.03	0.15	0.09
	Standard d	8144.10	5002.83	24.69	19978.30	2015.74	30.29	14.28	0.77	37.50	1.84	25.41	1.90	1.33	2.80	8.31	0.28	0.12	0.37	0.04	0.01	2.28	0.17	0.03	0.01	0.01	0.01
2-2	Average	258697.30	261007.72	127.42	-77364.14	34383.29	1043.19	1051.59	43.62	1846.24	31.20	289.01	17.51	17.54	33.68	33.68	0.64	0.60	11.94	0.51	0.02	65.12	1.24	0.32	0.03	0.35	0.02
	Standard d	7973.47	7649.04	50.81	131874.83	745.37	29.70	21.53	1.01	49.04	0.77	5.59	0.45	0.52	1.48	6.64	0.18	0.06	0.33	0.03	0.01	2.68	0.12	0.07	0.01	0.06	0.00
2-3	Average	57688.83	57138.83	14.85	-250.56	31875.52	161.09	155.89	8.77	314.60	7.47	75.35	1.75	1.80	6.43	7.53	0.21	0.02	1.87	0.08	0.00	23.69	0.15	0.03	0.00	0.04	0.02
	Standard d	2181.25	1406.88	6.56	373.93	406.47	4.40	3.86	0.15	10.21	0.10	1.37	0.04	0.08	0.24	0.78	0.11	0.01	0.06	0.01	0.00	0.53	0.01	0.01	0.00	0.00	0.00
2-4	Average	215776.28	217345.56	83.70	3007.79	130198.10	202.70	173.67	15.35	133.02	19.97	180.78	14.64	15.12	14.52	18.31	0.53	0.43	6.51	0.18	0.02	52.75	1.67	0.12	0.01	0.04	0.10
	Standard d	7489.57	8768.65	75.62	4410.77	3652.87	8.35	9.87	1.03	5.21	1.01	8.64	0.41	0.89	1.12	3.67	0.82	0.07	0.37	0.05	0.02	3.07	0.19	0.04	0.00	0.02	0.02
2-5	Average	209355.58	204208.36	152.02	1776.19	135854.43	676.07	662.47	28.27	306.97	12.10	93.05	12.51	12.42	17.90	16.70	0.48	0.35	21.17	0.57	0.01	32.64	1.77	0.55	0.03	0.09	0.25
	Standard d	6367.26	5101.90	115.82	1793.04	4400.39	33.70	21.79	1.47	13.16	0.41	4.19	0.25	0.72	1.58	2.80	0.34	0.07	0.54	0.07	0.01	1.14	0.21	0.03	0.01	0.01	0.04
2-6	Average	210260.41	215256.11	126.36	-630.34	71673.67	582.59	568.04	38.32	694.99	18.07	192.92	6.02	5.99	25.58	25.86	0.58	0.04	6.22	0.29	0.00	25.46	0.49	0.13	0.01	0.05	0.18
	Standard d	3786.19	5318.06	87.35	1519.05	1205.92	11.62	10.97	0.51	11.31	0.26	3.50	0.33	0.31	1.32	3.20	0.36	0.02	0.24	0.05	0.00	1.00	0.04	0.03	0.01	0.03	0.01
2-7	Average	243156.81	247829.91	276.23	57.12	25400.88	1919.60	1899.35	78.72	600.23	27.49	160.81	7.16	7.35	52.70	53.84	0.95	0.19	20.70	0.99	0.03	12.08	2.76	0.55	0.04	0.12	0.05
	Standard d	7038.62	6305.21	87.39	701.52	888.87	33.15	60.79	1.68	15.89	1.00	3.29	0.22	0.06	2.66	2.04	0.33	0.06	0.97	0.06	0.01	0.29	0.12	0.03	0.01	0.01	0.01
2-8c	Average	206634.79	214611.97	288.21	419.45	126821.78	367.21	356.66	26.63	296.44	11.51	96.83	17.58	18.32	19.20	19.38	0.29	0.17	8.22	0.23	0.00	21.72	0.89	0.13	0.01	0.03	0.34
	Standard d	4922.98	2494.89	526.52	639.33	2477.35	7.91	6.78	1.54	5.06	0.54	2.83	0.63	1.23	1.84	2.89	0.46	0.04	0.32	0.04	0.02	0.52	0.07	0.09	0.00	0.02	0.02
2-9	Average	238304.64	240645.55	364.01	-249.31	57949.23	822.13	812.76	40.38	1391.20	37.84	414.69	44.23	45.40	93.06	94.81	0.82	0.07	8.91	0.47	0.00	3.37	1.56	0.24	0.03	0.07	0.20
	Standard d	3213.96	10969.85	441.33	317.81	2061.93	10.15	12.23	1.10	20.80	1.09	2.88	1.45	0.77	1.00	5.07	0.21	0.01	0.13	0.03	0.01	0.29	0.10	0.04	0.01	0.03	0.02
2-11	Average	208234.46	221361.50	935.08	111.49	88436.71	865.49	832.76	34.29	189.82	15.74	107.34	8.75	9.38	14.76	16.60	0.53	0.04	9.84	0.37	0.01	27.44	0.58	0.22	0.02	0.05	0.14
	Standard d	6694.62	8365.13	457.05	427.15	3327.25	20.25	20.26	2.22	6.82	0.54	3.67	0.46	0.92	1.11	2.68	0.17	0.03	0.40	0.04	0.01	1.22	0.08	0.03	0.01	0.02	0.03
2-15	Average	240485.60	254121.62	-3502.97	43.37	23870.28	2149.48	2139.36	100.46	52.66	21.49	47.65	44.62	44.62	36.52	38.35	1.13	0.21	25.38	1.21	0.03	28.68	2.52	0.68	0.07	0.12	0.05
	Standard d	14257.37	6993.14	1565.98	425.11	893.08	73.29	75.40	4.13	1.67	0.51	2.36	2.40	1.09	1.12	4.29	0.31	0.04	0.80	0.05	0.01	0.73	0.03	0.05	0.01	0.02	0.01
2-23	Average	264179.70	261826.21	-1019.85	-186.32	97260.10	537.58	499.73	25.32	521.10	14.61	150.21	52.11	54.50	37.01	43.62	0.19	0.04	6.60	0.26	-0.01	22.75	0.72	0.14	0.01	0.06	0.18
	Standard d	13296.03	13141.81	658.11	653.27	2864.91	10.86	21.84	1.05	15.65	0.65	4.88	2.35	3.18	2.89	6.27	0.33	0.03	0.36	0.03	0.01	0.50	0.06	0.03	0.01	0.03	0.03
														Monitor standards													
AVG 2	Average	127246.85	128762.23	1203.37	20880.48	7151.10	1204.73	1200.18	22.50	3.33	2.82	3.88	10.73	10.96	14.38	23.50	0.36	9.81	38.61	2.55	0.14	203.18	5.60	0.82	0.14	0.10	0.31
	Standard d	6833.66	9714.05	4397.35	76032.69	478.95	62.46	52.17	1.45	0.57	0.14	0.68	1.47	1.78	1.47	3.36	0.43	0.58	1.24	0.23	0.02	8.37	0.28	0.09	0.02	0.04	0.03
NIST 612	Average	43.24	35.78	-971.62	-64.62	85192.31	43.98	44.19	39.15	35.98	34.98	38.83	37.09	37.10	37.98	38.58	35.10	31.45	38.08	40.12	42.11	39.75	35.91	35.05	40.17	40.16	37.37
	Standard d	6.14	5.69	3474.63	939.54	2048.06	1.76	1.37	1.30	1.28	1.16	0.65	0.80	0.93	1.53	3.74	1.33	0.77	0.60	0.79	0.94	1.12	0.49	0.51	0.86	1.14	0.64
NIST 610	Average	435.54	252.92	3365.38	2004.62	83676.92	497.77	506.85	457.54	418.17	416.48	464.35	420.92	430.38	446.69	451.08	395.63	425.35	450.62	489.54	371.46	455.97	441.05	420.31	486.85	472.38	464.88
	Standard d	12.19	11.96	11589.27	6741.64	917.48	8.47	13.78	8.50	8.97	9.95	5.41	5.43	9.72	14.63	17.70	6.74	7.96	6.49	11.24	6.74	5.83	8.01	6.59	8.46	11.23	5.98

Appendix D: LOI data

Sample	Crucible mass	Sample + crucible	sample mass	Post moisture loss (sample+ crucible)	Moisture loss	Sample after moisture loss	OM (sample+ crucible) (550°C)	Carbonate (sample+cr ucible) (950°C)	Mass of lost sample after 950°	Sample mass in disc	Flux mass in disc	LOI
	grams	grams	grams	grams	grams	grams	grams	grams	grams	grams	grams	%
1-1	17.2303	22.7617	5.5314	22.7407	0.0210	5.5104	22.6656	21.8864	0.8543	0.8706	6.6712	15.50
1-3	15.5581	21.3460	5.7879	21.3270	0.0190	5.7689	21.2539	19.8695	1.4575	0.4370	6.6707	25.26
1-6	15.4840	21.8642	6.3802	21.8470	0.0172	6.3630	21.7488	20.1109	1.7361	0.4366	6.6701	27.28
1-7	18.6575	24.2415	5.5840	24.2260	0.0155	5.5685	24.1508	22.6352	1.5908	0.8696	6.6699	28.57
1-8	15.0488	20.9859	5.9371	20.9727	0.0132	5.9239	20.8937	19.6545	1.3182	0.8700	6.6708	22.25
1-10	12.2596	15.2659	3.0063	15.2597	0.0062	3.0001	15.2171	14.3902	0.8695	0.8697	6.6754	28.98
1-11	13.9576	20.1491	6.1915	20.1439	0.0052	6.1863	20.1098	18.8954	1.2485	0.8697	6.6697	20.18
1-12	14.4543	20.5037	6.0494	20.4892	0.0145	6.0349	20.4058	19.2835	1.2057	0.4351	6.6700	19.98
1-13	11.9921	14.9988	3.0067	14.9906	0.0082	2.9985	14.9477	14.1934	0.7972	0.8693	6.6709	26.59
1-14	16.8492	19.8520	3.0028	19.8477	0.0043	2.9985	19.8074	18.9898	0.8579	0.8725	6.6715	28.61
1-15	15.3074	18.3102	3.0028	18.3048	0.0054	2.9974	18.2474	17.4487	0.8561	0.8688	6.6705	28.56
1-16	16.1139	22.1812	6.0673	22.1701	0.0111	6.0562	22.1154	20.5143	1.6558	0.4352	6.6694	27.34
1-17	13.4378	19.5733	6.1355	19.5685	0.0048	6.1307	19.5434	18.5646	1.0039	0.8701	6.6711	16.37
2-1	14.0847	20.1438	6.0591	20.1378	0.0060	6.0531	20.0995	18.5205	1.6173	0.8702	6.6707	26.72
2-2	14.6715	20.7712	6.0997	20.7672	0.0040	6.0957	20.7506	19.6640	1.1032	0.8695	6.6717	18.10
2-3	16.6691	22.7214	6.0523	22.7038	0.0176	6.0347	22.6643	20.8545	1.8493	0.4350	6.6698	30.64
2-4	15.0423	18.0448	3.0025	18.0369	0.0079	2.9946	18.0071	17.1501	0.8868	0.8701	6.6715	29.61
2-5	15.8167	21.9815	6.1648	21.9651	0.0164	6.1484	21.8694	19.7579	2.2072	0.8695	6.6710	35.90
2-6	14.5511	20.4900	5.9389	20.4830	0.0070	5.9319	20.4349	18.7051	1.7779	0.4343	6.6702	29.97
2-7	14.9280	21.0982	6.1702	21.0898	0.0084	6.1618	21.0140	20.1526	0.9372	0.8694	6.6719	15.21
2-8 c	18.8043	21.8066	3.0023	21.7973	0.0093	2.9930	21.7631	20.7178	1.0795	0.4347	6.6730	36.07
2-9	15.8406	21.8022	5.9616	21.7869	0.0153	5.9463	21.6228	20.1534	1.6335	0.4350	6.6708	27.47
2-11	16.4326	19.4390	3.0064	19.4333	0.0057	3.0007	19.3858	18.5223	0.9110	0.8703	6.6724	30.36
2-15	16.8538	19.8573	3.0035	19.8545	0.0028	3.0007	19.8060	19.4893	0.3652	0.8701	6.6686	12.17
2-23	10.8243	13.8258	3.0015	13.8195	0.0063	2.9952	13.7829	12.8908	0.9287	0.8690	6.6690	31.01